



**This electronic thesis or dissertation has been  
downloaded from Explore Bristol Research,  
<http://research-information.bristol.ac.uk>**

*Author:*

**Szeremeta, Witek K**

*Title:*

**On the use of evanescent fields to investigate nanoscale phenomena - from optical  
forces to cellular processes.**

**General rights**

Access to the thesis is subject to the Creative Commons Attribution - NonCommercial-No Derivatives 4.0 International Public License. A copy of this may be found at <https://creativecommons.org/licenses/by-nc-nd/4.0/legalcode>. This license sets out your rights and the restrictions that apply to your access to the thesis so it is important you read this before proceeding.

**Take down policy**

Some pages of this thesis may have been removed for copyright restrictions prior to having it been deposited in Explore Bristol Research. However, if you have discovered material within the thesis that you consider to be unlawful e.g. breaches of copyright (either yours or that of a third party) or any other law, including but not limited to those relating to patent, trademark, confidentiality, data protection, obscenity, defamation, libel, then please contact [collections-metadata@bristol.ac.uk](mailto:collections-metadata@bristol.ac.uk) and include the following information in your message:

- Your contact details
- Bibliographic details for the item, including a URL
- An outline nature of the complaint

Your claim will be investigated and, where appropriate, the item in question will be removed from public view as soon as possible.

---

---

# On the use of evanescent fields to investigate nanoscale phenomena - from optical forces to cellular processes.

---

---

By

WITOLD KRZYSZTOF SZEREMETA



School of Physics  
UNIVERSITY OF BRISTOL

A dissertation submitted to the University of Bristol in accordance with the requirements for award of the degree of DOCTOR OF PHILOSOPHY in the Faculty of Science.

25 NOVEMBER 2020

Word count: 41518



## ABSTRACT

Nanoscale is a special regime where the convergence of natural sciences occurs. Developing versatile tools to investigate phenomena on that scale is crucial for understanding intricate mechanisms which have consequences on macroscale.

This work shows the development of the new generation of Lateral Molecular Force Microscope (LMFM) and in particular the design of a new Vertical Positioning System for vertically oriented micro-cantilevers as well as a method for adjusting their tilt angle. The vertical orientation of the mechanical sensor allows it to have much lower stiffness (compared to that of a conventional Atomic Force Microscope), giving access to femtonewton and sub-femtonewton force resolution.

The unidirectional bending of the silicon nitride cantilevers entering the evanescent field is investigated and identified as an effect triggered by light coupling inside the cantilever. In relation to this bias bending, photostriction effect has been identified as the most likely mechanism behind it.

This work presents a range of optical forces measured in an evanescent field. In particular, a new experimental procedure is implemented to directly measure the transverse Belinfante spin momentum. The new experimental results give an additional insight into the fact, that the transfer of the helicity-dependent momentum to the micro-cantilever is a surface effect.

Finally, the LMFM setup is used to develop and establish the Sub-Cellular Fluctuation Imaging method. Scattering from the sub-cellular components of a bacterium under evanescent field illumination is utilised to assess its metabolic state, opening up the possibility of a label-free rapid Antimicrobial Susceptibility Tests.



## DEDICATION AND ACKNOWLEDGEMENTS

### TO MY PARENTS

#### Acknowledgements

I am extremely grateful to my supervisor, Dr. Massimo Antognozzi for his continual enthusiasm for research, his support, encouragement and the ever insightful conversations and advice throughout the duration of this project. It has been a pleasure to learn from and to do research with someone so knowledgeable and creative.

Thank you also to Kanasanun Phonrat, Jake Sheridan and Sophia Wisniewska for all the joint work we did. Working together was always both productive and very enjoyable.

For the many helpful discussions and advice over the last four years, I would like to thank my second supervisor Prof. Mervyn Miles as well as Prof. Ruth Oulton, Prof. John Hannay, Dr. Henkjan Gersen, Dr. Simon Hanna, Dr. Tomas Martin, Dr. Christopher Jones, Dr. Germinal Margo, Dr. Caroline Jarrett and Dr. Andrew Murray. I would also like to thank Tom Kennedy, John Rowden, Adrian Crimp and the Mechanical Workshop for their technical support.

Last but not least, thank you to my closest family and friends for supporting me throughout my PhD journey and for making it a very enjoyable four years in Bristol. I would also like to thank my granddad Dr. n. med Sławomir Jastrzębski and Dr. Iwona Paleska for inspiring me to pursue research from a young age.



## **AUTHOR'S DECLARATION**

I declare that the work in this dissertation was carried out in accordance with the requirements of the University's Regulations and Code of Practice for Research Degree Programmes and that it has not been submitted for any other academic award. Except where indicated by specific reference in the text, the work is the candidate's own work. Work done in collaboration with, or with the assistance of, others, is indicated as such. Any views expressed in the dissertation are those of the author.

SIGNED: ..... DATE: .....





## TABLE OF CONTENTS

<b>Abstract</b>	<b>i</b>
<b>Dedication and Acknowledgements</b>	<b>iii</b>
<b>Author's declaration</b>	<b>v</b>
<b>List of Figures</b>	<b>xi</b>
<b>List of Abbreviations</b>	<b>xv</b>
<b>1 Introduction</b>	<b>1</b>
1.1 Nanoscale System . . . . .	1
1.2 Optical Forces . . . . .	3
1.3 Optical Tweezers . . . . .	4
1.4 Scanning Probe Microscopes . . . . .	6
1.5 Vertically Oriented Probes . . . . .	7
1.6 Bibliography . . . . .	10
<b>2 Optical Forces in the Evanescent Field</b>	<b>17</b>
2.1 Optical Forces . . . . .	17
2.1.1 Electromagnetic stress–energy tensor . . . . .	17
2.1.2 Dipole approximation for small small particles . . . . .	19
2.1.3 Analytical model for optical forces acting on small particles . . . . .	20
2.2 Evanescent Field . . . . .	22

## TABLE OF CONTENTS

---

2.2.1	Theoretical description . . . . .	22
2.2.2	Polarisation . . . . .	25
2.2.3	Characteristics of the evanescent field . . . . .	30
2.3	Optical Forces in the Evanescent Field . . . . .	31
2.4	Bibliography . . . . .	33
<b>3</b>	<b>Lateral Molecular Force Microscope</b>	<b>37</b>
3.1	Near-field Scanning Optical Microscopy . . . . .	37
3.2	Overview of the Lateral Molecular Force Microscope . . . . .	38
3.2.1	Microscope environment overview . . . . .	39
3.2.2	Modes of operation . . . . .	40
3.3	Microfabricated Probes . . . . .	42
3.4	Scattered Evanescent Wave detection setup . . . . .	43
3.4.1	Measuring the depth of the evanescent wave . . . . .	45
3.4.2	Detection of Scattered Evanescent Wave . . . . .	47
3.5	Microscope Electronics and Software . . . . .	51
3.6	Sample and Probe Positioning . . . . .	52
3.6.1	Horizontal Translation Stages . . . . .	53
3.6.2	Vertical positioning of the sample stage . . . . .	56
3.6.3	Vertical Positioning System for the probe . . . . .	56
3.6.4	Tilt Adjustment . . . . .	59
3.6.5	Performance and Stability of Sample and Probe Positioning Systems . . . . .	62
3.6.6	Measuring Rotation Around X-axis . . . . .	63
3.7	Bibliography . . . . .	65
<b>4</b>	<b>Achieving sub-fN precision measurements using LMFM</b>	<b>71</b>
4.1	Experimental Procedure . . . . .	72
4.1.1	Displacement Measurements . . . . .	72
4.1.2	Auto-correlation study of data acquisition rate . . . . .	74
4.1.3	Calibration methods of the cantilevers' spring constant . . . . .	74

4.2	sub-fN resolution . . . . .	77
4.3	Bibliography . . . . .	80
<b>5</b>	<b>Optically induced unidirectional bending in Si<sub>3</sub>N<sub>4</sub> cantilevers</b>	<b>83</b>
5.1	Initial Observations . . . . .	84
5.1.1	Evanescent wave dependence (2-prism setup) . . . . .	87
5.2	Light coupling within the cantilever and its polarisation dependence . . . . .	90
5.2.1	Simulation methods, FDTD and DGTD . . . . .	90
5.2.2	Finding refractive index of cantilevers using ellipsometry . . . . .	92
5.2.3	Effect of the polarisation on bias bending . . . . .	92
5.2.4	3D simulations of cantilevers under s-polarised and p-polarised illumination . . . . .	94
5.3	Removing Bias Bending . . . . .	96
5.3.1	Triangular Cutout Scheme . . . . .	96
5.3.2	2 Holes scheme . . . . .	98
5.3.3	Manufacturing cantilever with modified end using focused ion beam . . . . .	101
5.3.4	Bias bending on cantilevers with circular and triangular cut-outs . . . . .	102
5.4	Locating the bias bending along the probe . . . . .	105
5.5	Discussion of the results . . . . .	107
5.5.1	Transfer of momentum - surface roughness or curvature of cantilever leading to recoil force . . . . .	107
5.5.2	Thermal gradient . . . . .	110
5.5.3	photostriction and thermal expansion - volumetric change effect . . . . .	110
5.6	Bibliography . . . . .	112
<b>6</b>	<b>Direct measurements of optical forces in the evanescent fields</b>	<b>117</b>
6.1	Measuring longitudinal force associated with orbital momentum of the evanescent field	118
6.1.1	Optically driven Mie particles in an evanescent field . . . . .	118
6.1.2	Attaching spheres to the SPM probes . . . . .	120
6.1.3	Measuring the orbital momentum on a Mie-sized sphere using LMFM with silicon nitride probes . . . . .	122

## TABLE OF CONTENTS

---

6.1.4	Measuring the orbital momentum on the Mie-sized sphere using LMFM with custom made glass probes . . . . .	125
6.2	Belinfante spin momentum . . . . .	128
6.2.1	Belinfante spin momentum - overview . . . . .	128
6.2.2	Direct measurement of the Belinfante's spin momentum by removing the bias bending . . . . .	130
6.3	Conclusions . . . . .	135
6.4	Bibliography . . . . .	136
<b>7</b>	<b>Use of evanescent field scattering to investigate sub-cellular activity in bacteria</b>	<b>139</b>
7.1	Sub-cellular Fluctuation Imaging (SCFI) - overview . . . . .	139
7.1.1	Fluctuation description . . . . .	141
7.2	Explaining the scattering pattern of a bacterium in an evanescent field . . . . .	144
7.3	Manipulating bacteria with LMFM probe to study the origin of the SCFI signal . . . .	147
7.4	Conclusions . . . . .	148
7.5	Bibliography . . . . .	149
<b>8</b>	<b>Final Conclusions</b>	<b>151</b>

## LIST OF FIGURES

FIGURE	Page
1.1 Diagram illustrating the gradient forces experienced by a sphere in a Gaussian beam . .	5
1.2 Tilt effect on the cantilever effective stiffness . . . . .	9
2.1 k-vectors of the incident beam and the resultant evanescent field . . . . .	24
2.2 LCVR calibration . . . . .	30
2.3 Evanescent field properties . . . . .	31
3.1 The Lateral Molecular Force Microscope . . . . .	39
3.2 Cantilever array diagram . . . . .	43
3.3 Diagram of the SEW detection system for the LMFM with a closeup illustration of the scattering cantilever tip in the evanescent field and an incidence bean coming at an angle ( $\alpha$ ) adapted from [2] . . . . .	44
3.4 Adjusting angle of incidence using adjustable mirrors . . . . .	45
3.5 Incidence angle evaluation through the use of prism method . . . . .	46
3.6 Incidence angle evaluation through the use probe approach method . . . . .	47
3.7 Pixel size calibration . . . . .	48
3.8 Principles of operations of a QPD . . . . .	48
3.9 Calibration of the QPD signal for displacement measurements . . . . .	50
3.10 Residual analysis of the fitting function in figure 3.9 . . . . .	51
3.11 Schematic diagram of the electronics in LMFM . . . . .	52
3.12 Horizontal Translation Stages . . . . .	54
3.13 Horizontal Translation Stages - piezo motor calibration . . . . .	55

## LIST OF FIGURES

---

3.14	Vertical Positioning Systems . . . . .	57
3.15	Vertical Positioning System - test in high vacuum . . . . .	60
3.16	Tilt Adjustment Scheme . . . . .	61
3.17	Performance and Stability of the Sample and Probe Positioning Systems . . . . .	63
3.18	Schematic of evaluating the rotation of the probe around x-axis . . . . .	64
4.1	Visualisation of the principles behind displacement measurements . . . . .	72
4.2	2 $\mu$ m silica spheres displacement measurement . . . . .	73
4.3	Autocorrelation of the data . . . . .	75
4.4	Power Spectrum Density . . . . .	77
4.5	Force measurement with sub-fN precision . . . . .	79
4.6	Probe stiffness histogram . . . . .	80
5.1	Cantilever orientation convention . . . . .	84
5.2	Summary of the Initial Bias Bending Observations . . . . .	85
5.3	Bias Bending Observations on Cantilever with a Sphere Attached . . . . .	86
5.4	2-prism setup . . . . .	87
5.5	Diagram illustrating the generation of the cantilever image for the CMOS camera . . . . .	88
5.6	Cantilever motion recorded for a 2-prism setup . . . . .	89
5.7	Diagram illustrating the difference between rectangular grid used in FDTD and an adaptive mesh used for DGTD . . . . .	90
5.8	Refractive index of silicon nitride cantilevers measured via ellipsometry . . . . .	93
5.9	Force experienced by the probe, due to the s-polarised and p-polarised light . . . . .	94
5.10	Simulations of light coupling inside the probes for p-polarised and s-polarised light . . . . .	95
5.11	Diagram of the triangular cutout scheme . . . . .	97
5.12	Simulations of the Triangular Cutout Scheme . . . . .	98
5.13	2 holes scheme optimisation . . . . .	99
5.14	Simulations of the 2-Holes Scheme . . . . .	100
5.15	Mounting cantilevers for FIB . . . . .	101
5.16	Reduction of bias bending using 2 holes design . . . . .	103

5.17	Reduction of bias bending using triangular cutout design . . . . .	104
5.18	Simulation of light propagating through the length of the cantilever . . . . .	105
5.19	Entire cantilever movement observations using CMOS camera . . . . .	106
5.20	EDX of silicon nitride cantilevers . . . . .	108
5.21	Diagram illustrating a method for estimating curvature of cantilevers . . . . .	109
5.22	Comparison of surface roughness of 2 sides of the cantilever . . . . .	109
6.1	Cantilever orientation convention (focus on chapter 6) . . . . .	118
6.2	Measuring the force on Mie-sized spheres in an evanescent field. . . . .	119
6.3	Attaching Spheres . . . . .	121
6.4	Simulations of the 3 different configurations of the sphere attached to the probe . . . . .	123
6.5	Longitudinal momentum measurement using spheres attached to silicon nitride cantilevers	124
6.6	Glass micro-needle results . . . . .	126
6.7	Spin-hall effect as an analogy with spin flow loops . . . . .	128
6.8	Previous Belinfante measurements . . . . .	129
6.9	The optical setup for the Belinfante spin momentum measurements . . . . .	130
6.10	Experimental results for Belinfante spin momentum measurement . . . . .	134
7.1	Comparison of images of a single <i>E.coli</i> bacterium between standard optical microscopy and SCFI . . . . .	141
7.2	Visualisation of the SCFI data analysis . . . . .	142
7.3	Log-normal distribution of SCFI data . . . . .	143
7.4	Fluctuation measurements for 3 different bacteria states . . . . .	144
7.5	FDTD simulation of a bacterium in evanescent field . . . . .	145
7.6	Reduction of 2 spots visible in SCFI . . . . .	146
7.7	Effect of mechanical binding of bacteria on the SCFI measurement . . . . .	148





## LIST OF ABBREVIATIONS

AFM	Atomic Force Microscope
DLS	Dynamic Light Scattering
DoF	Degrees of Freedom
FIB	Focused Ion Beam
HTS	Horizontal Translation Stages
LMFM	Lateral Molecular Force Microscope
NMR	Nuclear Magnetic Resonance
NSOM	Near-field Scanning Optical Microscope
PAINT	Points Accumulation for Imaging in Nanoscale Topography
PSD	Power Spectrum Density
SEM	Scanning Electron Microscope
SEW	Scattered Evanescent Wave
SPM	Scanning Probe Microscope
STM	Scanning Tunneling Microscope
TEM	Transmission Electron Microscope
TIR	Total Internal Reflection
TIRF	Total Internal Reflection Fluorescence
VOP	Vertically Oriented Probe
VPS	Vertical Positioning System



## INTRODUCTION

## 1.1 Nanoscale System

From the very beginning, humanity has been fascinated by the world surrounding us. From the large celestial objects, through tangible macroscale phenomena, all the way to wondering what are we and what is everything else made out of on the most fundamental level. Great philosophers of the ancient Greece made amazing intellectual efforts to try and find answers; most notably Democritus who is credited with the first formulation of the atomic theory of the Universe. However not until the 20<sup>th</sup> century science had an effective way of exploring nanoscale systems. In 1959, partially inspired by the earlier inventions of the Transmission Electron Microscope (TEM) and Scanning Electron Microscopy (SEM) [1], Richard Feynman gave his famous talk "There's Plenty of Room at the Bottom" which discussed the possibility of manipulating matter on nanoscale [2]. By many, this talk is considered to mark the beginning of nanotechnology as a field [3] and thanks to Feynmans undisputed talent as a science populariser, he managed to grab his listeners attention and inspire following generations of scientists to investigate countless nanoscale systems.

These systems are not easy to observe, starting from the most fundamental barrier which is the diffraction limit [4]. The nanoscale regime ranges from  $10^{-9}\text{m}$  to  $10^{-6}\text{m}$  whilst the visible light wavelength  $\lambda$  ranges from 380nm to 700nm; the diffraction limit when using a lens with numerical

aperture  $NA$  is given by  $\lambda/2NA$  and imposes a limit on the size of the structures that we can observe using classical optical methods. For the shortest wavelength  $\lambda \sim 380\text{nm}$  in the visible spectrum and the largest numerical aperture  $NA \sim 1.5$  we get a limit, on the size of a feature that can be resolved, of  $\sim 130\text{nm}$  which is 3 orders of magnitude larger than atoms and molecules.

One of the unique aspect of nanoscale regime, is that it is where the convergence of natural sciences occurs. At this level, physics, chemistry, biology, engineering, material science, medicine and other disciplines intertwine with each other, share common features, techniques and more fundamental questions [5]. Investigations on this scale allowed us to understand previously unexplained, macroscopically observed phenomena as in the case of the catalytic activity of Pt(110) during CO oxidization [6] or the discovery of the DNA molecule using x-ray diffraction images [7]. With evergrowing evidence of the possibility of quicker and more reliable medical diagnosis performed using nanoscale observations [8–10], it is clear that investigations on this level are crucial to the development of our technology and improvement to our daily lives.

Moreover, nanoscale itself is a fascinating regime for fundamental physics and material sciences, as it is effectively a mesoscale between the quantum mechanical or single molecular realm and the classical or bulk realm of large ensembles of matter. Objects on this scale may require quantum mechanical consideration, like the quantised conductance in carbon nanotubes [11]. Furthermore, the dynamic behaviour of these structures is no longer completely controlled by gravity, as is the case for their macroscale counterparts. At the nanoscale, interactions such as the Van der Waals forces [12] or thermal Brownian motion [13] play a much more relevant role.

As mentioned above, one of the first tools created for nanoscale discovery was the electron microscope, which gave us the ability to 'see' with high resolution by using high energy electrons instead of photons. However not only is this technique mainly confined to non-living samples, but it also mainly focuses on one aspect of discovery: the 'sight'. With all the amazing phenomena happening on the nanoscale, there is a need to expand our 'sensory' capabilities beyond 'vision'. Only by including mechanical forces ('touch'), chemical reactions ('smell'/'taste') and many others, will it be possible to aquire a full understanding of nanoscale processes. A clear example of this necessity is the study of bio-molecular machines [14].

## 1.2 Optical Forces

Even before Kepler's observation of a comet's tail and crediting the pressure of solar radiation for the orientation of the comet's tail away from the sun, scientists have been fascinated by the possibility of light exchanging momentum with matter [15]. Kepler's discovery is arguably the first clear example that established the idea of light being able to exert mechanical force. The biggest breakthrough in the understanding of what light was, was achieved by James Clerk Maxwell in the second half of the 19<sup>th</sup> century when he condensed all the experimental evidence on electromagnetism in the famous set of four equations. The same equations allowed him to hypothesise that light is in fact an electromagnetic wave [16]. First successful experiments on light pressure were carried out by Nichols together with Hull [17] and Lebedev [18] at the beginning of the 20<sup>th</sup> century. Unfortunately, due to extremely small momentum carried by light, experimental work in this field was deemed impractical and was put on hold by the wider scientific community.

For the next 50 years most advancements (though not exclusively) were made on the theoretical side of things. Most influential work, performed on the topic of momentum of light, was done by John Henry Poynting (including his earlier introduction of the energy flow vector better known nowadays as the Poynting vector [19]) and Guy Barlow [20–23] as well as the independent research by M. Abraham [24, 25] and H. Minkowski [26] whose derivations on momentum of light in a dielectric would start a century-long debate in the scientific community known as the 'Abraham-Minkowski controversy' [27, 28]. More information about Poynting's work can be found in a comprehensive review of his work on radiation pressure written by Loudon and Baxter [29].

Simultaneously, Albert Einstein published his renowned paper on Special Theory of Relativity [30], which aimed to address the need for the Maxwell's equations to be transformed covariantly. This paper initiated the emergence of Relativistic Field Theory and the Quantum Electrodynamics. Initially most of the work in this field was focused on explaining phenomena related to electrons [31–34]. Nevertheless, work on Relativistic Field Theory had almost immediate impact on the description of the massless photons and the momentum associated with these electromagnetic waves. In fact in 1940 F.J. Belinfante introduced an additional term to the stress-energy tensor in order to resolve the issue of its gauge-dependence [35] and by doing so introduced a new term describing the spin

momentum of photons.

For almost a century Belinfante's spin momentum was thought to be an unobservable quantity, even though effects originating from it were in fact observed like the transverse shift due to Belinfante's component of the stress-energy vector [36–38] known as Fedorov-Imbert effect. This effect was suggested in 1955 by Fedorov [39] and measured by Imbert in 1972 [40]. It took 75 years before Bliokh et al. suggested that the Belinfante's spin momentum could actually be observed in a circularly polarised evanescent field [41] and a few years later Antognozzi's group experimentally verified this prediction, using a development scanning probe microscope [42].

With most of the work on radiation pressure, in the first half of the 20<sup>th</sup> century, focusing on theory, a massive breakthrough came in 1960 with the invention of the laser [43], allowing scientists to access monochromatic light sources with significantly higher intensity density than what was available before. This led to A. Ashkin demonstrating the acceleration and trapping of particles using radiation pressure in 1970 [44] and the creation of the first optical tweezers instrument [45]. This technique will be described in more details in the following section (see section 1.3). The invention of the laser [43] opened up a completely new area of research making it possible to investigate the dependency of transfer of light momentum depending on the size of particles as well as their refractive index. As often happens in science, an enabling technology, can have disruptive effects in the way new fundamental phenomena are studied.

### 1.3 Optical Tweezers

When in 1969 Ashkin began his work on measuring radiation pressure from a focused laser beam, he could not have anticipated to come across an effect which would lay foundations to the modern day optical tweezers technique (otherwise known as optical trapping). The aim of his 1970 experiment [44] was to observe the effect of radiation pressure on a latex micro-sphere which he predicted to be along the direction of the laser beam. To his surprise as well as the initially expected forward movement, he observed the tendency of the latex spheres to move towards the centre axis of the beam. This effect can be explained intuitively by the combination of reflection and refraction from and in the sphere. Using a simple ray diagram (see figure 1.1) one can see how the move towards

the centre of the beam is a manifestation of the electromagnetic gradient force [46]. From these observations, Ashkin realised that, while a latex sphere would converge towards the center of the beam, objects of lower refractive index than the medium would be repelled away from the centre axis of the beam. This behaviour was particularly clear when using air bubbles in liquid. In a different experiment, Ashkin found that by arranging two lasers, so that their beams were counterpropagating and the forward radiation pressure would cancel out, he created the first ever optical trap [44]. The forward force generated by a single laser, acting on the micro-sphere, was comparable in magnitude to the gravity acting on the micro-sphere, which led Ashkin and Dziedzic to create the first stable optical levitation trap [47]. By illuminating the sphere from beneath it, they were able to balance the forward momentum of light with the gravitational pull downwards, enabling them to control the micro-sphere both in air and in vacuum. In the final embodiment Ashkin and coworkers, used a tightly focused beam from an objective with higher numerical aperture and they demonstrated that, by using this arrangement, it was possible to trap a micro-sphere without the use of the counteracting force due to gravity [45].

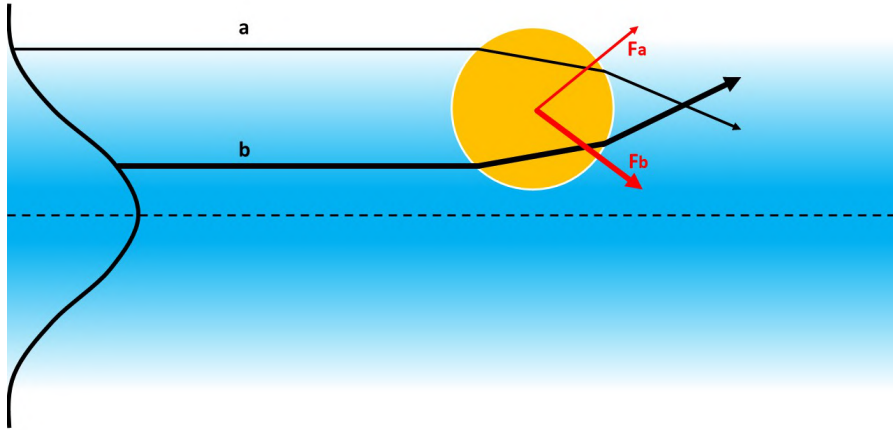


FIGURE 1.1. Ray diagram illustrating the gradient force experienced by a Mie-sized particles in a Gaussian beam

Optical tweezers have quickly become an extremely versatile and widely used technology. Experiments ranging from detecting forces on a sphere charged by a single electron charge [48, 49] to manipulation of viruses, bacteria and other biological samples [50]. However, care needs to be taken when working with biological samples in an optical trap, as the biological systems can be irreversibly



damaged by the high intensity of the focused laser beam. It has been shown that working in infrared regime can be a potential solution to this issue.

Following the development of these highly innovative tools to study and simultaneously utilising the radiation pressure from a laser beam, the next step in the context of investigating and understanding optical forces is to look at structured light. Several recent experiments were performed to detect the angular momentum of light [51] as well as its spin momentum [52], though these experiments were mainly performed on Gaussian and Laguerre-Gaussian beams [53]. The more subtle optical effects in evanescent fields have proven to be much more challenging when using optical tweezers setups due to the size of the region of interest as well as the optical tweezer's limited tip-sample separation control [54].

## 1.4 Scanning Probe Microscopes

Scanning Probe Microscopy is a family of techniques which originated in the IBM Zurich Research Laboratory in 1981. In that year G. Binnig, H. Rohrer, Ch. Gerber and E. Welbel reported on their successful experiment in which they observed vacuum tunneling through a controllable vacuum gap [55]. One year later, utilising a metal probe and combining it with a feedback mechanism and piezo drives they created the first ever Scanning Tunneling Microscope (STM) and presented topographical pictures of (110) surface reconstructions of  $CaIrSn_4$  and gold [56]. Shortly after, the group published the famous paper on  $7 \times 7$  reconstruction of Si(111) [57]. With such richness of results obtained by STM observation of conductive samples, it became clear that creating a method of performing similar experiments on the surfaces of insulators would be of great value to the academic community. Following their early success with STM, in 1986, G. Binnig, C.F. Quate and Ch. Gerber created the first ever Atomic Force Microscope (AFM) [58]. AFM contrary to STM measures force between a sharp tip and a sample surface and are not limited to conductive surfaces, so it can be used to investigate surfaces of insulators. Furthermore, AFM utilise 3 different modes of operation: contact, tapping and the most relevant in the context of measuring optical forces the non-contact mode. The non-contact mode is based on the interaction between a mechanical simple harmonic oscillator (SHO) and a force field gradient. The effect of the force gradient on a SHO is to shift the resonant frequency and

can be detected using simple demodulation techniques [59].

In short, the now greatly diverse family of SPMs can be described as a group of techniques utilising micro or nano-sized probes which can map the sample surface, measuring desired physical properties. The SPM family also includes Nearfield Scanning Optical Microscopes (NSOM) which will be further described in detail in section 3.1.

In the context of investigating fundamental optical forces, we will focus our attention on any SPM technique which detects extremely small forces through a shift in the cantilever's resonant frequency. One such example, is the measurement of the gradient force of an evanescent field [60]. By measuring the shift in resonant frequency of a modulated AFM cantilever above an evanescent field, researchers were able to create a 'topography of light' of a totally internally reflected beam. This map measured the attractive vertical gradient force of the evanescent field present above the substrate [60–62].

## 1.5 Vertically Oriented Probes

Over the past 30 years the SPM family has grown and diversified. One can divide the SPM family and differentiate many groups within it, depending on their mode of operation or quantities they measure. One such group, that can be identified, is a group of SPMs which uses Vertically Oriented Probe (VOP). Such geometry is characteristic of previously mentioned STMs, Near-field Scanning Optical Microscopy (NSOM) [63–65] and other techniques like the Lateral Molecular Force Microscopy (LMFM) [66] or the Transverse Dynamic Force Microscopy (TDFM) [67]. Common for all of these techniques is the vertical orientation of the probe which is perpendicular to the sample.

Positioning probes vertically carries numerous advantages for force sensing in the plane of the sample. Especially the possibility of using much softer cantilevers than conventional AFM. The stiffness of a probe  $k$  ultimately determines the force resolution of a probe microscope as the force  $F$  is calculated using Hooke's Law

$$F(d) = -kd \tag{1.1}$$

where  $d$  is the observed displacement of the cantilever tip. The minimum stiffness  $k_{min}$  of the probe is limited by the presence of the field gradient (i.e. electrostatic field or Van der Waals interactions) [12]. In the case of conventional AFM, as the probe approaches the region of interest, it needs to be

sufficiently stiff to withstand the attractive pull towards the surface caused by attractive surface forces. If the stiffness is smaller than the force gradient, according to equation (1.2) it will jump-to-contact, remaining immobilised on the surface and unable to perform force measurements.

$$k_{min} > \frac{\partial F_{total}}{\partial d}. \quad (1.2)$$

With standard AFM cantilevers being mounted horizontally, the magnitude of said forces needs to be considered. For a typical silicon nitride cantilever positioned above a glass cover slip, the Van der Waals force gradient is given by

$$\frac{\partial F_{VdW}}{\partial d} = \frac{AR}{3d^3}. \quad (1.3)$$

where  $A$  is the Hamaker constant and  $R$  is the tip radius curvature [68]. Therefore the theoretical stiffness lower limit of a cantilever positioned at 12nm away from the surface is  $10^{-3}$ N/m. However, this assumes a motionless cantilever, when in fact the cantilever itself is subject to thermal noise which makes it oscillate around the equilibrium position [69]

$$\langle d^2 \rangle = \frac{k_B T}{k}. \quad (1.4)$$

For room temperature  $T$  the oscillation amplitude is around 2nm, which would result in the cantilever experiencing even larger forces as it approaches the surface. We can therefore conclude that horizontally oriented cantilevers need to be generally stiffer than  $10^{-3}$ N/m to perform non-contact measurements close to a surface.

One way of addressing this issue, is to change the effective stiffness of the cantilever by changing the angle from horizontal to vertical [70]. The intrinsic spring constant  $k$  of a cantilever, relates to the deflection  $d_{\perp}$  and the force normal  $F_{\perp}$  to the cantilever (see figure 1.2) as

$$k = -\frac{F_{\perp}}{d_{\perp}}. \quad (1.5)$$

With the strong attractive force being directed normal to the surface; tilting of the cantilever will affect the effective spring constant in the direction of choice as follows

$$k_z = -\frac{F_z}{d_z} = -\frac{F_z}{d_{\perp} \cos(\zeta)} \quad (1.6)$$

and by considering the intrinsic spring constant we find

$$d_{\perp} = -\frac{F_{\perp}}{k} = -\frac{F_z \cos(\zeta)}{k} \quad (1.7)$$

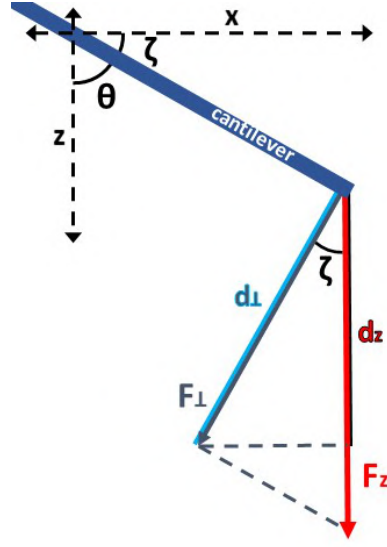


FIGURE 1.2. Diagram illustrating the cantilever tilt for the purpose of deriving vertical effective stiffness with respect to angle ( $\zeta$ )

and therefore

$$k_z = \frac{k}{\cos^2(\zeta)}. \quad (1.8)$$

From equation (1.8) we can conclude that, with the vertical orientation, it is possible to use much softer cantilevers without the risk of them 'jumping to contact' thanks to the system's new effective vertical stiffness. In theory as  $\zeta$  tends to  $90^\circ$  the minimum stiffness tends to 0, however in reality manufacturing will limit how soft the actual cantilever can be. Nevertheless, this orientation enables the use of cantilevers with stiffness of the order of  $10^{-5}\text{N/m}$ - $10^{-6}\text{N/m}$  (compared with  $10^1\text{N/m}$ - $10^{-3}\text{N/m}$  for a standard AFM cantilever) capable of measuring femtonewton forces, a regime mainly reserved for optical tweezers.

Another advantage of using VOP is a much greater tip-sample separation control. A vertical field gradient will also affect the tip-sample distance, this is particularly evident in optical tweezers where the effective vertical stiffness of the optical trap is much weaker than the attractive force gradient in the vertical direction. In this cases the surface needs to be passivated to prevent the bead from binding to the surface [71].

Further advantages of using vertically mounted, soft cantilevers can be found in the ability to image delicate structures as demonstrated by Fletcher et al. [72].

The Lateral Molecular Force Microscope used in this project and described later in detail (see

chapter 3) uses a particular type of ultra soft micro-fabricated cantilevers in a vertical orientation, which is crucial for investigating optical forces in evanescent fields. These fields in fact possess a large vertical force gradient, whilst their small decay length forces the probe to operate very close to the surface, where the inter-surface forces are significant.

As will be shown in this work, the use of vertically oriented micro-fabricated cantilevers opens up a completely new set of experiments to characterise optical near-fields.

## 1.6 Bibliography

- [1] M. v. Ardenne, “Das Elektronen-Rastermikroskop,” *Zeitschrift fur Physik*, p. 553, 1938.
- [2] R. P. Feynman, “There’s Plenty of Room at the Bottom,” p. 22, 1960.
- [3] C. Toumey, “Reading Feynman Into Nanotechnology: A Text for a New Science,” *Techné*, vol. 12:3 Fall, p. 36, 2008.
- [4] B. Guenther, *Modern Optics*. Oxford University Press, 2015.
- [5] M. C. Roco, “Nanotechnology: Convergence with modern biology and medicine,” *Current Opinion in Biotechnology*, vol. 14, pp. 337–346, June 2003.
- [6] B. L. M. Hendriksen and J. W. M. Frenken, “CO Oxidation on Pt(110): Scanning Tunneling Microscopy Inside a High-Pressure Flow Reactor,” *Physical Review Letters*, vol. 89, July 2002.
- [7] R. E. Franklin and R. G. Gosling, “The structure of sodium thymonucleate fibres. I. The influence of water content,” *Acta Crystallographica*, vol. 6, pp. 673–677, Sept. 1953.
- [8] A. Vasala, V. P. Hytönen, and O. H. Laitinen, “Modern Tools for Rapid Diagnostics of Antimicrobial Resistance,” *Frontiers in Cellular and Infection Microbiology*, vol. 10, p. 308, July 2020.
- [9] S. Dinarelli, M. Girasole, S. Kasas, and G. Longo, “Nanotools and molecular techniques to rapidly identify and fight bacterial infections,” *Journal of Microbiological Methods*, vol. 138, pp. 72–81, July 2017.

- [10] W. Xu, R. Mezencev, B. Kim, L. Wang, J. McDonald, and T. Sulchek, "Cell Stiffness Is a Biomarker of the Metastatic Potential of Ovarian Cancer Cells," *PLoS ONE*, vol. 7, p. e46609, Oct. 2012.
- [11] S. Frank, P. Poncharal, Z. L. Wang, and W. A. de Heer, "Carbon Nanotube Quantum Resistors," vol. 280, p. 4, 1998.
- [12] N. A. Burnham, R. J. Colton, and H. M. Pollock, "Interpretation of force curves in force microscopy," *Nanotechnology*, vol. 4, pp. 64–80, Apr. 1993.
- [13] A. Einstein, "Investigations On The Theory Of The Brownian Movement," *Annalen der Physik*, vol. 19, no. 4, pp. 371–381, 1906.
- [14] C. Veigel, "Moving into the cell: Single-molecule studies of molecular motors in complex environments," p. 14, 2011.
- [15] J. Worrall, "The pressure of light: The strange case of the vacillating 'crucial experiment'," *Studies in History and Philosophy of Science Part A*, vol. 13, pp. 133–171, June 1982.
- [16] J. C. Maxwell, *A Treatise on Electricity and Magnetism*. Cambridge Library Collection. Physical Sciences, Oxford, Clarendon press, 1873.
- [17] E. F. Nichols and G. F. Hull, "A Preliminary Communication on the Pressure of Heat and Light Radiation," *Physical Review (Series I)*, vol. 13, pp. 307–320, Nov. 1901.
- [18] P. N. Lebedev, "Experimental Examination Of Light Pressure," *Annalen der Physik*, vol. 6, p. 433, 1901.
- [19] J. H. Poynting, "On the Transfer of Energy in the Electromagnetic Field," *Philosophical Transactions of the Royal Society A: Mathematical, Physical and Engineering Sciences*, vol. 175, pp. 343–361, 1884.
- [20] J. Poynting, "Radiation pressure," *The London, Edinburgh, and Dublin Philosophical Magazine and Journal of Science*, vol. 9, pp. 393–406, Apr. 1905.

- [21] J. H. Poynting, “The wave motion of a revolving shaft, and a suggestion as to the angular momentum in a beam of circularly polarised light,” *Proceedings of the Royal Society A: Mathematical, Physical and Engineering Sciences*, vol. 82, pp. 560–567, 1909.
- [22] J. H. Poynting and G. Barlow, “Bakerian Lecture:—The pressure of light against the source: The recoil from light,” *Proceedings of the Royal Society A: Mathematical, Physical and Engineering Sciences*, vol. 83, pp. 534–546, 1910.
- [23] G. Barlow, “On the torque produced by a beam of light in oblique refraction through a glass plate,” *Proceedings of the Royal Society A: Mathematical, Physical and Engineering Sciences*, vol. 87, pp. 1–16, 1912.
- [24] M. Abraham, “Zur Elektrodynamik bewegter Körper,” *Rendiconti del Circolo Matematico di Palermo*, vol. 28, no. 1, 1909.
- [25] M. Abraham, “Sull’elettrodinamica di Minkowski,” *Rendiconti del Circolo Matematico di Palermo*, vol. 30, pp. 33–46, 1910.
- [26] H. Minkowski, “Die Grundgleichungen für die elektromagnetischen Vorgänge in bewegten Körpern,” *Nachrichten von der Gesellschaft der Wissenschaften zu Göttingen, Mathematisch-Physikalische Klasse*, pp. 53–111, 1908.
- [27] S. M. Barnett and R. Loudon, “The enigma of optical momentum in a medium,” *Philosophical Transactions of the Royal Society A: Mathematical, Physical and Engineering Sciences*, vol. 368, pp. 927–939, Mar. 2010.
- [28] S. M. Barnett, “Resolution of the Abraham-Minkowski Dilemma,” *Physical Review Letters*, vol. 104, Feb. 2010.
- [29] R. Loudon and C. Baxter, “Contributions of John Henry Poynting to the understanding of radiation pressure,” *Proceedings of the Royal Society A: Mathematical, Physical and Engineering Sciences*, vol. 468, pp. 1825–1838, 2012.
- [30] A. Einstein, “Zur elektrodynamik bewegter körper,” *Annalen der Physik*, vol. 4, pp. 891–921, 1905.

- [31] P. A. M. Dirac, “The Quantum Theory of the Emission and Absorption of Radiation,” *Proceedings of the Royal Society A: Mathematical, Physical and Engineering Sciences*, vol. 114, pp. 243–265, 1927.
- [32] P. A. M. Dirac, “The Quantum Theory of the Electron,” *Proceedings of the Royal Society A: Mathematical, Physical and Engineering Sciences*, vol. 117, p. 610, 1928.
- [33] P. A. M. Dirac, “A theory of electrons and protons,” *Proceedings of the Royal Society A: Mathematical, Physical and Engineering Sciences*, no. 126, p. 360, 1930.
- [34] C. D. Anderson, “The Positive Electron,” *Physical Review*, vol. 43, pp. 491–494, Mar. 1933.
- [35] F. Belinfante, “On the current and the density of the electric charge, the energy, the linear momentum and the angular momentum of arbitrary fields,” *Physica*, vol. 7, pp. 449–474, May 1940.
- [36] K. Y. Bliokh and Y. P. Bliokh, “Conservation of Angular Momentum, Transverse Shift, and Spin Hall Effect in Reflection and Refraction of an Electromagnetic Wave Packet,” *Physical Review Letters*, vol. 96, Feb. 2006.
- [37] K. Y. Bliokh and A. Aiello, “Goos–Hänchen and Imbert–Fedorov beam shifts: An overview,” *Journal of Optics*, vol. 15, p. 014001, Jan. 2013.
- [38] K. Y. Bliokh and Y. P. Bliokh, “Polarization, transverse shifts, and angular momentum conservation laws in partial reflection and refraction of an electromagnetic wave packet,” *Physical Review E*, vol. 75, June 2007.
- [39] F. I. Fedorov, “To the theory of total reflection,” *Journal of Optics*, vol. 15, p. 014002, Jan. 2013.
- [40] C. Imbert, “Calculation and Experimental Proof of the Transverse Shift Induced by Total Internal Reflection of a Circularly Polarized Light Beam,” *Physical Review D*, vol. 5, pp. 787–796, Feb. 1972.
- [41] K. Y. Bliokh, A. Y. Bekshaev, and F. Nori, “Extraordinary momentum and spin in evanescent waves,” *Nature Communications*, vol. 5, p. 3300, May 2014.



- [42] M. Antognozzi, C. R. Bermingham, R. L. Harniman, S. Simpson, J. Senior, R. Hayward, H. Hoerber, M. R. Dennis, A. Y. Bekshaev, K. Y. Bliokh, and F. Nori, “Direct measurements of the extraordinary optical momentum and transverse spin-dependent force using a nano-cantilever,” *Nature Physics*, vol. 12, pp. 731–735, Aug. 2016.
- [43] T. Maiman, “Stimulated Optical Radiation in Ruby,” *Nature*, vol. 187, pp. 493–494, 1960.
- [44] A. Ashkin, “Acceleration and Trapping of Particles by Radiation Pressure,” *Physical Review Letters*, vol. 24, pp. 156–159, Jan. 1970.
- [45] J. M. Dziedzic, J. E. Bjorkholm, and S. Chu, “Observation of a single-beam gradient force optical trap for dielectric particles,” *Optics Letters*, vol. 11, no. 5, p. 288, 1986.
- [46] A. Ashkin, “History of optical trapping and manipulation of small-neutral particle, atoms, and molecules,” *IEEE Journal of Selected Topics in Quantum Electronics*, vol. 6, pp. 841–856, Nov. 2000.
- [47] A. Ashkin and J. M. Dziedzic, “Optical Levitation by Radiation Pressure,” *Applied Physics Letters*, vol. 19, pp. 283–285, Oct. 1971.
- [48] S. Arnold, “Determination of particle mass and charge by one electron differentials,” *Journal of Aerosol Science*, vol. 10, pp. 49–53, Jan. 1979.
- [49] A. Ashkin, “Applications of Laser Radiation Pressure,” *Science*, vol. 210, pp. 1081–1088, Dec. 1980.
- [50] Y.-F. Chen, J. N. Milstein, and J.-C. Meiners, “Femtonewton Entropic Forces Can Control the Formation of Protein-Mediated DNA Loops,” *Physical Review Letters*, vol. 104, Jan. 2010.
- [51] H. He, M. E. J. Friese, N. R. Heckenberg, and H. Rubinsztein-Dunlop, “Direct Observation of Transfer of Angular Momentum to Absorptive Particles from a Laser Beam with a Phase Singularity,” *Physical Review Letters*, vol. 75, pp. 826–829, July 1995.
- [52] V. Svak, O. Brzobohatý, M. Šiler, P. Ják, J. Kaňka, P. Zemánek, and S. H. Simpson, “Transverse spin forces and non-equilibrium particle dynamics in a circularly polarized vacuum optical trap,” *Nature Communications*, vol. 9, p. 5453, Dec. 2018.

- [53] L. Allen, M. W. Beijersbergen, R. J. C. Spreeuw, and J. P. Woerdman, “Orbital angular momentum of light and the transformation of Laguerre-Gaussian laser modes,” *Physical Review A*, vol. 45, pp. 8185–8189, June 1992.
- [54] D. Gao, W. Ding, M. Nieto-Vesperinas, X. Ding, M. Rahman, T. Zhang, C. Lim, and C.-W. Qiu, “Optical manipulation from the microscale to the nanoscale: Fundamentals, advances and prospects,” *Light: Science & Applications*, vol. 6, pp. e17039–e17039, Sept. 2017.
- [55] G. Binnig, H. Rohrer, C. Gerber, and E. Weibel, “Tunneling through a controllable vacuum gap,” *Applied Physics Letters*, vol. 40, pp. 178–180, Jan. 1982.
- [56] G. Binnig, H. Rohrer, C. Gerber, and E. Weibel, “Surface Studies by Scanning Tunneling Microscopy,” *Physical Review Letters*, vol. 49, pp. 57–61, July 1982.
- [57] G. Binnig, H. Rohrer, C. Gerber, and E. Weibel, “ $7 \times 7$  Reconstruction on Si(111) Resolved in Real Space,” *Physical Review Letters*, vol. 50, pp. 120–123, Jan. 1983.
- [58] G. Binnig, C. F. Quate, and C. Gerber, “Atomic Force Microscope,” *Physical Review Letters*, vol. 56, pp. 930–933, Mar. 1986.
- [59] F. J. Giessibl and H. Bielefeldt, “Physical interpretation of frequency-modulation atomic force microscopy,” *Physical Review B*, vol. 61, pp. 9968–9971, Apr. 2000.
- [60] D. C. Kohlgraf-Owens, S. Sukhov, and A. Dogariu, “Mapping the mechanical action of light,” *Physical Review A*, vol. 84, July 2011.
- [61] D. C. Kohlgraf-Owens, S. Sukhov, and A. Dogariu, “Near-Field Topography of Light,” *Optics and Photonics News*, vol. 23, p. 39, Dec. 2012.
- [62] D. C. Kohlgraf-Owens, S. Sukhov, L. Greusard, Y. De Wilde, and A. Dogariu, “Optically induced forces in scanning probe microscopy,” *Nanophotonics*, vol. 3, Jan. 2014.
- [63] D. W. Pohl, W. Denk, and M. Lanz, “Optical stethoscopy: Image recording with resolution  $\lambda/20$ ,” *Applied Physics Letters*, vol. 44, pp. 651–653, Apr. 1984.

- [64] U. Dürig, D. W. Pohl, and F. Rohner, “Near-field optical-scanning microscopy,” *Journal of Applied Physics*, vol. 59, pp. 3318–3327, May 1986.
- [65] Y. De Wilde, P.-A. Lemoine, D. G. Seiler, A. C. Diebold, R. McDonald, C. M. Garner, D. Herr, R. P. Khosla, and E. M. Secula, “Review of NSOM Microscopy for Materials,” in *AIP Conference Proceedings*, vol. 931, (Gaithersburg, MD), pp. 43–52, AIP, 2007.
- [66] M. Antognozzi, A. Ulcinas, L. Picco, S. H. Simpson, P. J. Heard, M. D. Szczelkun, B. Brenner, and M. J. Miles, “A new detection system for extremely small vertically mounted cantilevers,” *Nanotechnology*, vol. 19, p. 384002, Sept. 2008.
- [67] R. L. Harniman, J. A. Vicary, J. K. H. Hörber, L. M. Picco, M. J. Miles, and M. Antognozzi, “Methods for imaging DNA in liquid with lateral molecular-force microscopy,” *Nanotechnology*, vol. 23, p. 085703, Mar. 2012.
- [68] N. A. Burnham and R. J. Colton, “Measuring the nanomechanical properties and surface forces of materials using an atomic force microscope,” *Journal of Vacuum Science & Technology A: Vacuum, Surfaces, and Films*, vol. 7, pp. 2906–2913, July 1989.
- [69] J. L. Hutter and J. Bechhoefer, “Calibration of atomic-force microscope tips,” *Review of Scientific Instruments*, vol. 64, pp. 1868–1873, July 1993.
- [70] P. Attard, A. Carambassis, and M. W. Rutland, “Dynamic Surface Force Measurement. 2. Friction and the Atomic Force Microscope,” *Langmuir*, vol. 15, pp. 553–563, Jan. 1999.
- [71] C. Tischer, S. Altmann, S. Fišinger, J. K. H. Hörber, E. H. K. Stelzer, and E.-L. Florin, “Three-dimensional thermal noise imaging,” *Applied Physics Letters*, vol. 79, pp. 3878–3880, Dec. 2001.
- [72] J. M. Fletcher, R. L. Harniman, F. R. H. Barnes, A. L. Boyle, A. Collins, J. Mantell, T. H. Sharp, M. Antognozzi, P. J. Booth, N. Linden, M. J. Miles, R. B. Sessions, P. Verkade, and D. N. Woolfson, “Self-Assembling Cages from Coiled-Coil Peptide Modules,” *Science*, vol. 340, pp. 595–599, May 2013.

## OPTICAL FORCES IN THE EVANESCENT FIELD

## 2.1 Optical Forces

## 2.1.1 Electromagnetic stress-energy tensor

The electromagnetic stress-energy tensor  $\mathbf{T}_{em}^{\mu\nu}$  (in Minkowski notation) is a relativistic version of the Maxwell second order stress tensor and it describes the flow of energy and momentum of the electromagnetic field as well as its interaction with the medium in which it is propagating. In 1940 F.J. Belinfante [1] added a new term to the electromagnetic stress-energy tensor in order to ensure it is symmetric and gauge-invariant. The new term is given by

$$\mathbf{T}_{spin}^{\mu\nu} = -\frac{1}{\mu_0} \partial_\tau (A^\mu F^{\nu\tau}) \quad (2.1)$$

and the electromagnetic stress-energy tensor become:

$$\mathbf{T}_{em}^{\mu\nu} = \mathbf{T}_{old}^{\mu\nu} + \mathbf{T}_{spin}^{\mu\nu} = -\frac{1}{\mu_0} \left( F^\mu{}_\tau F^{\nu\tau} - \frac{1}{4} \eta^{\mu\nu} F^{\rho\sigma} F_{\rho\sigma} \right) \quad (2.2)$$

where  $\mu_0$  is the permeability of free space (or magnetic constant),  $F^{\mu\nu}$  is the Faraday field tensor

$$F^{\mu\nu} = \begin{pmatrix} 0 & E_x/c & E_y/c & E_z/c \\ E_x/c & 0 & B_z & -B_y \\ E_y/c & -B_z & 0 & B_x \\ E_z/c & B_y & -B_x & 0 \end{pmatrix} \quad (2.3)$$

where  $\epsilon_0$  is the permittivity of free space (or electric constant) and  $\mathbf{E}$  and  $\mathbf{B}$  are the electric field and magnetic flux density respectively.  $\eta^{\mu\nu}$  is the Minkowski metric given by

$$\eta^{\mu\nu} = \begin{pmatrix} 1 & 0 & 0 & 0 \\ 0 & -1 & 0 & 0 \\ 0 & 0 & -1 & 0 \\ 0 & 0 & 0 & -1 \end{pmatrix} \quad (2.4)$$

and  $A^\mu$  is the electromagnetic four-potential. In fact for  $T_{em}^{00}$  we find [2, 3]

$$\mathbf{T}_{em}^{00} = -\frac{1}{\mu_0} \left( F^0{}_\tau F^{0\tau} - \frac{1}{4} \eta^{00} F^{\rho\sigma} F_{\rho\sigma} \right) = \frac{1}{2} \left( \epsilon_0 |\mathbf{E}|^2 + \frac{1}{\mu_0} |\mathbf{B}|^2 \right) = W \quad (2.5)$$

which is the energy density  $W$  of an electromagnetic field, Substituting equations (2.3) and (2.4) into equation (2.2), the electromagnetic stress-energy tensor can be rewritten as

$$\mathbf{T}_{em}^{\mu\nu} = \begin{pmatrix} W & \wp_j/c \\ \wp_i/c & \mathbf{M}_{ij} \end{pmatrix} \quad (2.6)$$

where  $\mathbf{M}_{ij}$  is the Maxwell's stress tensor and is given by

$$\mathbf{M}_{ij} = \epsilon_0 E_i E_j + \frac{1}{\mu_0} B_i B_j - W \delta_{ij} \quad (2.7)$$

with  $\delta_{ij}$  being the Kronecker's delta (with  $i, j = \{x, y, z\}$ ) and where  $\wp$  is the energy flow density known as the Poynting vector, given (in vacuum) by

$$\wp = \frac{1}{\mu_0} (\mathbf{E} \times \mathbf{B}). \quad (2.8)$$

In fact the Maxwell's stress tensor  $\mathbf{M}_{ij}$  can be used to evaluate the mechanical forces of the electromagnetic field (over the full oscillation period of the wave) acting on an object within a given enclosed surface  $S$  [4–6]

$$\langle \mathbf{F} \rangle = \int_S \langle \mathbf{M}_{ij} \rangle \cdot \mathbf{n} dS \quad (2.9)$$

where  $\mathbf{n}$  is the unit vector perpendicular to the surface and where the angle brackets  $\langle \dots \rangle$  denote time average. In a very similar manner it can also be used to calculate the optical torque  $\mathbf{Y}$  on a rigid object

$$\langle \mathbf{Y} \rangle = \int_S \langle \mathbf{M}_{ij} \times \mathbf{r} \rangle \cdot \mathbf{n} dS \quad (2.10)$$

where  $\mathbf{r}$  is the position vector.

### 2.1.2 Dipole approximation for small small particles

A charged particle in an electromagnetic field experiences a force acting on it. The well known Lorentz Force can also be used as a starting point to evaluate optical forces acting on sub-wavelength-sized objects in so called dipole approximation [3, 5, 7]. The Rayleigh regime where the dimension  $a$  of the particle satisfies the scattering condition when interacting with a wave of wavenumber  $k$

$$ka \ll 1 \quad (2.11)$$

opens up the possibility to consider optical forces and their nature in an analytical manner. This limit allows for much simpler calculation of forces than in Mie regime [8–10] where the particles are of similar size as the wavelength and the contributions from scattering, reflection, refraction and finally the size and shape of the object have to be carefully considered [9–11].

The force experienced by a charge (moving with velocity  $\mathbf{v}$ ) in an electromagnetic field is given by the Lorentz force [5]

$$\mathbf{F}(\mathbf{r}, t) = q[\mathbf{E}(\mathbf{r}, t) + \mathbf{v}(\mathbf{r}, t) \times \mathbf{B}(\mathbf{r}, t)] \quad (2.12)$$

which can also be generalised in terms of charge density  $\rho$  and current flow  $\mathbf{j}(\mathbf{r}, t)$

$$\mathbf{F}(\mathbf{r}, t) = \int_V [\rho(\mathbf{r}, t)\mathbf{E}(\mathbf{r}, t) + \mathbf{j}(\mathbf{r}, t) \times \mathbf{B}(\mathbf{r}, t)] dV. \quad (2.13)$$

Rayleigh particles can be approximated to a point like dipole consisting of two opposite charges positioned infinitesimally close to one another [5] and possessing the dipole moment  $\mathbf{d}_p$

$$\mathbf{d}_p = q(\mathbf{r}_1 - \mathbf{r}_2) \quad (2.14)$$

alternatively, the particle can become polarised as a result of an applied  $\mathbf{E}$  field

$$\mathbf{d}_p = \alpha \mathbf{E} \quad (2.15)$$

where  $\alpha$  is the complex polarisability

$$\alpha = \alpha' + i\alpha''. \quad (2.16)$$

Introducing the dipole moment into equation (2.12) one can find a time-averages force over a whole oscillation period (where  $\omega$  is the frequency of the oscillation) to be [5]

$$\langle \mathbf{F} \rangle = \frac{1}{2} \text{Re} \left( \mathbf{d}_p^* \cdot \nabla \right) \mathbf{E} - i\omega \left( \mathbf{d}_p^* \times \mathbf{B} \right). \quad (2.17)$$

Assuming a small velocity of the dipole compared to the speed of light  $c$  and using (2.16) and (2.15), we can write the time-averaged force (2.17) as

$$\langle \mathbf{F} \rangle = \frac{\alpha'}{2} \text{Re}(\mathbf{E}^* \nabla \mathbf{E}) + \frac{\alpha''}{2} \text{Im}(\mathbf{E}^* \nabla \mathbf{E}), \quad (2.18)$$

which can be rewritten as

$$\langle \mathbf{F} \rangle = \frac{1}{4} \text{Re}(\alpha_e) \nabla |\mathbf{E}|^2 + \frac{1}{2} \text{Im}(\alpha_e) \text{Im}(\mathbf{E}^* \nabla \mathbf{E}) \quad (2.19)$$

where the first term can be identified as the well known gradient force and the second as the scattering force [5].

### 2.1.3 Analytical model for optical forces acting on small particles

In 2007 Bekshaev and Soskin [12] and later in 2009 M.V. Berry [13] suggested a decomposition of the Poynting vector  $\wp$  (eq.2.8) in its time averaged form and associating it with the momentum density  $\mathbf{P}$

$$\langle \wp \rangle = \frac{cg}{2} \text{Re}(\mathbf{E}^* \times \mathbf{H}) = \mathbf{P}/c^2. \quad (2.20)$$

For the remainder of this chapter the background medium is considered and Gaussian units are used with  $g = 1/4\pi$  as the gaussian unit factor. As a result, the momentum density  $\mathbf{P}$  can be expressed as [12, 13]

$$\mathbf{P} = \frac{g}{2\omega} \left( \left[ \text{Im} \frac{1}{\mu} \mathbf{E}^* \cdot (\nabla) \mathbf{E} + \text{Im} \frac{1}{\varepsilon} \mathbf{H}^* \cdot (\nabla) \mathbf{H} \right] + \left[ \frac{1}{2\mu} \nabla(\mathbf{E}^* \times \mathbf{E}) + \frac{1}{2\varepsilon} \nabla(\mathbf{H}^* \times \mathbf{H}) \right] \right) \quad (2.21)$$

where the following notation has been used [14]

$$\mathbf{E}^* \cdot (\nabla) \mathbf{E} = E_x^* \nabla E_x + E_y^* \nabla E_y + E_z^* \nabla E_z. \quad (2.22)$$

The first two expressions on the right hand side of equation (2.21) can be identified as the electric and magnetic contributions to the orbital momentum density, whilst the remaining two expressions can be identified as the electric and magnetic contribution to spin momentum density

$$\mathbf{P} = [\mathbf{P}_e^o + \mathbf{P}_m^o] + [\mathbf{P}_e^s + \mathbf{P}_m^s] = \mathbf{P}^o + \mathbf{P}^s. \quad (2.23)$$

Thus equation (2.23) shows that the Poynting vector is a sum of 2 momentum densities with different physical origin and that parity of electric and magnetic fields is satisfied. It is worth revisiting the

energy density of the field (2.5) which can easily be shown to be made of an electric and a magnetic part [15]

$$W = \frac{g}{2} (\epsilon |\mathbf{E}|^2 + \mu |\mathbf{H}|^2) = W_e + W_m. \quad (2.24)$$

The force experienced by a particle in the dipole approximation is made out of its electric, magnetic and electromagnetic parts [3, 16, 17]

$$\mathbf{F} = \mathbf{F}_e + \mathbf{F}_m + \mathbf{F}_{em}. \quad (2.25)$$

Equation (2.19) in section 2.1.2 is the expression for the electric contribution to the total dipole force. In fact one can easily identify that the first expression the right hand side is associated with the energy density of the field  $W_e$  and the second term is associated with the orbital momentum density  $\mathbf{P}_e^o$  [18, 19]

$$\mathbf{F}_e = \frac{1}{2g\epsilon} \text{Re}(\alpha_e) \nabla W_e + \frac{\omega\mu}{g} \text{Im}(\alpha_e) \mathbf{P}_e^o. \quad (2.26)$$

Following the same derivation it can be shown that the magnetic contribution to the total force experienced by the dipole is given by [18]

$$\mathbf{F}_m = \frac{1}{2g\mu} \text{Re}(\alpha_m) \nabla W_m + \frac{\omega\epsilon}{g} \text{Im}(\alpha_m) \mathbf{P}_m^o \quad (2.27)$$

and is analogous to the electric contribution  $\mathbf{F}_e$ . The final part of the total force acting on the particle has both electric and magnetic contributions and can be written as [18]

$$\mathbf{F}_{em} = -\frac{\omega}{3g} k^3 \text{Re}(\alpha_e^* \alpha_m) (\mathbf{P}^o + \mathbf{P}^s) + \frac{\omega}{3c} k^3 \text{Im}(\alpha_e^* \alpha_m) \text{Im}(\mathbf{E}^* \times \mathbf{H}) \quad (2.28)$$

where the imaginary term is the contribution from the Imaginary Poynting vector  $\mathbf{P}^i$  defined as

$$\mathbf{P}^i = \frac{g}{c} \text{Im}(\mathbf{E}^* \times \mathbf{H}). \quad (2.29)$$

Equations (2.26)-(2.28) show that the electromagnetic interaction depending on particle's polarisabilities  $\alpha_e$  and  $\alpha_m$  induce forces of different physical origins. Which leads to a notion that the equation (2.25) can be rewritten to reflect just that [17]

$$\mathbf{F} = \mathbf{F}^g + \mathbf{F}^o + \mathbf{F}^s + \mathbf{F}^i. \quad (2.30)$$



The first parts of equations (2.26) and (2.27) is the gradient of the energy density and can be identified as the gradient force contribution

$$\mathbf{F}^g = \frac{1}{2g\epsilon} \text{Re}(\alpha_e) \nabla W_e + \frac{1}{2g\mu} \text{Re}(\alpha_m) \nabla W_m. \quad (2.31)$$

The force due to orbital momentum density  $\mathbf{F}^o$  is given by

$$\mathbf{F}^o = \frac{\omega}{g} \left( \left( \mu \text{Im}(\alpha_e) - \frac{k^3}{3} \text{Re}(\alpha_e^* \alpha_m) \right) \mathbf{P}_e^0 + \left( \epsilon \text{Im}(\alpha_m) - \frac{k^3}{3} \text{Re}(\alpha_e^* \alpha_m) \right) \mathbf{P}_m^0 \right), \quad (2.32)$$

and the force associated with spin momentum density  $\mathbf{F}^s$  is

$$\mathbf{F}^s = -\frac{\omega}{3g} k^3 \text{Re}(\alpha_e^* \alpha_m) \mathbf{P}^s. \quad (2.33)$$

The final contribution  $\mathbf{F}^i$  is derived from the imaginary part of the Poynting vector

$$\mathbf{F}^i = \frac{\omega}{3g} k^3 \text{Im}(\alpha_e^* \alpha_m) \mathbf{P}^i \quad (2.34)$$

The decomposition shown in equation (2.30) allows us to give the force experienced by a dipole particle a strong physical meaning.

## 2.2 Evanescent Field

### 2.2.1 Theoretical description

Evanescent wave or near field is a sub-wavelength region of electromagnetic field. Analogous in its mathematical description to the quantum tunneling, this exponentially decaying field is most often created during total internal reflection (TIR) of a wave.

From Snell's law

$$n_i \sin(\alpha) = n_f \sin(\beta) \quad (2.35)$$

which describes the dependence of the refraction angle  $\beta$  on the incident angle  $\alpha$  as well as the refractive indices of the corresponding media ( $n_f$  and  $n_i$  respectively, with indices  $i$  and  $f$  standing for 'incident' and 'final' used from here on in), arises the condition for total internal reflection when

$$\alpha > \arcsin^{-1}(n_r/n_i) \quad (2.36)$$

A convenient way of describing an evanescent field is by rotating a plane wave by an imaginary angle ( $\psi$ ) [9, 20]. The incident polarised electromagnetic field propagating along the z-axis can be defined using the wavevector

$$\mathbf{k} = \begin{pmatrix} 0 \\ 0 \\ k \end{pmatrix}, \quad (2.37)$$

where  $k$  is the wave number  $k = n_i k_0 = n_i \frac{2\pi}{\lambda_0}$  (with  $k_0$  and  $\lambda_0$  being the wave number and wavelength in free space respectively) and can be written as

$$\mathbf{E}_i = \frac{A_i \sqrt{\mu}}{\sqrt{1 + |m_i|^2}} \begin{pmatrix} 1 \\ m_i \\ 0 \end{pmatrix} e^{ikz}, \quad (2.38)$$

$$\mathbf{H}_i = \frac{A_i \sqrt{\epsilon}}{\sqrt{1 + |m_i|^2}} \begin{pmatrix} -m_i \\ 1 \\ 0 \end{pmatrix} e^{ikz}. \quad (2.39)$$

where the wave amplitude is  $A_i$  and where

$$m_i = \frac{E_{iy}}{E_{ix}} \quad (2.40)$$

is a complex number characterizing the polarisation of the wave [9].

To rotate the propagation direction of the plane wave a rotation matrix (about the transverse y-axis) is used

$$\hat{R}_y(\psi) = \begin{pmatrix} \cos(\psi) & 0 & \sin(\psi) \\ 0 & 1 & 0 \\ -\sin(\psi) & 0 & \cos(\psi) \end{pmatrix} = \begin{pmatrix} \cosh(\gamma) & 0 & i \sinh(\gamma) \\ 0 & 1 & 0 \\ -i \sinh(\gamma) & 0 & \cosh(\gamma) \end{pmatrix}, \quad (2.41)$$

where  $\psi$  is an imaginary angle  $\psi = i\gamma$ . The rotation matrix is applied to the spatial distribution of the field as well as the vector components of both the electric and magnetic parts of the wave  $\mathbf{E}$ , giving

$$\mathbf{E}_f = \frac{A_f \sqrt{\mu}}{\sqrt{1 + |m_f|^2}} \begin{pmatrix} 1 \\ m_f k/k_z \\ -i\kappa/k_z \end{pmatrix} e^{ik_z z - \kappa x} \quad (2.42)$$

and

$$\mathbf{H}_f = \frac{A_f \sqrt{\epsilon}}{\sqrt{1 + |m_f|^2}} \begin{pmatrix} -m_f \\ k/k_z \\ i m_f \kappa / k_z \end{pmatrix} e^{i k_z z - \kappa x} \quad (2.43)$$

where  $k_z$  is the conserved component of the wavevector (see figure 2.1) along the z-axis and is given by

$$k_z = k_0 n_i \sin(\alpha) = k_0 n_f \cosh(\gamma) \quad (2.44)$$

and where  $\kappa$  is the imaginary component along the x-axis given by

$$\kappa = k_0 n_f \sinh(\gamma), \quad (2.45)$$

satisfying  $k_z^2 - \kappa^2 = k^2$  relation.

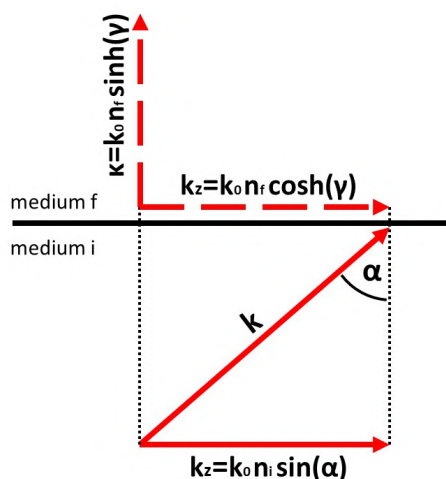


FIGURE 2.1. Diagram of the  $k$ -vectors of the incident beam, at an angle ( $\alpha$ ), and the resultant evanescent field.

The resulting amplitude and the polarisation number are

$$A_f = \frac{k_z}{k} \sqrt{\frac{1 + |m_f|^2}{1 + |m_i|^2}} T_p A_i \quad (2.46)$$

and

$$m_f = \frac{T_s}{T_p} m_i. \quad (2.47)$$

Both of which include the Fresnel transmission coefficients given by

$$T_s = \frac{2 n_i \cos(\alpha)}{n_i \cos(\alpha) + i n_f \sinh(\gamma)} \quad (2.48)$$

$$T_s = \frac{2n_i \cos(\alpha)}{n_f \cos(\alpha) + i n_i \sinh(\gamma)} \quad (2.49)$$

### 2.2.2 Polarisation

Polarisation is a geometrical property of any transverse wave which can describe the direction of its oscillation. For the electromagnetic fields it describes the direction of the electric and magnetic fields, which are always orthogonal to each other. One of the most common ways to describe polarisation states is through the use of Stokes parameters [5, 9, 21]

$$\tau = \frac{1 - |m|^2}{1 + |m|^2} \quad (2.50)$$

$$\chi = \frac{2\text{Re}[m]}{1 + |m|^2} \quad (2.51)$$

$$\sigma = \frac{2\text{Im}[m]}{1 + |m|^2} \quad (2.52)$$

where  $m$  was defined in equation (2.40).

#### 2.2.2.1 Mathematical description of the Stokes parameters for the LMFM systems

Reconciling the theoretical description with the actual experimental setup, requires the description of the polarisation of the evanescent field generated in the Lateral Molecular Force Microscope (which will be described in chapter 3 section 3.4.1). In the setup, the polarisation is controlled using a liquid crystal variable retarder, quarter-wave plate and linear polariser (or a combination of any of them in said order). After initial polarisation control, the beam reflects off a right-angled mirror, leading to a change in the direction of the  $\mathbf{k}$  vector (which corresponds to a change from left to right circularly polarised light). The calculations of the transformations of the incoming beam is presented below for each of the optical components.

A generalized formula for a waveplate effect on the polarised beam can be found using Jones calculus [22]. In order to find a matrix describing an arbitrarily rotated waveplate with an arbitrary retardance, a rotation matrix  $R(\phi)$  needs to be applied to a general phase retarder matrix  $M_P$  as

follows

$$\begin{aligned}
 M_{A,P}(\phi) &= R(-\phi) M_P R(\phi) \\
 &= \begin{pmatrix} \cos(\phi) & -\sin(\phi) \\ \sin(\phi) & \cos(\phi) \end{pmatrix} \begin{pmatrix} e^{-i\delta} & 0 \\ 0 & 1 \end{pmatrix} \begin{pmatrix} \cos(\phi) & \sin(\phi) \\ -\sin(\phi) & \cos(\phi) \end{pmatrix} \\
 &= \begin{pmatrix} e^{-i\delta} \cos^2(\phi) + \sin^2(\phi) & (e^{-i\delta} - 1) \sin(\phi) \cos(\phi) \\ (e^{-i\delta} - 1) \sin(\phi) \cos(\phi) & \cos^2(\phi) + e^{-i\delta} \sin^2(\phi) \end{pmatrix}.
 \end{aligned} \tag{2.53}$$

With the incoming field propagating along the z-axis and the beam being polarised along the y-axis (s-polarisation), the retarder will have the following effect

$$\begin{aligned}
 \mathbf{E}^{WP} &= E_0 \begin{pmatrix} E_x^{WP} \\ E_y^{WP} \end{pmatrix} e^{ikz} = M_{A,P}(\phi) E_0 \begin{pmatrix} 0 \\ 1 \end{pmatrix} e^{ikz} \\
 &= E_0 \begin{pmatrix} (e^{-i\delta} - 1) \sin(\phi) \cos(\phi) \\ \cos^2(\phi) + e^{-i\delta} \sin^2(\phi) \end{pmatrix} e^{ikz}
 \end{aligned} \tag{2.54}$$

where  $E_x^{WP}$  can be simplified as

$$\begin{aligned}
 E_x^{WP} &= (e^{-i\delta} - 1) \sin(\phi) \cos(\phi) \\
 &= e^{-i\delta/2} e^{i\delta/2} (e^{-i\delta} - 1) \sin(\phi) \cos(\phi) \\
 &= e^{-i\delta/2} (e^{-i\delta/2} - e^{i\delta/2}) \sin(\phi) \cos(\phi) \\
 &= e^{-i\delta/2} (-2i \sin(\delta/2)) \sin(\phi) \cos(\phi) \\
 &= -ie^{-i\delta/2} \sin(\delta/2) \sin(2\phi)
 \end{aligned} \tag{2.55}$$

and where  $E_y^{WP}$  can be simplified as

$$\begin{aligned}
 E_y^{WP} &= \cos^2(\phi) + e^{-i\delta} \sin^2(\phi) \\
 &= (\cos^2(\phi) + e^{-i\delta} \sin^2(\phi)) (-ie^{-i\delta/2} e^{i\delta/2}) \\
 &= -ie^{-i\delta/2} (\cos^2(\phi) (ie^{i\delta/2}) + (ie^{-i\delta/2}) \sin^2(\phi)) \\
 &= -ie^{-i\delta/2} (i \cos^2(\phi) (\cos(\delta/2) + i \sin(\delta/2)) + i (\cos(\delta/2) - i \sin(\delta/2)) \sin^2(\phi)) \\
 &= -ie^{-i\delta/2} (i \cos(\delta/2) (\cos^2(\phi) + \sin^2(\phi)) + \sin(\delta/2) (\cos^2(\phi) - \sin^2(\phi))) \\
 &= -ie^{-i\delta/2} (i \cos(\delta/2) + \sin(\delta/2) \cos(2\phi)).
 \end{aligned} \tag{2.56}$$

Substituting equations (2.55) and (2.56) into equation (2.54) and omitting  $-ie^{-i\delta/2}$  we get

$$\mathbf{E}^{WP} = E_0 \begin{pmatrix} \sin(\delta/2) \sin(2\phi) \\ i \cos(\delta/2) + \sin(\delta/2) \cos(2\phi) \end{pmatrix} e^{ikz}. \quad (2.57)$$

Similar to the equation (2.53) a matrix for transformation due to a linear polariser can be generalised as

$$\begin{aligned} M_{Lpol}(\phi) &= \begin{pmatrix} \cos(\phi) & -\sin(\phi) \\ \sin(\phi) & \cos(\phi) \end{pmatrix} \begin{pmatrix} 1 & 0 \\ 0 & 0 \end{pmatrix} \begin{pmatrix} \cos(\phi) & \sin(\phi) \\ -\sin(\phi) & \cos(\phi) \end{pmatrix} \\ &= \begin{pmatrix} \cos^2(\phi) & \sin(\phi) \cos(\phi) \\ \sin(\phi) \cos(\phi) & \sin^2(\phi) \end{pmatrix} \end{aligned} \quad (2.58)$$

Which for p-polarised light and s-polarised light respectively light is equivalent to the following

$$\begin{aligned} M_{Ppol} &= \begin{pmatrix} 1 & 0 \\ 0 & 0 \end{pmatrix} \\ M_{Spol} &= \begin{pmatrix} 0 & 0 \\ 0 & 1 \end{pmatrix} \end{aligned} \quad (2.59)$$

For experiments aimed at measuring optical forces associated with circularly polarised light, the quarter-wave plate has been used as the optical element affecting the polarisation state of the evanescent field. Hence using equation (2.68) we can express the polarisation parameter  $m$  (see equation (2.40)), before it enters the objective lens, as [21]

$$m_i = \frac{-i \cos(\delta/2) - \sin(\delta/2) \cos(2\phi)}{\sin(\delta/2) \sin(2\phi)} = \frac{-\cos(2\phi) - i \cot(\delta/2)}{\sin(2\phi)}. \quad (2.60)$$

where the acquired sign change is due to the beam reflecting off a right-angled mirror. The reflection leads to a change in the direction of the  $\mathbf{k}$  vector, and so to preserve the coordinate system, the orientation of x-axis needs to be flipped. In order to rewrite the Stokes parameters (2.50) to (2.52) for our system, the following relations which originate from trigonometric identities as well as equation (2.44) can be used

$$\begin{aligned} \sinh^2(\gamma) &= \cosh^2(\gamma) - 1 \\ n_i^2 \sin^2(\alpha) &= n_f^2 \cosh^2(\gamma) \\ n_i^2 \cos^2(\alpha) &= n_i^2 - n_f^2 \cosh^2(\gamma). \end{aligned} \quad (2.61)$$

With  $n_f = 1$ , the polarisation coefficient  $m_f$  is given by

$$\begin{aligned}
 m_f &= m_i \frac{T_s}{T_p} = m_i \frac{\cos(\alpha) + i n_i \sinh(\gamma)}{n_i \cos(\alpha) + i \sinh(\gamma)} \\
 &= m_i \left( \frac{(\cos(\alpha) + i n_i \sinh(\gamma))(n_i \cos(\alpha) - i \sinh(\gamma))}{n_i^2 \cos^2(\alpha) + \sinh^2(\gamma)} \right) \\
 &= m_i \left( \frac{n_i \cos^2(\alpha) + n_i \sinh^2(\gamma)}{n_i^2 \cos^2(\alpha) + \sinh^2(\gamma)} + i \frac{n_i^2 \cos(\alpha) \sinh(\gamma) - \cos(\alpha) \sinh(\gamma)}{n_i^2 \cos^2(\alpha) + \sinh^2(\gamma)} \right) \\
 &= m_i \left( \frac{n_i (\cos^2(\alpha) + \sinh^2(\gamma))}{n_i^2 \cos^2(\alpha) + \sinh^2(\gamma)} + i \frac{(n_i^2 - 1) \cos(\alpha) \sinh(\gamma)}{n_i^2 \cos^2(\alpha) + \sinh^2(\gamma)} \right) \\
 &= m_i \left( \frac{n_i (\cosh^2(\gamma) - \sin^2(\alpha))}{(n_i^2 - 1)} + i \frac{(n_i^2 - 1) \cos(\alpha) \sinh(\gamma)}{(n_i^2 - 1)} \right) \\
 &= m_i \left( \frac{n_i (\cosh^2(\gamma) - \sin^2(\alpha))}{(n_i^2 - 1)} + i \cos(\alpha) \sinh(\gamma) \right) \\
 &= \frac{\cos(2\phi) + i \cot(\delta/2)}{\sin(2\phi)} \left( \frac{(n_i^2 - 1) \cosh(\gamma) \sin(\alpha)}{(n_i^2 - 1)} + i \cos(\alpha) \sinh(\gamma) \right) \\
 &= \frac{\cosh(\gamma) \sin(\alpha) \cos(2\phi) - \sinh(\gamma) \cos(\alpha) \cot(\delta/2)}{\sin(2\phi)} \\
 &\quad + i \frac{\cosh(\gamma) \sin(\alpha) \cot(\delta/2) + \sinh(\gamma) \cos(\alpha) \cos(2\phi)}{\sin(2\phi)}.
 \end{aligned} \tag{2.62}$$

Knowing that

$$\begin{aligned}
 |m_f|^2 &= |m_i|^2 |T_s|^2 \left| \frac{1}{T_p} \right|^2 \\
 &= |m_i|^2 \left( \frac{4n_i^4 \cos^4(\alpha) + 4n_i^2 \cos^2(\alpha) \sinh^2(\gamma)}{(n_i^2 \cos^2(\alpha) + \sinh^2(\gamma))^2} \right) \left( \frac{\cos^2(\alpha) + n_i^2 \sinh^2(\gamma)}{4n_i^2 \cos^2(\alpha)} \right) \\
 &= |m_i|^2 \left( \frac{1}{n_i^2 \cos^2(\alpha) + \sinh^2(\gamma)} \right) \left( \frac{\cos^2(\alpha) + n_i^2 \sinh^2(\gamma)}{1} \right) \\
 &= |m_i|^2 \left( \frac{\cos^2(\alpha) + n_i^2 (\cosh^2(\gamma) - (\cos^2(\alpha) + \sin^2(\alpha)))}{(n_i^2 - 1)} \right) \\
 &= \left( \frac{(\cos^2(2\phi) + \cot^2(\delta/2))}{\sin^2(2\phi)} \right) \left( \frac{-(n_i^2 - 1) \cos^2(\alpha) + (n_i^2 - 1) \cosh^2(\gamma)}{(n_i^2 - 1)} \right) \\
 &= \frac{(\cos^2(2\phi) + \cot^2(\delta/2)) (\cosh^2(\gamma) - \cos^2(\alpha))}{\sin^2(2\phi)},
 \end{aligned} \tag{2.63}$$

we can express the Stokes parameters (given by (2.50) to (2.52)) for our system as [21]

$$\tau(\phi) = \frac{\sin^2(2\phi) - (\cos^2(2\phi) + \cot^2(\delta/2)) (\cosh^2(\gamma) - \cos^2(\alpha))}{\sin^2(2\phi) + (\cos^2(2\phi) + \cot^2(\delta/2)) (\cosh^2(\gamma) - \cos^2(\alpha))} \tag{2.64}$$

$$\chi(\phi) = 2 \frac{\sin(2\phi) (\cosh(\gamma) \sin(\alpha) \cos(2\phi) - \sinh(\gamma) \cos(\alpha) \cot(\delta/2))}{\sin^2(2\phi) + (\cos^2(2\phi) + \cot^2(\delta/2)) (\cosh^2(\gamma) - \cos^2(\alpha))} \tag{2.65}$$

$$\sigma(\phi) = 2 \frac{\sin(2\phi) (\cosh(\gamma) \sin(\alpha) \cot(\delta/2) + \sinh(\gamma) \cos(\alpha) \cos(2\phi))}{\sin^2(2\phi) + (\cos^2(2\phi) + \cot^2(\delta/2)) (\cosh^2(\gamma) - \cos^2(\alpha))}. \quad (2.66)$$

### 2.2.2.2 The effect on polarisation of a quarter wave-plate

The quarter-wave plate used in the setup was designed for  $\lambda_0 = 633\text{nm}$ , however the wavelength of the laser used is  $\lambda = 660\text{nm}$ . This means that the phase shift acquired by the beam once passing through the QWP will not be  $\frac{\pi}{2}$  but will be given by the corrected retardance

$$\delta_{QWP} = \frac{\lambda_0}{\lambda} \frac{\pi}{2}. \quad (2.67)$$

### 2.2.2.3 The effect on the polarisation of a liquid crystal variable retardance device

The liquid crystal variable retarder in contrast to the quarter-wave plate has a variable retardance  $\delta_{LCVR}$  and itself is not rotated. When an electric potential is applied across the liquid crystal device, the molecules align to the field accordingly, changing the level of birefringence along the extraordinary axis [23]. In our setup, the fast axis is oriented at  $\phi = 45^\circ$  to the incoming s-polarised (along y-axis) laser beam, which simplifies equation (2.57) giving

$$\mathbf{E}^{LCVR} = E_0 \begin{pmatrix} \sin(\delta_{LCVR}/2) \\ i \cos(\delta_{LCVR}/2) \end{pmatrix} e^{ikz}. \quad (2.68)$$

The retardance of the LCVR can be determined as a function of voltage, by measuring relative intensities along x-axis and y-axis

$$\frac{I_x}{I_y} = \tan^2(\delta_{LCVR}/2). \quad (2.69)$$

The data for experimental determination of the retardance of the LCVR can be seen in figure 2.2.



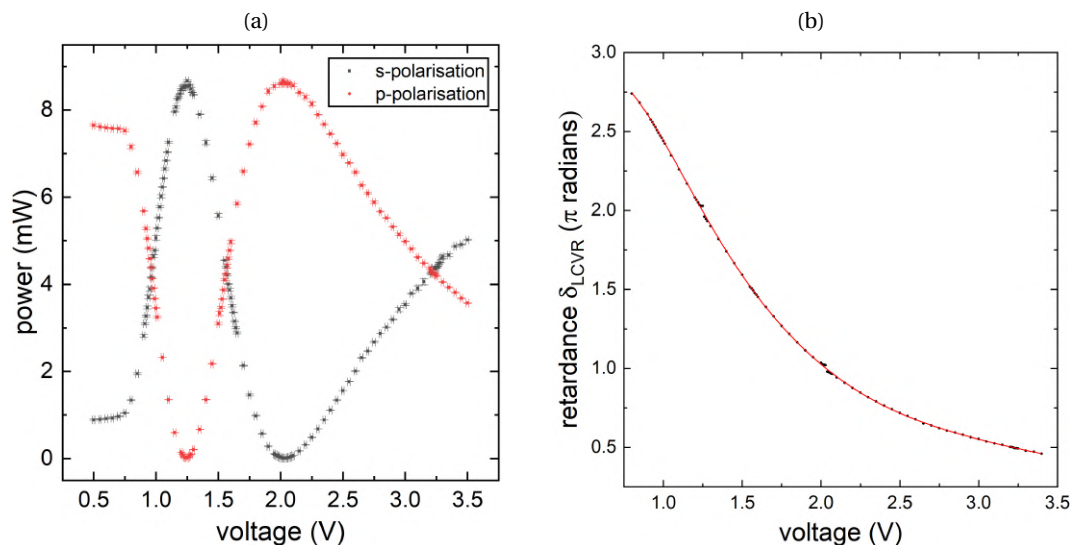


FIGURE 2.2. **(a)** Experimental calibration data for LCVR. **(b)** Corresponding retardance  $\delta_{LCVR}$  relation against input voltage, found using equation (2.69). Red line is a polynomial fit.

### 2.2.3 Characteristics of the evanescent field

The intensity of the field is proportional to the square of the electric field; away from the surface it can be described as

$$I(z) \propto |\mathbf{E}_{fx}|^2 \propto I_0 e^{-x/2\kappa} \quad (2.70)$$

where  $I_0$  is the intensity at the surface, whilst the decay length  $l_d$  of the evanescent wave is given by [24]

$$l_d = \frac{1}{2\kappa} = \frac{\lambda}{4\pi \sqrt{n_i^2 \sin^2(\alpha) - n_f^2}} \quad (2.71)$$

and is dependent on the angle of incidence  $\alpha$  and the refractive indices. In practice, for light incident close to critical angle in the visible spectrum going from glass to air, the decay length is around 300nm, however measurements are rarely performed at the critical angle, meaning that the decay length quickly drops below 150nm (see figure 2.3a).

Comparing equations (2.38) and (2.42), in each dimension, reveals two unusual features of the evanescent field.

Firstly, the intensity of the field created, depending on the angle of incidence, can be greater than that of the incident beam [25–27]. If we take the intensity  $I_f^j = |E_f^j|^2$  at the interface  $z = 0$  where

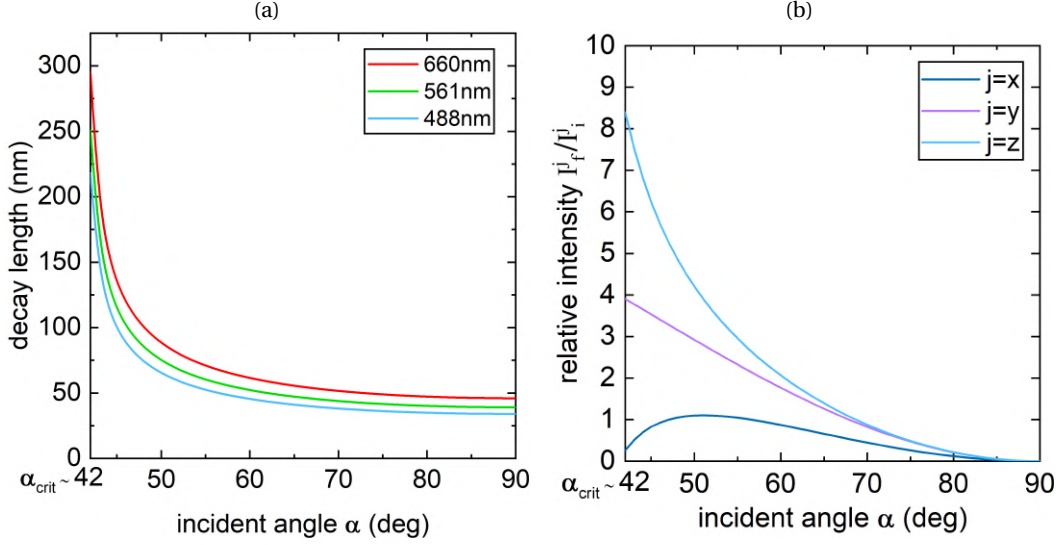


FIGURE 2.3. Evanescent field properties **(a)** decay length vs angle of incidence **(b)** ratio of intensities of incident  $I_i^j$  and  $I_f^j$  transmitted fields at  $x=0$  for all the dimensions ( $j = x, y, z$ ).

$j = \{x, y, z\}$  and compare it with the intensity of the incident wave also at the interface  $z = 0$  we can observe the following relation in figure 2.3.

Secondly, figure 2.3 and equations (2.42) and (2.43) clearly show the presence of polarisation in the direction of the propagation of the evanescent wave. The evanescent field, generated from the p-polarised component of incident light, acquires elliptical polarisation in  $xz$ -plane upon total internal reflection. This phenomenon is called spin locking as the direction of the rotation of the field (its handedness) in  $xz$ -plane is solely dependent on the direction of the propagation of the wave and not on its initial polarisation [28–31].

## 2.3 Optical Forces in the Evanescent Field

Derivation of the analytical model in section 2.1.3 shows the decomposition of the forces acting on a small particle in an arbitrary monochromatic field, giving equations (2.30) through to (2.34). When solving those for homogeneous plane wave, the energy density of the wave is

$$W = \frac{g}{2\omega} |A|^2 n^2 \omega = \text{const.} \quad (2.72)$$

and therefore

$$\begin{aligned}
 F^g &= 0 \\
 F^o &= \frac{\omega}{g} \left( \mu \text{Im}(\alpha_e) + \varepsilon \text{Im}(\alpha_m) - \frac{2k^3}{3} \text{Re}(\alpha_e^* \alpha_m) \right) \frac{W}{n^2 \omega} k \hat{\mathbf{z}} \\
 F^s &= 0 \\
 F^i &= 0
 \end{aligned} \tag{2.73}$$

the only force experienced by the particle is the orbital contribution and is oriented along the direction of the propagation of the wave.

However in the case of the evanescent wave, the energy density is

$$W = \frac{g}{2\omega} n^2 \omega |A|^2 e^{-i2\kappa x} \tag{2.74}$$

where their electric and magnetic contributions can be written as

$$\begin{aligned}
 W_e &= \frac{1}{2} \left( 1 + \tau \frac{\kappa^2}{k_z^2} \right) W \\
 W_m &= \frac{1}{2} \left( 1 - \tau \frac{\kappa^2}{k_z^2} \right) W
 \end{aligned} \tag{2.75}$$

and so the force acting on the particle in the evanescent field are [9, 14, 21, 32]

$$\begin{aligned}
 F^g &= -2\kappa \left( \frac{\text{Re}(\alpha_e)}{4g\varepsilon} \left( 1 + \tau \frac{\kappa^2}{k_z^2} \right) + \frac{\text{Re}(\alpha_m)}{4g\mu} \left( 1 - \tau \frac{\kappa^2}{k_z^2} \right) \right) W \hat{\mathbf{x}} \\
 F^o &= \frac{\omega}{g} \left( \frac{W_e}{n^2 \omega} \left( \mu \text{Im}(\alpha_e) - \frac{k^3}{3} \text{Re}(\alpha_e^* \alpha_m) \right) + \frac{W_m}{n^2 \omega} \left( \varepsilon \text{Im}(\alpha_m) - \frac{k^3}{3} \text{Re}(\alpha_e^* \alpha_m) \right) \right) k_z \hat{\mathbf{z}} \\
 F^s &= \frac{\omega}{3g} k^3 \text{Re}(\alpha_e^* \alpha_m) \frac{W}{n^2 \omega} \left( -\frac{\kappa^2}{k_z} \hat{\mathbf{z}} + \sigma \frac{k\kappa}{k_z} \hat{\mathbf{y}} \right) \\
 F^i &= \frac{\omega}{3g} k^3 \text{Im}(\alpha_e^* \alpha_m) \frac{W}{n^2 \omega} \left( -\tau \frac{k^2 \kappa}{k_z^2} \hat{\mathbf{x}} + \chi \frac{k\kappa}{k_z} \hat{\mathbf{y}} \right).
 \end{aligned} \tag{2.76}$$

Most importantly, two of the total force contribution have a transverse, spin-dependent component. The contribution from the spin momentum and the imaginary Poynting vector can therefore be thought of as manifestations of the Belinfante's spin momentum contribution to the electromagnetic stress-energy tensor [21, 32, 33]. It is worth mentioning here another spin-dependent force acting on a polarisable particle. It has been shown recently that a small polarisable particle near a surface will experience a recoil force acting in the opposite direction to the direction of scattering of the EM field, which depends on the polarisation of the wave [34–37].

## 2.4 Bibliography

- [1] F. Belinfante, “On the current and the density of the electric charge, the energy, the linear momentum and the angular momentum of arbitrary fields,” *Physica*, vol. 7, pp. 449–474, May 1940.
- [2] R. P. Cameron, S. M. Barnett, and A. M. Yao, “Optical helicity, optical spin and related quantities in electromagnetic theory,” *New Journal of Physics*, vol. 14, p. 053050, May 2012.
- [3] D. Gao, W. Ding, M. Nieto-Vesperinas, X. Ding, M. Rahman, T. Zhang, C. Lim, and C.-W. Qiu, “Optical manipulation from the microscale to the nanoscale: Fundamentals, advances and prospects,” *Light: Science & Applications*, vol. 6, pp. e17039–e17039, Sept. 2017.
- [4] J. J. Kingsley-Smith, M. F. Picardi, L. Wei, A. V. Zayats, and F. J. Rodríguez-Fortuño, “Optical forces from near-field directionalities in planar structures,” *Physical Review B*, vol. 99, p. 235410, June 2019.
- [5] L. Novotny and B. Hecht, *Principles of Nano-Optics*. Cambridge University Press, 2012.
- [6] A. Canaguier-Durand, A. Cuche, C. Genet, and T. W. Ebbesen, “Force and torque on an electric dipole by spinning light fields,” *Physical Review A*, vol. 88, p. 033831, Sept. 2013.
- [7] B. T. Draine, “The discrete-dipole approximation and its application to interstellar graphite grains,” *The Astrophysical Journal*, vol. 333, p. 848, Oct. 1988.
- [8] G. Mie, “Beiträge zur Optik trüber Medien, speziell kolloidaler Metallösungen,” *Annalen der Physik*, vol. 330, no. 3, pp. 377–445, 1908.
- [9] A. Y. Bekshaev, K. Y. Bliokh, and F. Nori, “Mie scattering and optical forces from evanescent fields: A complex-angle approach,” *Optics Express*, vol. 21, p. 7082, Mar. 2013.
- [10] A. Y. Bekshaev, O. V. Angelsky, S. G. Hanson, and C. Y. Zenkova, “Scattering of inhomogeneous circularly polarized optical field and mechanical manifestation of the internal energy flows,” *Physical Review A*, vol. 86, p. 023847, Aug. 2012.

- [11] E. Almaas and I. Brevik, “Radiation forces on a micrometer-sized sphere in an evanescent field,” *Journal of the Optical Society of America B*, vol. 12, p. 2429, Dec. 1995.
- [12] A. Bekshaev and M. Soskin, “Transverse energy flows in vectorial fields of paraxial beams with singularities,” *Optics Communications*, vol. 271, pp. 332–348, Mar. 2007.
- [13] M. V. Berry, “Optical currents,” *Journal of Optics A: Pure and Applied Optics*, vol. 11, p. 094001, Sept. 2009.
- [14] A. Bekshaev, K. Y. Bliokh, and M. Soskin, “Internal flows and energy circulation in light beams,” *Journal of Optics*, vol. 13, p. 053001, May 2011.
- [15] K. Y. Bliokh, A. Y. Bekshaev, and F. Nori, “Optical Momentum, Spin, and Angular Momentum in Dispersive Media,” *Physical Review Letters*, vol. 119, Aug. 2017.
- [16] R. Gómez-Medina, M. Nieto-Vesperinas, and J. J. Sáenz, “Nonconservative electric and magnetic optical forces on submicron dielectric particles,” *Physical Review A*, vol. 83, p. 033825, Mar. 2011.
- [17] A. Y. Bekshaev, “Subwavelength particles in an inhomogeneous light field: Optical forces associated with the spin and orbital energy flows,” *Journal of Optics*, vol. 15, p. 044004, Apr. 2013.
- [18] M. Nieto-Vesperinas and J. J. Saenz, “Optical forces from an evanescent wave on a magnetodielectric small particle,” *Optics Letters*, vol. 35, p. 4078, Dec. 2010.
- [19] S. Albaladejo, M. I. Marques, M. Laroche, and J. J. Saenz, “Scattering Forces from the Curl of the Spin Angular Momentum of a Light Field,” *Physical Review Letters*, p. 4, 2009.
- [20] P. C. Clemmow, I. Antennas, and P. Society, *The Plane Wave Spectrum Representation of Electromagnetic Fields*. A Classic Reissue, IEEE, 1996.
- [21] M. Antognozzi, C. R. Bermingham, R. L. Harniman, S. Simpson, J. Senior, R. Hayward, H. Hoerber, M. R. Dennis, A. Y. Bekshaev, K. Y. Bliokh, and F. Nori, “Direct measurements of the extraordinary optical momentum and transverse spin-dependent force using a nano-cantilever,” *Nature Physics*, vol. 12, pp. 731–735, Aug. 2016.
- [22] B. Guenther, *Modern Optics*. Oxford University Press, 2015.

- [23] S. Kasap, *Optoelectronics & Photonics: Principles & Practices: International Edition*. Pearson Education Limited, 2013.
- [24] M. Oheim, A. Salomon, A. Weissman, M. Brunstein, and U. Becherer, “Calibrating Evanescent-Wave Penetration Depths for Biological TIRF Microscopy,” *Biophysical Journal*, vol. 117, pp. 795–809, Sept. 2019.
- [25] L. Józefowski, J. Fiutowski, T. Kawalec, and H.-G. Rubahn, “Direct measurement of the evanescent-wave polarization state,” *Journal of the Optical Society of America B*, vol. 24, p. 624, Mar. 2007.
- [26] D. Axelrod, “Fluorescence excitation and imaging of single molecules near dielectric-coated and bare surfaces: A theoretical study,” *Journal of Microscopy*, vol. 247, pp. 147–160, Aug. 2012.
- [27] T. Kawalec, L. Józefowski, J. Fiutowski, M. Kasprończ, and T. Dohnalik, “Spectroscopic measurements of the evanescent wave polarization state,” *Optics Communications*, vol. 274, pp. 341–346, June 2007.
- [28] M. F. Picardi, A. Manjavacas, A. V. Zayats, and F. J. Rodríguez-Fortuño, “Unidirectional evanescent-wave coupling from circularly polarized electric and magnetic dipoles: An angular spectrum approach,” *Physical Review B*, vol. 95, p. 245416, June 2017.
- [29] L. A. McCarthy, K. W. Smith, X. Lan, S. A. Hosseini Jebeli, L. Bursi, A. Alabastri, W.-S. Chang, P. Nordlander, and S. Link, “Polarized evanescent waves reveal trochoidal dichroism,” *Proceedings of the National Academy of Sciences*, vol. 117, pp. 16143–16148, July 2020.
- [30] K. Y. Bliokh, F. J. Rodríguez-Fortuño, F. Nori, and A. V. Zayats, “Spin–orbit interactions of light,” *Nature Photonics*, vol. 9, pp. 796–808, Dec. 2015.
- [31] T. Van Mechelen and Z. Jacob, “Universal spin-momentum locking of evanescent waves,” *Optica*, vol. 3, p. 118, Feb. 2016.
- [32] K. Y. Bliokh, A. Y. Bekshaev, and F. Nori, “Extraordinary momentum and spin in evanescent waves,” *Nature Communications*, vol. 5, p. 3300, May 2014.

- [33] V. Svak, O. Brzobohatý, M. Šiler, P. Ják, J. Kaňka, P. Zemánek, and S. H. Simpson, “Transverse spin forces and non-equilibrium particle dynamics in a circularly polarized vacuum optical trap,” *Nature Communications*, vol. 9, p. 5453, Dec. 2018.
- [34] F. J. Rodríguez-Fortuño, N. Engheta, A. Martínez, and A. V. Zayats, “Lateral forces on circularly polarizable particles near a surface,” *Nature Communications*, vol. 6, Dec. 2015.
- [35] F. J. Rodriguez-Fortuno, G. Marino, P. Ginzburg, D. O’Connor, A. Martinez, G. A. Wurtz, and A. V. Zayats, “Near-Field Interference for the Unidirectional Excitation of Electromagnetic Guided Modes,” *Science*, vol. 340, pp. 328–330, Apr. 2013.
- [36] J. J. Kingsley-Smith, M. F. Picardi, L. Wei, A. V. Zayats, and F. J. Rodríguez-Fortuño, “Optical forces from near-field directionalities in planar structures,” *Physical Review B*, vol. 99, p. 235410, June 2019.
- [37] L. Wei, M. F. Picardi, J. J. Kingsley-Smith, A. V. Zayats, and F. J. Rodríguez-Fortuño, “Directional scattering from particles under evanescent wave illumination: The role of reactive power,” *Optics Letters*, vol. 43, p. 3393, July 2018.

## LATERAL MOLECULAR FORCE MICROSCOPE

Presented in this chapter is a design of a new generation of Lateral Molecular Force Microscope [1], which is a SPM with a vertically oriented mechanical sensor. Creating new high precision positioning stages was crucial in achieving a versatile, stable and sensitive microscope. Part of the content of this chapter is included in the manuscript submitted to the journal *Sensors - Special Issue: Cantilever-Based Sensors* [2].

### 3.1 Near-field Scanning Optical Microscopy

Near-field Scanning Optical Microscopy (NSOM) is a part of the large SPM family and was first realised by D.W. Pohl et al. in 1984 when they presented an optical equivalent of a stethoscope. With that instrument they demonstrated that the diffraction limit could be overcome in the optical spectrum, if one uses a probe with a small enough aperture, located within tens of nanometers from the sample, like a stethoscope which can locate a heart if placed on the patient's chest [3]. The conceptual principles were suggested first by Synge in 1928 [4, 5] and were theoretically explored in the 1960s [6, 7]. The concept then was proven to work in the microwave regime by A. Ash and G. Nichols [8], however creating a suitable aperture probe to work for optical wavelengths remained a technological challenge until the early 80s.



NSOMs can be divided into two main categories. The first one being the aperture NSOM, mentioned above, where the probe with an aperture can either work as a source of light or as a detector. The second category is the scattering NSOM (s-NSOM, also referred to as apertureless NSOM) where a tip of the probe is approximated by a dipole scatterer and the light it scatters, is collected and measured in the far field. When illuminating the probe with the appropriate laser frequency range (frequency of molecular vibrations), s-NSOM can be used to perform surface enhanced Raman scattering (SERS) [9] or tip enhanced Raman scattering (TERS) [10]. Nano-antennas have been successfully investigated as an option to increase the signal-to-noise ratio and the resolution of NSOMs (both the aperture and apertureless), though the manufacturing of these probes is not yet straight forward [11–13].

## 3.2 Overview of the Lateral Molecular Force Microscope

The Lateral Molecular Force Microscope (LMFM) (see figure 3.1) is a type of s-NSOM utilizing Scattered Evanescent Wave (SEW) as means of detecting the position of the vertically oriented probe (see section 3.4). The special orientation of the probe not only allows for use of significantly softer mechanical sensors than that of a conventional AFM (see section 1.5), but it also opens up the possibility to investigate forces acting parallel to the sample surface. The new generation of LMFM designed and built for this project was based on the initial version suggested by Antognozzi et al. in 2008 [1] and is a significant improvement from the one used in 2016 to measure the Belinfante Spin Momentum [14]. The main motivation behind the design of the new generation of LMFM was to create an instrument with simple nano-scale control over the positioning of both the sample and the probe with remote control capabilities. Furthermore, the new system was designed to be compatible with full automation of sample and probe exchange, in part answering the global scientific issue of low levels of reproducibility in current most advanced research [15]. Microscope presented in this chapter shows how the innovative design paradigm adopted, satisfies all the previous requirements while improving sensitivity, stability and versatility when compared to the previous generation.

The most significant part of the evolution of LMFM was to establish positional control over the sample and probe along 7 degrees of freedom (DoF) using motorised actuators. This solution signifi-

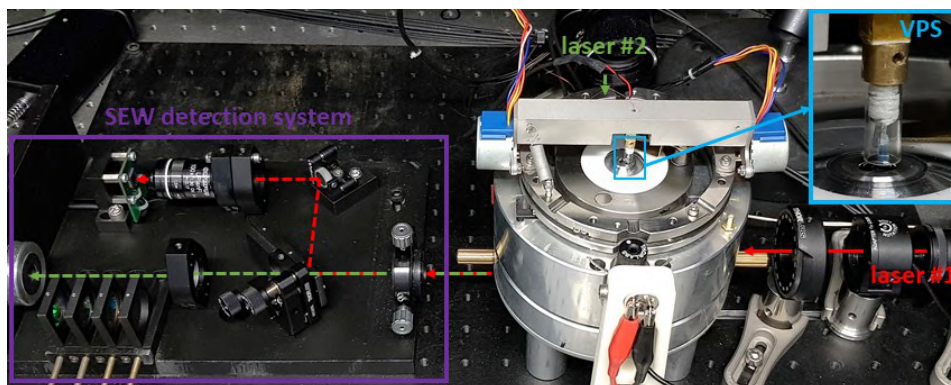


FIGURE 3.1. Photograph of the LMFM with highlighted laser paths, scattered evanescent wave detection system (described in section 3.4) and the vertical positioning system (VPS) described in section 3.6.3.

cantly improved the ability to manipulate the sample and probe while simplifying their exchange. To obtain these results, it was necessary to develop original translational stages and rotational control. Two stick-slip-based translational stages were designed to control the translational degrees of freedom in the horizontal plane for both the sample and the probe (see section 3.6.1). The vertical positioning of the sample is controlled using motorised screws to ensure the sample lies in the focal plane of the objective lens. A novel stick-slip vertical positioning system was introduced to control the probe-sample distance (see section 3.6.3). Microscope SPM-head required a radical new design to allow control of the tilt of the cantilever ( $7^{th}$  DoF), ensuring that each measurement is performed with the probe at the desired, vertical orientation.

### 3.2.1 Microscope environment overview

The microscope has been designed to perform measurements in both air and liquid environments allowing to investigate living biological samples as well as optical fields in different refractive indices. All measurements presented in this thesis were performed at room temperature and in ambient conditions, unless otherwise specified.

The microscope described in this chapter contains a thermally insulated ceramic sample stage, which combined with a thermoelectric Peltier component opens up the possibility to investigate the optical and mechanical properties of samples in a range of temperatures (approximately  $5^{\circ}\text{C}$  to  $42^{\circ}\text{C}$  which corresponds to a key temperature range for microbiology; between refrigerator temperatures

and that of human body with very high fever).

The microscope body, the laser optics and the SEW detection system are all mounted on a thick aluminium plate which enhances the overall system rigidity. The whole setup is placed on a Newport optical table fitted with passive pneumatic legs in a standard windowless laboratory. Due to the extreme force sensitivity of the instrument, the presence of the microscope operator in the laboratory can easily introduce detectable air currents movement and sound waves. To counteract this problem, some of the measurements were performed with the microscope enclosed in a metal enclosure. Thanks to the new microscope design, it was also possible to perform some of the most sensitive measurements remotely, allowing the environment in the room to equilibrate without anyone present. Further improvements in the drive-by-wire technology employed in the current system could enable even more complex measurements to be performed remotely. These changes would include replacing the current manual switches with electronic relays or mounting optical polarisers on motorized mounts.

### 3.2.2 Modes of operation

The versatility of the system translates into a range of different applications with force sensing being the main focus in the present work. Forces applied to the cantilever can be measured using two different modes of operation which include the static force and deflection measurements and the dynamic force measurements. Furthermore, the LMFM can be used for scanning probe imaging, as well as probe-less applications like the Sub-Cellular Fluctuation Imaging (SCFI) and fluorescence microscopy.

**Static mode** is the mode of operation predominantly used throughout this thesis and is described in more detail in chapter 4, and relates the deflection of the probe and its spring constant  $k$  to find the force using Hooke's Law (eq.1.1). This mode of operation can also be used to measure forces in a variety of biological samples, from molecular motors to cell membrane proteins. In the case of the motor protein kinesin, LMFM can measure the force generated by individual steps as the kinesin processes along a microtubule [16]. In other research the LMFM was used to evaluate the conformational changes and the binding mechanism of the protein adhesin found on the outer membrane of *Moraxella* bacterial cells [17].

**Dynamic mode** force sensing differs from the static mode in that it relates the amplitude and the phase of driven probe oscillations with the force applied. Similarly to the non-contact mode AFM, the motion of the probe is described using simple harmonic oscillator equation with an external force  $F$  acting upon it [18, 19]

$$m \frac{d^2 x}{dt^2} + b \frac{dx}{dt} + kx = F \cos(\omega t) \quad (3.1)$$

where  $\omega$  is the angular frequency,  $m$  is the mass and  $b$  is the damping coefficient, which can be related to the resonant frequency  $\omega_0$  and the quality factor  $Q$  as  $b = m\omega_0/Q$ . Solving this second order differential equation allows us to arrive at expressions relating the amplitude  $A_d$  of oscillations and the phase  $\varphi_d$  to the applied force as

$$A_d = \frac{F}{m \left( (\omega_0^2 - \omega^2)^2 + (\omega\omega_0/Q)^2 \right)} \quad (3.2)$$

$$\varphi_d = \tan^{-1} \left( \frac{m\omega\omega_0}{(k - \omega^2 m)Q} \right). \quad (3.3)$$

The LMFM working in dynamic mode has been previously used to observe viscoelastic properties of a confined thin film of water, where individual layers of  $H_2O$  molecules could be clearly identified [20].

As already mentioned, the LMFM can also be used to perform **scanning probe imaging** similar to that of other SPMs [21]. This method is based on the same principles behind the dynamic force measurements that detect force gradients while scanning the sample surface. Differently from conventional AFM imaging, in LMFM, the total scattering signal from the probe is used to ensure a constant tip-sample separation. This mode uses slightly stiffer cantilevers from the ones used in static-force sensing LMFM, to limit the area swept by the driven probe both due to the excitation frequency as well as thermally induced fluctuations. The technique has proven to be capable of imaging single molecules of DNA [22] and is especially suited to imaging very fragile self-assembling peptide cages [23].

With the current trend of creating techniques for correlated imaging (e.g. combination of AFM for surface topography with fluorescence microscopy to help identify receptors of interest) [21], the LMFM design gives the opportunity to perform experiments combining force measurements to optical microscopy like **Total Internal Reflection Fluorescence (TIRF) imaging** [24, 25] which

involves the use of either organic fluorophores [26] or quantum dot fluorescent dyes [26]. The LMFM is in fact compatible with many other super-resolution imaging techniques such as sPAINT [27, 28] by simply modifying part of the detection system (see section 3.4).

Recently, a new imaging mode was developed. The **Sub-Cellular Fluctuations Imaging (SCFI)** which utilizes the evanescent field illumination to observe fluctuations inside bacterial cells [29] (likely to be also applicable to investigations on eucariotic cells). The technique is based on the recent discovery that bacterial cells fluctuate when viable [30]. SCFI can be used to rapidly assess if an antibiotic is effective against a particular bacterial infection. SCFI could potentially help in the fight against antimicrobial resistance by enabling faster antimicrobial susceptibility tests. The SCFI method is described in further details in section 7.1.

### 3.3 Microfabricated Probes

The cantilevers predominantly used in LMFM are the commercially available rectangular NuNano  $Si_3N_4$  super low stress silicon nitride probes [31]. They are manufactured from an amorphous Super Low Stress LPCVD (low pressure chemical vapour deposition) silicon nitride wafer supplied by Si-Mat (with (1 0 0) Si wafer substrate). The cantilever shape is etched using  $CHF_3$  gas, before being released from silicon substrate using KOH wet-etching process [31].

The stiffness of such cantilever depends on its dimensions ( $l, w, t$  are the length, width and thickness respectively) and Young's modulus  $Y$  according to

$$k = \frac{Ywt^3}{4l^3} \quad (3.4)$$

These cantilevers dimensions are tuned according to the specific application. For low force sensing they are either 100nm or 50nm thick resulting in nominal force constant of  $10^{-5}N/m$  a  $10^{-6}N/m$  respectively. When measuring cantilevers' width in an electron microscope it was found that the width of the cantilevers varies between  $1.2\mu m$  and  $1.8\mu m$  which is almost double that of what the manufacturer states ( $1\mu m$ ). To address the uncertainty, the stiffness of the probe is evaluated during the measurement using thermal spectrum fitting [32] and so there is no need to rely on stiffness information supplied by the manufacturer. The torsional spring constant needs to be considered when the cantilever experiences large displacements and can be calculated using the following

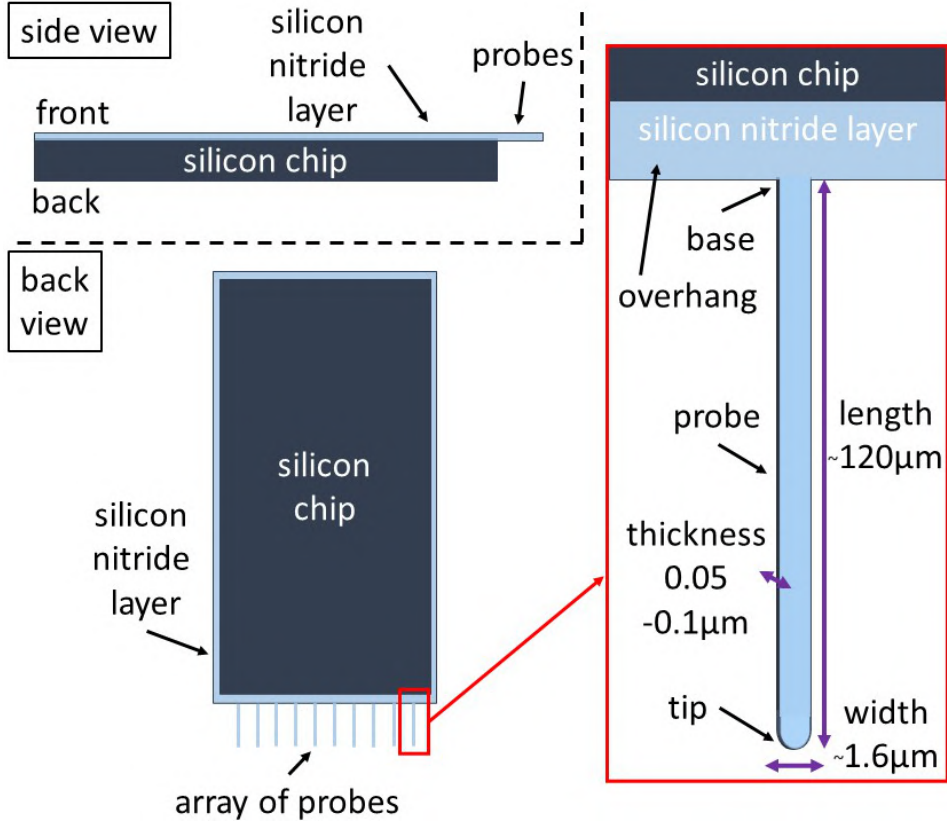


FIGURE 3.2. Cantilever array diagram (side and back view) illustrating the design of the probes used in LMFM (not to scale)

formula

$$k_{\varphi} = \frac{4Gkl^2}{3Y} \quad (3.5)$$

where  $G$  is the shear modulus. If a 5pN force is applied to the vertical edge of the 100nm thick cantilever (assuming a half width of 500nm), it would produce a torque of 2.5nN·nm and a correspondent lateral displacement of 0.02nm, comparing this effect with the displacement caused by the same force acting through the centre of the cantilever, we can conclude that the torsional effect is negligible for displacements smaller than ~ 150nm.

### 3.4 Scattered Evanescent Wave detection setup

Due to the small size of the probes [31] it would not be possible to use conventional AFM optical detection systems [21, 33, 34], so LMFM uses the Scattered Evanescent Wave (SEW) setup [1] to

detect the position of the tip of the cantilever. The SEW detection system works on the basis that objects entering the evanescent field will scatter the light, transforming it from near-field to far-field which subsequently can be measured using a detector. Such a scheme allows tracking the position of the probe tip with respect to the sample plane in three dimensions simultaneously. The SEW system works equally well in different media, in air as well as in liquid. Moreover, because the probe interacts with the evanescent field which it subsequently scatters, the size of the probe used can be as small as the wavelength of the laser.

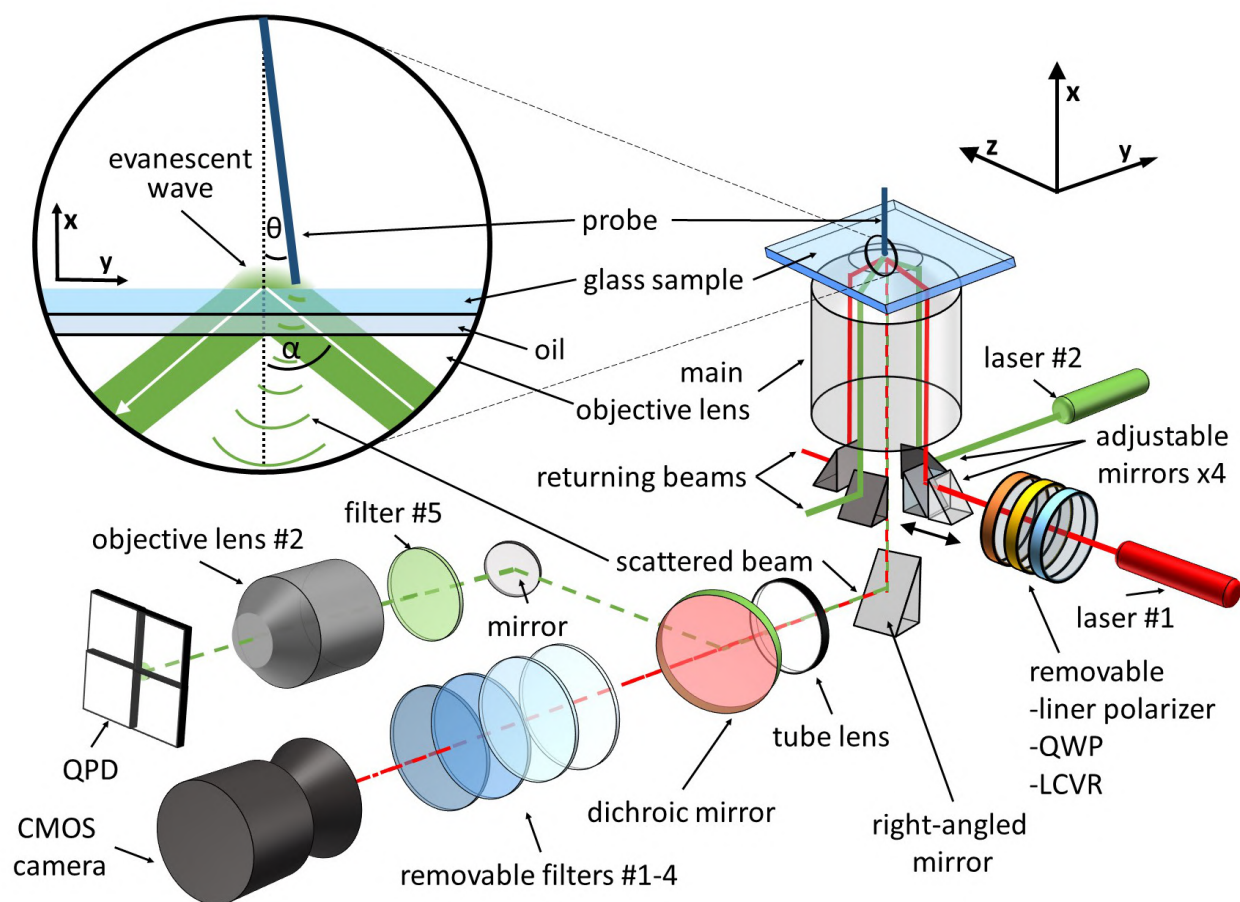


Figure 3.3: Diagram of the SEW detection system for the LMFM with a closeup illustration of the scattering cantilever tip in the evanescent field and an incidence beam coming at an angle ( $\alpha$ ) adapted from [2]

The evanescent wave in LMFM is created upon Total Internal Reflection (TIR) of a Gaussian laser beam at the glass-air (or other medium e.g. water) interface (see figure 3.3). Two perpendicular

laser beams are used to produce two concentric evanescent fields. The lasers used in the specific system are the OBIS FP 660LX (laser #1) and the Vortran Stradus VersaLase with 488nm, 561nm, 642nm modules (laser #2). Four adjustable mirrors are located underneath the main objective lens ( $\times 100$  Nikon TIRF objective  $NA = 1.49$ ). Changing their position affects how far from the axis of the objective lens the beam propagates, which in turn affects the angle of incidence  $\alpha$  of the beam onto the glass surface. The SEW system uses one laser wavelength to detect the tip position (detection laser) while the other wavelengths can be used to produce optical evanescent fields or fluorescence illumination. When the tip of the probe scatters the evanescent field, the Nikon objective lens collects the light and produces a high-magnification image on the detection plane and directed towards the detection system, on the way passing through a tube lens. Before reaching the detector the scattered light goes through a dichroic mirror which separates the detection laser wavelength from the other wavelengths (laser #2 and laser #1 in figure 3.3 respectively). The scattered light from the detection laser then goes towards the Quadrant Photodiode Detector (QPD) through a second objective lens (Olympus Plan Fluorite Oil Immersion Objective  $NA = 1.30$ ). The other wavelengths scattered by the tip are directed towards a sCMOS camera. This part of the optical path can be modified to work alongside a TIRF microscopy[24, 25] or sPAINT[27, 28, 35].

### 3.4.1 Measuring the depth of the evanescent wave

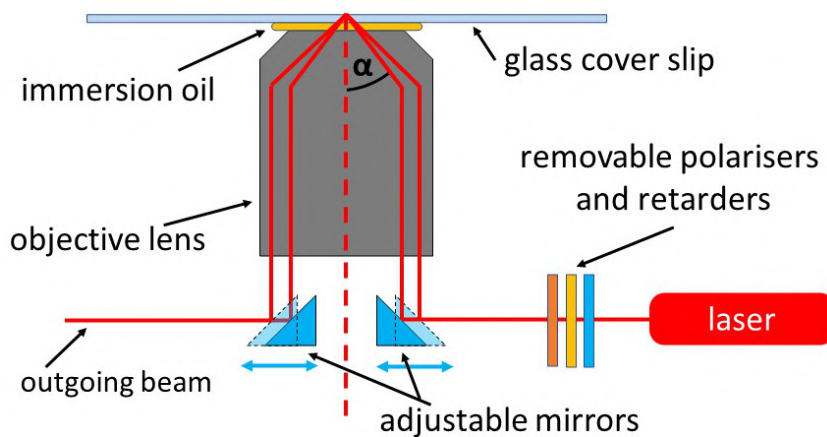


FIGURE 3.4. Diagram illustrating how the incident angle ( $\alpha$ ) is adjusted by changing the position of the mirrors underneath the objective lens.

As mentioned in the previous section, the adjustable mirrors underneath the objective lens



allow to shift the path of the laser beam within the objective lens, allowing the user to control the incident angle ( $\alpha$ ) (see figure 3.4). This is especially important when working with samples of different refractive indices as the critical angle can change significantly (e.g  $42^\circ$  for air ( $n_f = 1$ ) and  $62^\circ$  for water ( $n_f = 1.33$ ) when creating a glass-air interface (refractive index for borosilicate glass is  $n_i = 1.518$ ). Two methods can be used to determine the decay length of the evanescent wave  $l_d$  and the related incident angle ( $\alpha$ ) of the laser (see equation (2.71)) which is crucial to characterise the field.

The first method utilises a glass prism placed above and parallel to the Nikon objective lens (see figure 3.5) with the index matching oil (Olympus immersion oil Type-F) filling the gap in between allowing the incident beam to travel without changing the angle. The angle of the outgoing beam  $\beta$  can be measured and subsequently related to the incident angle using Snell's Law and geometrical relations giving:

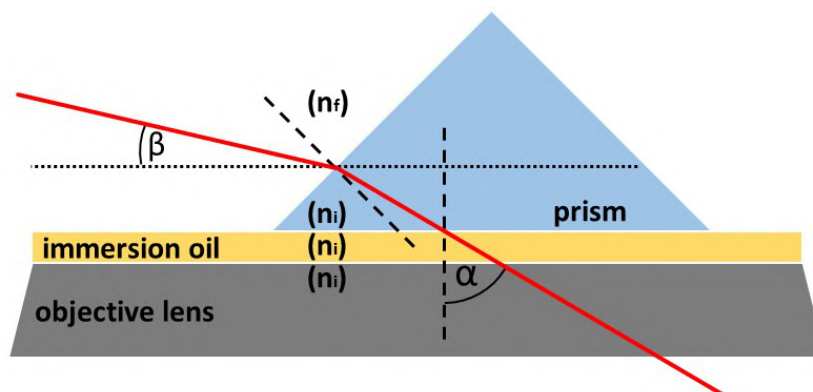


FIGURE 3.5. Diagram illustrating how to use a prism to evaluate the angle of beam incidence ( $\alpha$ ) through measuring refraction angle ( $\beta$ ).

$$\beta = 45^\circ - \arcsin\left(\frac{n_i}{n_f} \sin(\alpha - 45^\circ)\right). \quad (3.6)$$

Second method uses the probe itself. Knowing that the intensity of the evanescent field decays exponentially away from the surface (see equation (2.70)); it is possible to fit the measured scattered intensity (sum signal) of the scattered light coming from the vertical motion of the probe to find the decay length of the field (see figure 3.6).

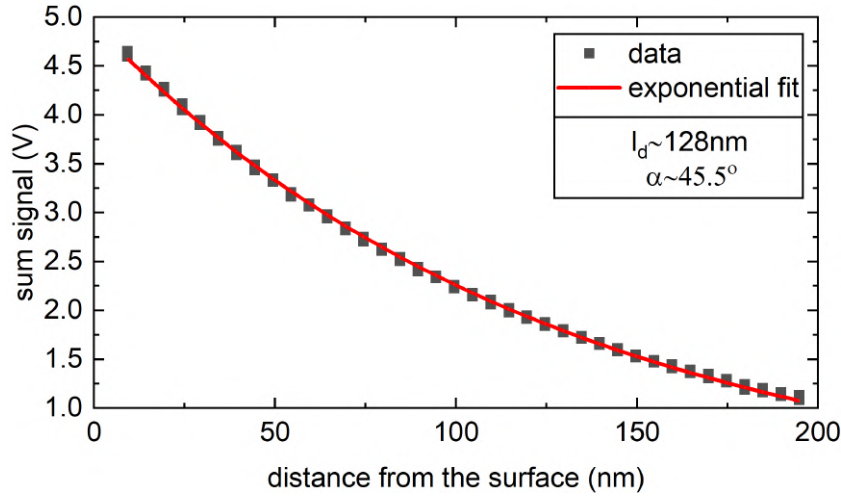


FIGURE 3.6. An example of measurement of the incidence angle using the probe method. The sum signal recorded by the detector changes exponentially as the probe is approaching the sample. The characteristic decay length of the exponential fit is the decay length of the field itself. The incidence angle can then be evaluated.

### 3.4.2 Detection of Scattered Evanescent Wave

As described in figure 3.3, the object plane can be imaged by the sCMOS camera and/or the QPD. The collected light from the objective lens is split into two paths according to the frequency by the dichroic mirror (see figure 3.3).

#### 3.4.2.1 Detection via the CMOS camera

Before reaching the CMOS camera, the scattered light goes through a selection of notch filters which are used for fluorescence microscopy. A calibration graticule with lines  $10\mu\text{m}$  apart, was used to find the optical magnification of the microscope. The number of pixels on the CMOS camera between the graticule lines was counted and the pixel size was evaluated to be  $26.5\text{nm} \pm 0.1\text{nm}$  and  $26.5\text{nm} \pm 0.2\text{nm}$  for Z and Y directions respectively. Considering that the actual pixel size is  $6.5\mu\text{m} \times 6.5\mu\text{m}$ , the optical magnification is approximately  $\times 250$ .

#### 3.4.2.2 Detection via the Quadrant Photodiode Detector (QPD)

Along the path of the detection laser, the scattered light is directed through an additional band pass filter to ensure the light reaching the detector is from the intended source, as any residual light would

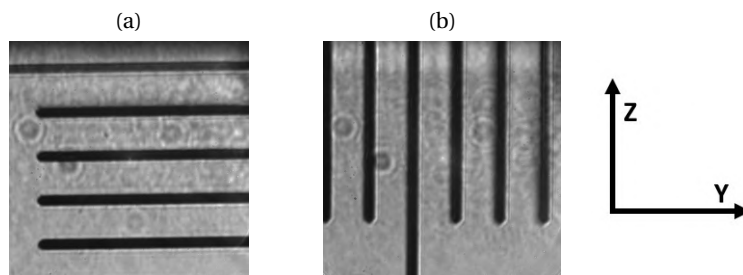


FIGURE 3.7. Images of the calibration graticule used for determining the pixel size of  $26.5\text{nm} \pm 0.1\text{nm}$  and  $26.5\text{nm} \pm 0.2\text{nm}$  in (a) Z and (b) Y directions respectively.

impact the measurements. The light then travels through a second objective lens (magnification  $\times 100$ ) before being recorded by the QPD.

The QPD measures the intensity of light incident on each of the four sectors (see figure (3.8)) and outputs proportional voltage. The overall signal intensity (or sum signal) is evaluated from the sum of all the sector's output voltages. The differential voltage corresponding to the position in z-axis and y-axis can be found by subtracting the signal from the 2 halves of the detector along the desired direction. When a scattering object is translated along a particular direction in the sample plane,

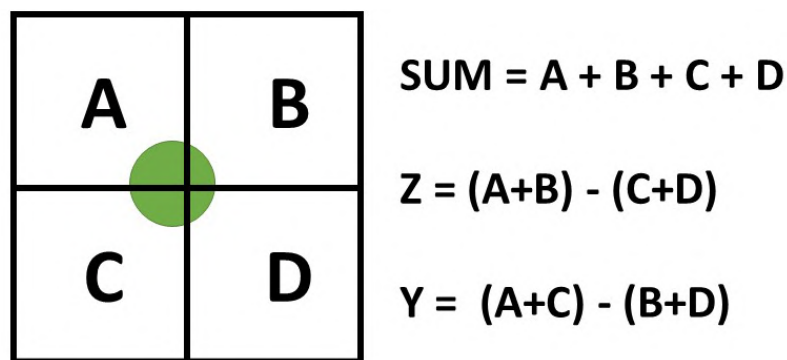


FIGURE 3.8. Principles of operations of a QPD

the corresponding image point will traverse the detector plane along the corresponding direction. The voltage recorded by the QPD will depend on the size and shape of the scatterer as well as the intensity of the field with which it is interacting. Once the object has moved all the way to one half of the detector, the differential signal becomes constant and there is no longer any information on the position of that object in that direction. Therefore, for measuring the position, the detector is only sensitive when the scattered light is focused in the centre. Furthermore, if the displacement is

small compared to the size of the object, the change in the differential signal is linear with the change in displacement. It is important to remember that the size of the linear region is dependent on the scattering object itself.

### 3.4.2.3 QPD displacement calibration method

As the relation between the differential voltage measured by the detector and the displacement of the probe depends on the shape of the probe, a calibration constant for each probe is required for the detector signal to be converted into probe displacement. After positioning the probe in the centre of the detector, the probe is moved in each of the orthogonal directions (i.e.  $y$  and  $z$ ), within the linear region shown in figure 3.9. A trapezoidal function as seen in figure 3.9a is preferred to a square triangular functions. The height of the trapezium is used to evaluate the differential voltage  $\Delta V$  (see figure 3.9b) with respect to the known displacement  $\Delta d$  allowing to evaluate the specific calibration constant  $c_{calib}$  for the experiment using equation (3.7). The two sloped sides (gray data in figure 3.9b) allow to double-check that the probe is indeed located in the linear region ensuring a normal distribution of the residuals to the linear fit of the slope (see figure 3.10).

$$c_{calib} = \frac{\Delta d}{\Delta V} \quad (3.7)$$

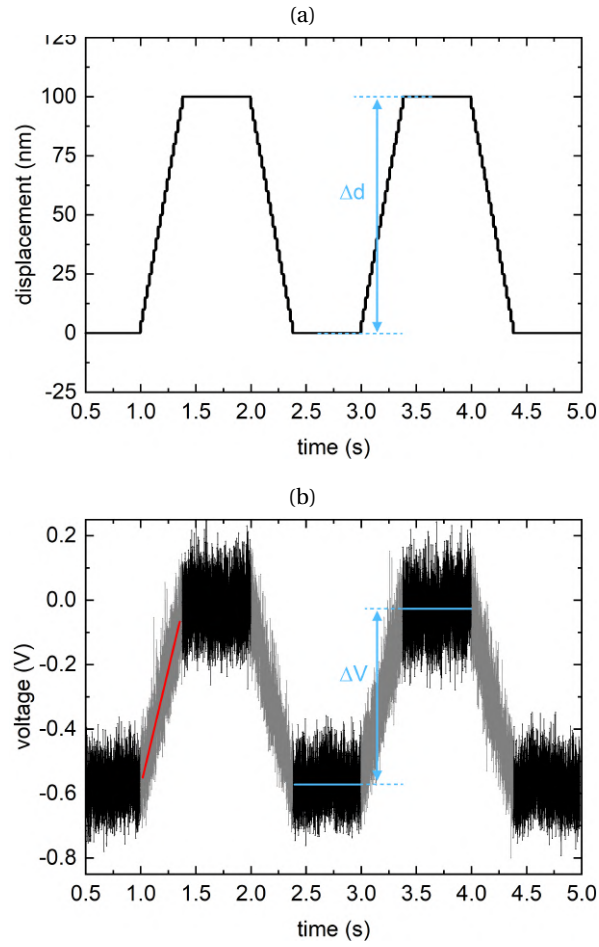


FIGURE 3.9. Calibration of the QPD signal for displacement measurements. Displayed are the time trace of **(a)** the applied trapezoidal displacement, and **(b)** the corresponding signal measured in the direction of motion. The ratio between the height of the trapezium in **(a)** and **(b)** is used to calculate the calibration constant. The red line in **(b)** is a linear fit to the data corresponding to the slope of the trapezium.

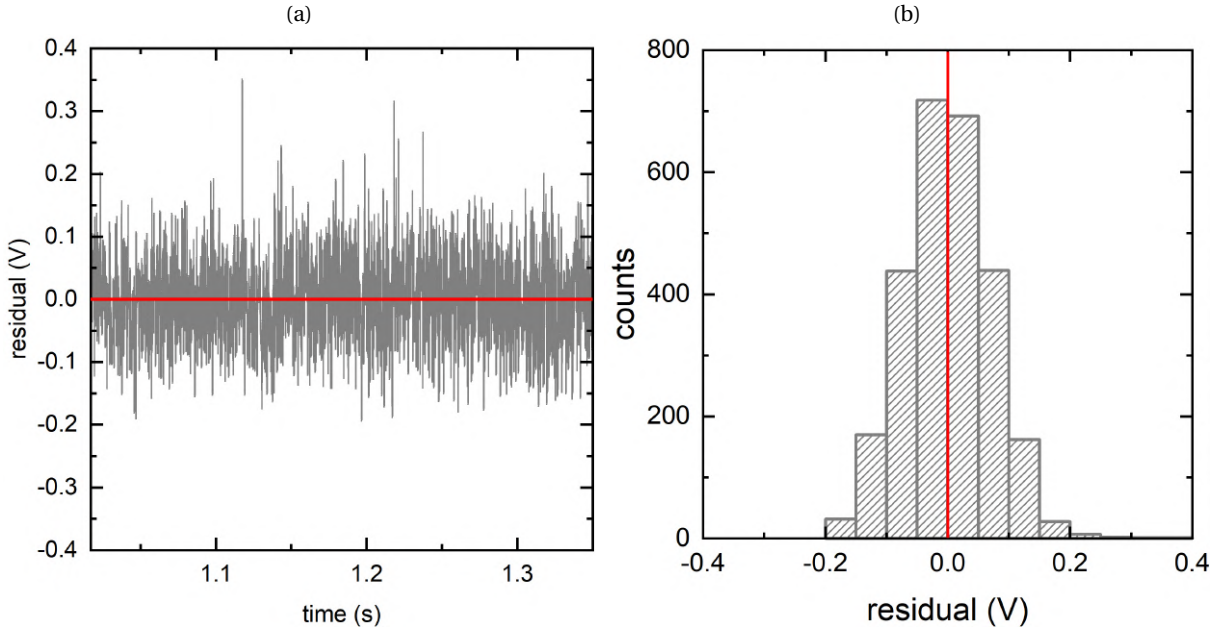


FIGURE 3.10. Residual analysis of the fitting function in figure 3.9 confirming the measurements are performed in the linear region of the detector. **(a)** Time trace of the residuals to the linear fit presented in figure 3.9. **(b)** Corresponding histogram of the data presented in **(a)** showing the normal distribution of residuals and confirming the linear region of the detector.

### 3.5 Microscope Electronics and Software

The core functionality of the controller electronics is provided by a multifunction Fully Programmable Gate Array (FPGA) by National Instruments (NI USB-7856R Multifunction RIO). The real-time software running on the FPGA and on the PC is written in LabVIEW 2018, the offline data analysis software is a combination of LabVIEW and Python code.

The Y,Z and SUM signal from the QPD (Hamamatsu S5990-01,  $4 \times 4$  mm) go through a preamplifier with adjustable gains and an anti-aliasing low pass filter and is then processed by the FPGA card. When working in the dynamic mode, the positional signal from the probe can be analysed by a digital lock-in amplifier (Signal Recovery 7265 DSP), which outputs the amplitude of oscillation and relative phase of the signal at the selected frequency. The lock-in amplifier in combination with an acoustic actuator is also used to measure the vertical orientation of the probe (see sections 3.6.4 and 3.6.6). Optical force measurements are performed by modulating the driving laser using a square wave

provided by an external function generator (Philips PM5192), see section 4.1.1. The sample and probe translation stages are controlled via the FPGA card after an amplification stage necessary to drive the stick-slips piezoelectric actuators. The images from the sCMOS camera (Hamamatsu Orca Flash 4.0) are saved directly on the PC using LabVIEW code. The stepper motors adjusting the tilt are controlled using an Arduino Uno micro-controller .

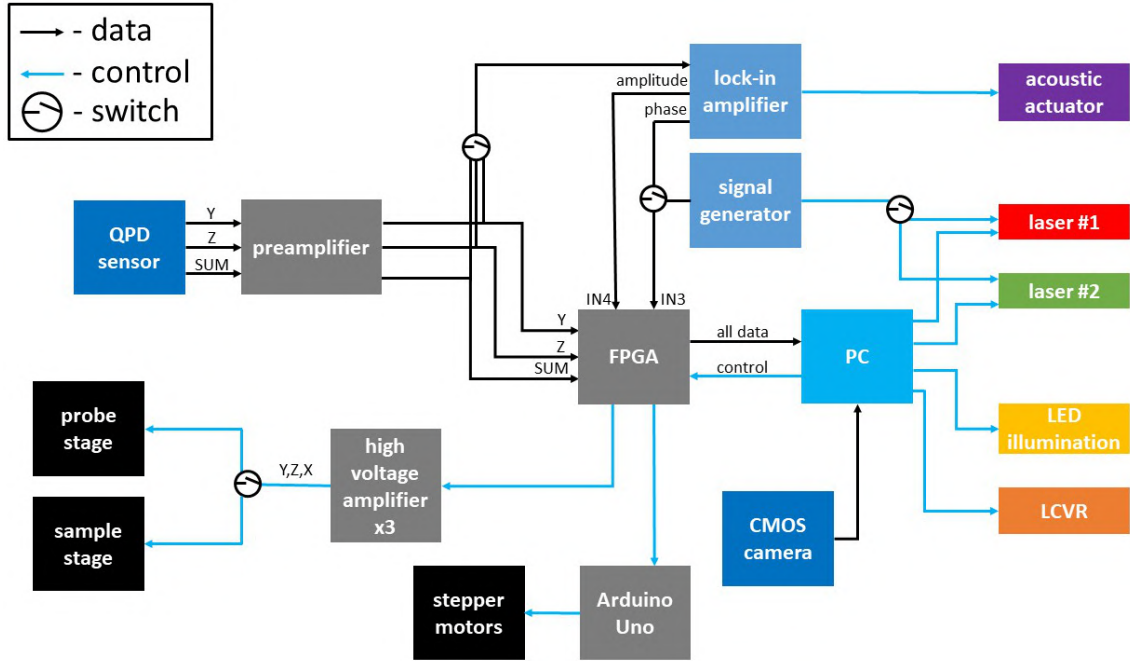


FIGURE 3.11. Schematic diagram of the electronics in LMFM

### 3.6 Sample and Probe Positioning

Although current commercial SPMs have become easier to use, they still suffer from a relatively steep learning curve. As a result, challenging experiments could become significantly simpler if many (if not all) SPM operations could be automated. For example, the possibility of exchanging tip and sample automatically is presently only available in large AFMs designed for microfabrication facilities (manufactured by Park Systems). At the same time, the motorised control of tip and sample can compromise stability and resolution and it is often avoided in high-end instruments. The new generation of LMFM contains an innovative design based on stick-slip piezo-drive that can elegantly

solve most of these problems and could lead to a fully autonomous system. As mentioned before, in this work the focus is on controlling 4 DoF of the probe and 3 DoF of the sample whilst the linear stages are compatible with tip and sample automatic exchange.

Ever since the invention of the first dynamic piezoelectric translation stage by D. W. Pohl in 1986 [36], the stick-slip design have become one of the most commonly used technology in SPMs for remote operations [37–39]. While remote controlling can be the initial step towards autonomous operations, several key issues have to be addressed to ensure stability and resolution. The translation and rotational stages described in the following sections played a fundamental role in enabling the unique measurements described in the later chapters of this thesis.

### 3.6.1 Horizontal Translation Stages

The Horizontal Translation Stages (HTS) designed and implemented for the new generation of LMFM are a type of piezo-driven stick-slip stages. The 2-tiered design has been inspired by the work done by Drevniok et al. [40], though it differs in a couple of significant aspects. As with all the modern piezo-based stick-slip stages, this system operates in 2 modes. The coarse positioning, stick-slip mode for long-range (millimetre-scale) positioning, as well as the smooth extension for fine positioning purposes (nanometer scale).

As can be seen in figure 3.12, the complete translation system consists of two concentric stages (one for the probe and one for the sample). Each HTS comprises of two stacked plates, sitting on top of a set of 3 piezo motors, which are located in the body of the microscope. Using the principles of 3-point kinematic mounting, the axial motion of the piezo actuators is transferred to the plates through a set of small spheres, cylinders and sapphire discs. Two pairs of parallel cylinders sitting on top of 2 spheres respectively, constrains the above plate to move along one axis only. With the top plate also having the same configuration (but rotated at  $90^\circ$ ), it is possible to achieve orthogonal movement of the 2 stacked plates. The stick-slip waveform is used for coarse, long-range positioning (millimetre-scale), whilst smooth extension (e.g. sinusoidal or triangular) is used for fine positioning and scanning purposes. The 2 stages are arranged concentrically with the inner stage holding the sample and the outer stage supporting the bridge on which the probe is mounted.

To create the stick-slip motion, each of the 3 piezo motors mounted in the base of the microscope



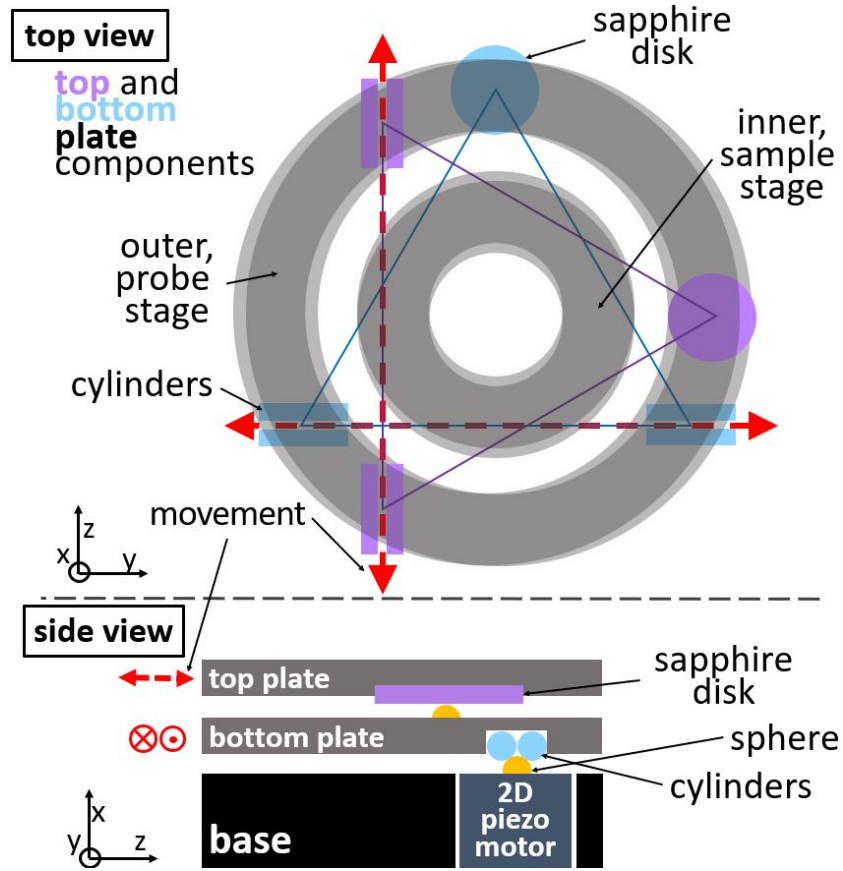


FIGURE 3.12. Schematic drawings (top and side view) of the nested probe (outer) and sample (inner) stages which are comprised of two stacked plates each. Movement of the piezo motors which are placed in the base of the microscope is translated to the stages using the principles of 3-point kinematic mount where two pairs of cylinders in each plate constrain it to move along the desired 1 dimension. Adapted from [2].

needs to extend quickly enough, so that the acceleration of the system exceeds the static friction between the cylinders and the spheres. It is important to notice that only the plate with the cylinders oriented in the same direction of the actuated piezoelectrics will experience the translation while the plate with the cylinders in the orthogonal direction will remain stationary.

Adapting this configuration allows for independent stick-slip movement of the sample in orthogonal horizontal directions as well as smooth high-precision scanning mode. Moreover, all the active parts (piezo actuators) are placed in the base of the microscope meaning that both stages do not have any active components and are in fact passive elements of the microscope thus increasing the overall stability of the system. The maximum range of movement of HTS in the LMFM is 1cm according to

the geometry of the system (the length of the cylinders and the diameter of the sapphire disk). It is useful to notice that this design is compatible with automatic sample exchange based on a conveyor belt for semiconductor wafer dispensing. It would be in fact possible to simply lift the top sample plate up and replace it with a similar plate carrying a new sample.

### 3.6.1.1 Horizontal Translation Stages - calibration

Different piezo stacks can be used to serve as 2D piezo motors. Three sets of 2 primed linear piezo actuators (PiezoDrive SA050510) positioned in L-configuration were used in this microscope (see figure 3.13a). Recently we also tested 2D sheer piezo stacks and deemed them to be a superior option for future microscopes.

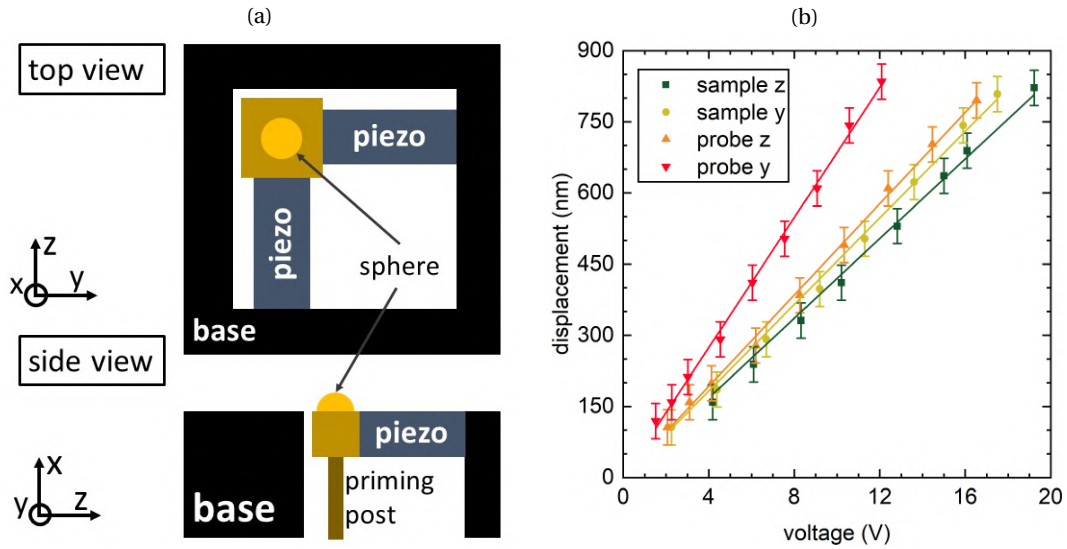


FIGURE 3.13. (a) diagram schematic (top and side view) of the 2D piezo motor used in this LMFM (b) calibration data of the linear actuators

As the 2 orthogonal piezo actuators are primed by a vertical post, the piezo extension constant might be different from the manufacturer's specifications. For that reason, a calibration of the stages movement was performed. Whilst varying the supplied voltage, a position of a small scatterer in the microscope's focal plane was recorded using the CMOS camera. A linear relation between the displacement and the applied voltage was observed (see figure 3.13b) along the z-axis and y-axis, giving similar calibration constants for both the sample and probe stages.

### 3.6.2 Vertical positioning of the sample stage

As previously mentioned, the probe and sample stages share a common base containing the piezo-electric actuators. The same base is moved up and down using motorised screws (PIAK10 from Thorlabs) to adjust the position of the sample in the vertical  $x$  direction. Precise control of the sample vertical position is essential to focus the microscope and optimise the SEW detection system. Equally important is the fact that the focusing operation does not change the tip-sample separation making it safe to adjust the focus even when the probe is a few tens of nanometres away. Bright-field microscopy and laser illumination can be used to employ common auto-focus algorithms.

### 3.6.3 Vertical Positioning System for the probe

One of the most challenging aspects of developing positioning tools for SPMs is finding a way of bringing the sample and the probe together, which often involves movement in the vertical direction; and therefore, a movement with or against the gravity. In STM, the vertical cylindrical probe is often moved towards the sample using compact, stick-slip based positioning system introduced by S.H.Pan [41]. In this system, a triangular-like probe holder is held and moved by 3 shear piezo actuators which push against the holder to prevent it from falling. This system is complex to set up and difficult to adapt for automated probe exchange.

The solution that we have devised is reminiscent of Pan's design but in a much simpler embodiment. Figure 3.14a describes the novel design of a Vertical Positioning System (VPS) which utilizes the well-known stick-slip effect to provide precise movement of a VOP. As usual, the VPS operates in 2 modes, coarse positioning and smooth scanning.

#### 3.6.3.1 Vertical Positioning System - design

The design of the VPS is very straightforward, and it consists of just 3 main elements: 1 - the moving plug, 2 - the glass tube and 3 - the piezo stack actuator. Schematic drawing of the VPS can be found in Figure 3.14a. Micro-fabricated cantilevers as well as other cylindrical probes can be mounted on the moving plug. The plug itself fits precisely into a smooth glass tube (cut-to-measure NMR glass tube with 4mm inner diameter were used) which acts as a guide rail directly connected to the piezo stack actuator (PK4FA2H3P2). The static friction between the plug and the glass tube is sufficient to

counteract the gravitational pull and keep the plug stationary. At the same time the friction force is sufficiently low to allow for the stick-slip movement on demand when the piezo actuator is engaged (with an exponential saw-tooth-like waveform). Kinetic friction then acts as a stopping force together with or against the gravity.

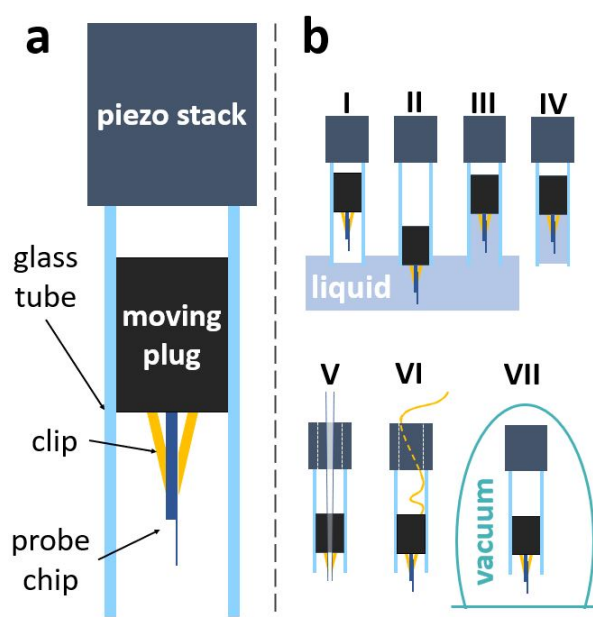


FIGURE 3.14. (a) schematic drawing of the Vertical Positioning System (VPS) (side view) (b) schematic drawings of different applications of the VPS (b(I-IV)) VPS is compatible with working in liquids and the glass tube can be subsequently used as an incubation chamber for probe (bio-)chemical functionalisation (b(V)) VPS could be adopted for NSOM techniques that use tapered waveguide probes (b(VI)) it is also possible to attach a small wire to a conductive probe which can be used for STM (b(VII)) VPS has been tested and is compatible with working in high vacuum chamber (see section 3.6.3.4). Adapted from [2].

By adjusting the amplitude of the waveform supplied to the piezo actuator, the stick-slip mode can produce nanoscale steps of the order of  $10^{-9}$  m. Larger steps can be used to travel macroscale distances of the order of  $10^{-2}$  m.

Although the design was created with LMFM in mind, the VPS here presented could be adapted to many other techniques which use vertically oriented probes. Its simplicity goes hand in hand with its potential versatility (see Figure 3.14b) allowing for it to work not only in air but also in other environments such as vacuum or liquid (see section 7.3 for example of use in liquid), which is of particular importance for bio-molecular applications. Electrical fields can be applied to conductive

probes, providing that sufficiently thin wires are used (e.g. wires used in magnetic coils). An optical fiber could be threaded through a hollow version of the plug to enable aperture NSOM microscopy.

### 3.6.3.2 Vertical Positioning System - optimisation through simulation

A simple time stepping simulation was created to investigate how the step size depends on various parameters, such as the acceleration of the piezo stack  $a(t)$ , gravity  $g$ , non-linear coefficient of friction (either static  $F_s$  or kinetic  $F_k$ ) and mass  $m$  of the plug. If the plug is initially at rest and the following relation between the piezo acceleration and the frictional force is met

$$|a(t) \pm g| > \left| \frac{F_s}{m} \right| \quad (3.8)$$

the plug slips. Once the plug is moving, it is experiencing kinetic friction which is acting in the opposite direction to the direction of motion, slowing it down and eventually stopping it.

Initially, variables like the friction coefficient, mass of the plug and the piezo acceleration were experimentally determined to optimise the system. The piezo acceleration was inferred from the voltage supplied, as it is proportional to the piezo displacement times the piezo coefficient. The plug was weighed at  $m = 0.12\text{g} \pm 0.01\text{g}$ . The static friction coefficient was determined using a custom designed piezo force gauge. The static friction of the plug in the tube was evaluated at  $F_s = 0.16\text{N} \pm 0.01\text{N}$ . Tuning the static friction of the plug is essential to adjust its mass. From the model it was found that using relatively heavier plugs in combination with larger static friction resulted in better performances.

### 3.6.3.3 VPS - Moving Plug Design

Initial plugs were lathed from polyoxymethylene plastic due to its low friction, high stiffness and high dimensional stability, to snugly fit into the NMR glass tube. However, the machining process proved challenging and time consuming. Furthermore, because the NMR glass tube themselves were not completely identical, each time the tube was exchanged, new plugs had to be made. It was clear that with such low friction coefficient, small changes in the tube's diameter will have significant consequences on the stability of the system. Surprisingly, this type of plugs performed particularly well in a liquid environment.

Following the initial observations and the results from the simulation, it was decided that a plug of higher mass and with a higher friction coefficient was needed. Two avenues were considered.

Either creating a plug inside the glass tube ensuring the appropriate fit, or creating one with a more malleable surface so that it can adjust to the dimensions of the tube.

For the first solution, the Ardalite Steele Epoxy was used as the main material. A small ball bearing was added inside to add weight to the plug. The required fit was achieved using the following procedure. Vertically positioned glass tube with a closed bottom end was filled with a solution of high concentration of detergent Decon 90. Subsequently, the detergent solution was displaced by slowly filling the tube with the epoxy and adding the sphere in the middle. The thin layer of the detergent ensured that the epoxy would not bind with the glass tube itself, whilst simultaneously ensuring a close fit.

The final solution for manufacturing the plug made use of a stainless steel M4 grab screws, wrapped in a suitable number of layers of electrical Teflon tape (RS PRO PTFE Tape 0.075mm). The relatively large mass of the screw together with the adjustable friction ensured by a malleable Teflon tape, made it possible to reach the desired mass to friction ratio. This solution has been the most successful one, due to the relative simplicity of the assembly process and the availability of the materials. Furthermore, the use of stainless steel is advantageous when working in aqueous solution.

#### **3.6.3.4 Vertical Positioning System - test in high vacuum**

The VPS has also been tested successfully in a high vacuum environment, proving its versatility and potential use in other setups, where remote positioning of a probe is a critical requirement. The VPS with a polyoxymethylene plug was inserted into the vacuum chamber of the Edwards E306 Thermal Evaporator. This evaporator allows to provide an external signal to the VPS in the chamber in order to drive the piezo actuator. The air was pumped out to reach  $2 \times 10^{-3}$  Pa. When the connected signal generator outputted a saw-tooth waveform, it induced a clear stick-slip motion of the plug that could repeatedly travel millimeters up and down. The resultant movement can be seen in figure 3.15. This experiment was of qualitative nature only.

#### **3.6.4 Tilt Adjustment**

The angular adjustment of the tilt of the probe with respect to the sample surface is of particular importance when dealing with a vertically oriented micro-cantilever. If the cantilever is not perfectly

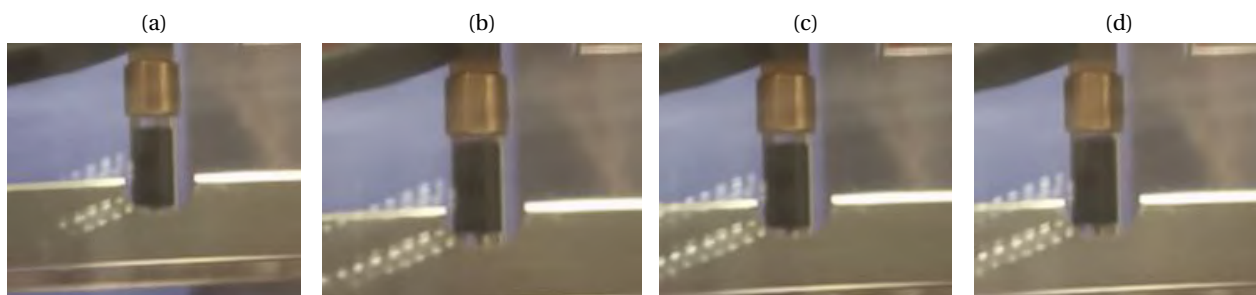


FIGURE 3.15. Chronological series of frames showing the vertical movement of a polyoxymethylene plug in the glass tube of the Vertical Positioning System in high vacuum at  $2 \times 10^{-3}$  Pa.

vertical, an attractive tip-sample interaction (e.g. van der Waals force) can produce a bending of the cantilever as the tip approaches the surface and move the tip laterally and closer to the surface. Precise adjustment of the tilt angle is necessary to remove this effect and maintain the tip on a fixed position while approaching the surface (as discussed in section 1.2).

As seen in figure3.16a, the VPS is mounted on a 'bridge' (which was enabled thanks to the compact size of VPS), above the sample, which is attached to 2 stepper motors on either side. The stepper motors are fixed to the top plate of the probe HTS, and the bridge rotates with respect to that plate. The stepper motors do 6 steps for every  $1^\circ$  of rotation. The axis of rotation of these stepper motors was designed to be aligned with the region of interest on the surface of the sample. In this way when the tip of the cantilever is close to the sample and the bridge is rotated, the tip experiences minimal lateral movement. In other words, the cantilever pivots around its tip when the bridge rotates.

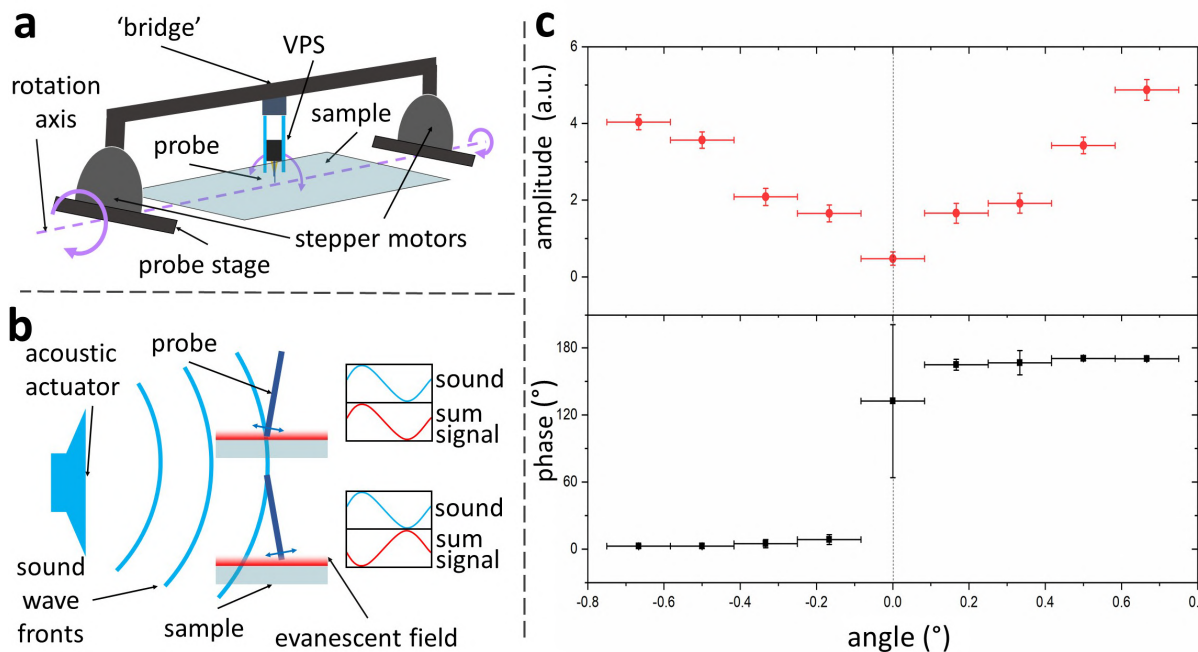


FIGURE 3.16. (a) schematic drawing of the angular adjustment design enabled by the compact size of the VPS. Two stepper motors on either side of the 'bridge' have the axis of rotation going through the sample plane. This ensures that upon the angle change, the tip of the probe remains in the region of interest (b) schematic drawing of the angle adjustment method. An acoustic actuator oscillates the cantilever whilst the sum signal is monitored at the driving frequency by the lock-in amplifier. As the tilt of the cantilever is changed, the amplitude drops when getting closer to the vertical position, whilst the phase changes as the cantilever passes through the vertical position. (c) Experimental results showing the amplitude of the sum signal and phase as a function of the tilt angle. As the vertical orientation is passed, a sharp change in phase is observed that also corresponds to the minimum amplitude of oscillations in the vertical direction. Reproduced from [2].

To adjust the probe's vertical position, an automated routine was developed. An acoustic actuator is used to oscillate the cantilever at a chosen frequency. When the cantilever is not vertical; the cantilever oscillation causes the tip to move laterally but also up and down with respect to the surface. This vertical oscillation can be observed as a change in the sum signal (see figures 3.16b and 3.16c). A lock-in amplifier is used to measure the oscillation amplitude of the sum signal as well as the relative phase. The larger the tilt angle of the cantilever, the larger the oscillations of the sum signal, which means that in order to find the vertical orientation, the amplitude measured by the lock-in amplifier



needs to be at its minimum. As illustrated in Figure 3.16b, when the probe is tilted in one direction, the sum signal will have a specific phase relation with the acoustic signal. If probe is tilted, the phase relation will be opposite. Therefore, as the tilt angle changes to minimise the amplitude, the sum signal maintains a constant phase with respect to the acoustic actuator, up until the moment when the cantilever goes through the vertical position. Subsequently, a close to 180-degree phase shift will occur which signals the vertical orientation has been reached (see Figure 3.16c).

### 3.6.5 Performance and Stability of Sample and Probe Positioning Systems

As previously stated, introducing motorised capabilities can reduce stability and/or resolution. The performance of the LMFM microscope was therefore characterised in terms of stability and accuracy of the sample and probe positioning stages.

By adjusting the voltage applied to the piezo actuators it was possible to create different step sizes allowing for long-range movement of the probe and sample (of the order of  $10^{-2}$  m), as well as to create very fine steps for nanoscale positioning (see Figure 3.17a). With respect to the VPS, the smallest steps towards the surface ('steps down') were recorded to be on average  $S_d = 2.79\text{nm} \pm 0.09\text{nm}$  with a standard deviation of  $\sigma_d = 0.52\text{nm}$ . The smallest steps away from the surface ('steps up') were found to be on average  $S_d = 2.7\text{nm} \pm 0.1\text{nm}$  with a standard deviation of  $\sigma_d = 0.7\text{nm}$ .

VPS step size was evaluated by first recording the sum signal scattered by the probe as it was moving, followed by a recording of a smooth approach of the probe towards the surface (as described in section 3.4.1) until contact point. This allowed to create a calibration curve to convert the sum signal into distance.

The smallest vertical steps produced are around an order of magnitude smaller than what is required for safe and precise approach of the tip to the sample when using SEW detection system. With the depth of the evanescent field being around 150nm the ability to produce approach steps smaller than half the decay length would be sufficient.

The stability of the microscope was evaluated by observing the drift of both the probe and the sample (see Figure 3.17b). It was found that the system experiences uniform drift velocities on the order of 1nm/min in both the horizontal plane for both the sample and the probe, as well as the vertical direction for the VPS. This is an extremely low drift value and it is comparable to the

performance of commercially available AFM systems [42].

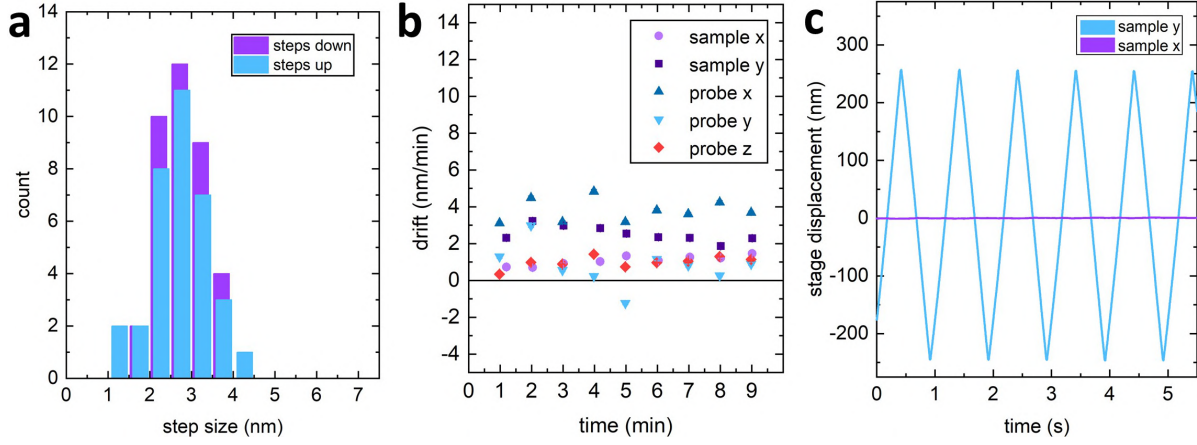


FIGURE 3.17. (a) histogram of average step size of the VPS in both upwards and downwards direction (b) evaluation of sample and probe drift in xy-plane as well as probe's drift in vertical  $z$  direction (c) cross-talk present in the system due to movement in orthogonal directions corresponds to 0.3% of the desired movement. Reproduced from [2]

If the sample stage was to be used as a SPM scanning unit, the cross-talk between  $Y$  &  $Z$  (horizontal) directions of sample stage movement needs to be investigated. Initially a cross-talk of the order of 10% was observed, however tuning the voltage between the 2 orthogonal directions, it was possible to significantly reduce the cross-talk. After applying the correction, the cross-talk was measured again (see Figure 3.17c) and found to be corresponding to about 0.3% of movement in the desired orthogonal direction, meaning that the new design of the stages is fully compatible to perform conventional SPM imaging.

### 3.6.6 Measuring Rotation Around X-axis

As previously explained, the present design allows the control of 4 degrees of freedom of the vertical oriented probe. Nevertheless, there are still 2 other degrees of freedom of the probe which are not adjustable in the current system. Ideally the cantilever should be oriented along the  $z$ -axis and as it bends, the tip should move along the  $y$ -axis. In practice, when the cantilever is mounted in the VPS, it can be rotated around the  $y$ -axis and around the  $z$ -axis (see figure 1.17). A small rotation around the  $y$ -axis has minor consequences, as the probe does not easily bend along the  $z$ -axis due to its

rectangular cross-section. Moreover, when the cantilevers are mounted in the first place, they can be pushed against a flat back of the clip, ensuring very small angle of rotation around the y-axis.

The rotation around the x-axis (azimuth angle) can have significant consequences when measuring in-plane forces. Due to the cylindrical shape of the plug in the VPS, it is harder to control the azimuth angle. For this reason, a simple method of evaluating this angle has been devised.

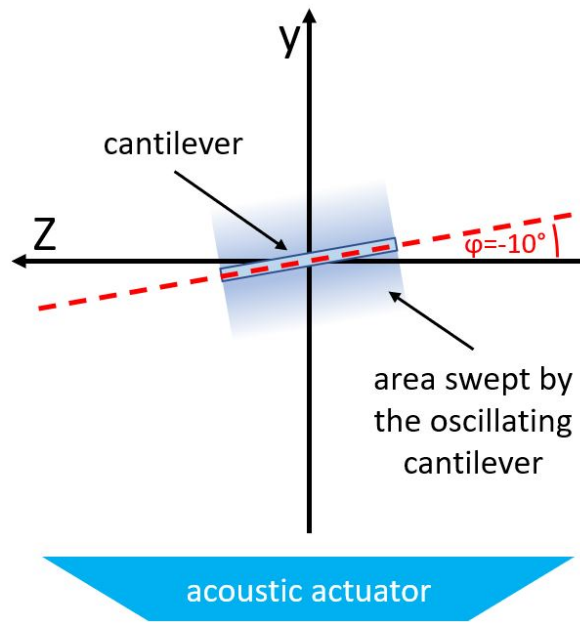


FIGURE 3.18. Schematic drawing of a scheme for evaluating the rotation of the probe around x-axis.

Once again, the cantilever is set in oscillation using the acoustic actuator, but this time we measure the oscillation of the tip in the y and z directions (i.e. in the plane of the sample), instead of the vertical movement used to adjust the tilt. The method relies on the fact that the small oscillation induced by the acoustic actuator will take place only in the direction of the low stiffness of the probe. If the movement of the tip is not entirely along the y-axis, it means that the azimuth angle  $\varphi$  is present. Hence the displacements in z or y directions, can be used to calculate the angle of rotation of the cantilever around x-axis. The azimuth angle  $\varphi$  is simply given by:

$$\varphi = \tan^{-1} \left( \frac{A_z}{A_y} \right) \quad (3.9)$$

where  $A_z$  and  $A_y$  are the amplitude of displacement measured in z and y axis respectively.

### 3.7 Bibliography

- [1] M. Antognozzi, A. Ulcinas, L. Picco, S. H. Simpson, P. J. Heard, M. D. Szczelkun, B. Brenner, and M. J. Miles, "A new detection system for extremely small vertically mounted cantilevers," *Nanotechnology*, vol. 19, p. 384002, Sept. 2008.
- [2] W. K. Szeremeta, R. L. Harniman, C. R. Bermingham, and M. Antognozzi, "Towards a Fully Automated Scanning Probe Microscope for Biomedical Applications," *Submitted to Sensors, Special Issue: Cantilever-Based Sensors*, 2020.
- [3] D. W. Pohl, W. Denk, and M. Lanz, "Optical stethoscopy: Image recording with resolution  $\lambda/20$ ," *Applied Physics Letters*, vol. 44, pp. 651–653, Apr. 1984.
- [4] E. Synge, "A suggested method for extending microscopic resolution into the ultra-microscopic region," *The London, Edinburgh, and Dublin Philosophical Magazine and Journal of Science*, vol. 6, pp. 356–362, Aug. 1928.
- [5] Y. De Wilde, P.-A. Lemoine, D. G. Seiler, A. C. Diebold, R. McDonald, C. M. Garner, D. Herr, R. P. Khosla, and E. M. Secula, "Review of NSOM Microscopy for Materials," in *AIP Conference Proceedings*, vol. 931, (Gaithersburg, MD), pp. 43–52, AIP, 2007.
- [6] W. Lukosz, "Optical Systems with Resolving Powers Exceeding the Classical Limit\*," *Journal of the Optical Society of America*, vol. 56, p. 1463, Nov. 1966.
- [7] W. Lukosz, "Optical Systems with Resolving Powers Exceeding the Classical Limit II," *Journal of the Optical Society of America*, vol. 57, p. 932, July 1967.
- [8] E. A. Ash and G. Nicholls, "Super-resolution Aperture Scanning Microscope," *Nature*, vol. 237, pp. 510–512, 1972.
- [9] Q. Cao, J. Feng, H. Lu, H. Zhang, F. Zhang, and H. Zeng, "Surface-enhanced Raman scattering using nanoporous gold on suspended silicon nitride waveguides," *Optics Express*, vol. 26, p. 24614, Sept. 2018.
- [10] R. R. Jones, D. C. Hooper, L. Zhang, D. Wolverson, and V. K. Valev, "Raman Techniques: Fundamentals and Frontiers," *Nanoscale Research Letters*, vol. 14, p. 231, Dec. 2019.

- [11] L. Novotny and N. van Hulst, “Antennas for light,” *Nature Photonics*, vol. 5, pp. 83–90, Feb. 2011.
- [12] A. Singh, P. M. de Roque, G. Calbris, J. T. Hugall, and N. F. van Hulst, “Nanoscale Mapping and Control of Antenna-Coupling Strength for Bright Single Photon Sources,” *Nano Letters*, vol. 18, pp. 2538–2544, Apr. 2018.
- [13] A. G. Curto, G. Volpe, T. H. Taminiau, M. P. Kreuzer, R. Quidant, and N. F. van Hulst, “Unidirectional Emission of a Quantum Dot Coupled to a Nanoantenna,” *Science*, vol. 329, pp. 930–933, Aug. 2010.
- [14] M. Antognozzi, C. R. Bermingham, R. L. Harniman, S. Simpson, J. Senior, R. Hayward, H. Hoerber, M. R. Dennis, A. Y. Bekshaev, K. Y. Bliokh, and F. Nori, “Direct measurements of the extraordinary optical momentum and transverse spin-dependent force using a nano-cantilever,” *Nature Physics*, vol. 12, pp. 731–735, Aug. 2016.
- [15] M. Baker, “Is there a reproducibility crisis?,” *Nature*, vol. 533, pp. 452–454, May 2016.
- [16] T. Scholz, J. A. Vicary, G. M. Jeppesen, A. Ulcinas, J. K. H. Hörber, and M. Antognozzi, “Processive behaviour of kinesin observed using micro-fabricated cantilevers,” *Nanotechnology*, vol. 22, p. 095707, Mar. 2011.
- [17] C. Agnew, E. Borodina, N. R. Zaccai, R. Conners, N. M. Burton, J. A. Vicary, D. K. Cole, M. Antognozzi, M. Virji, and R. L. Brady, “Correlation of in situ mechanosensitive responses of the *Moraxella catarrhalis* adhesin UspA1 with fibronectin and receptor CEACAM1 binding,” *Proceedings of the National Academy of Sciences*, vol. 108, pp. 15174–15178, Sept. 2011.
- [18] S. Magonov, V. Elings, and M.-H. Whangbo, “Phase Imaging and stiffness in tapping-mode atomic force microscopy,” *Surface Science*, vol. 375, pp. 385–391, 1997.
- [19] M. Antognozzi, H. Haschke, and M. J. Miles, “A new method to measure the oscillation of a cylindrical cantilever: “The laser reflection detection system”,” *Review of Scientific Instruments*, vol. 71, pp. 1689–1694, Apr. 2000.

- [20] M. Antognozzi, A. D. L. Humphris, and M. J. Miles, "Observation of molecular layering in a confined water film and study of the layers viscoelastic properties," *Applied Physics Letters*, vol. 78, pp. 300–302, Jan. 2001.
- [21] Y. F. Dufrêne, T. Ando, R. Garcia, D. Alsteens, D. Martinez-Martin, A. Engel, C. Gerber, and D. J. Müller, "Imaging modes of atomic force microscopy for application in molecular and cell biology," *Nature Nanotechnology*, vol. 12, pp. 295–307, May 2017.
- [22] R. L. Harniman, J. A. Vicary, J. K. H. Hörber, L. M. Picco, M. J. Miles, and M. Antognozzi, "Methods for imaging DNA in liquid with lateral molecular-force microscopy," *Nanotechnology*, vol. 23, p. 085703, Mar. 2012.
- [23] J. M. Fletcher, R. L. Harniman, F. R. H. Barnes, A. L. Boyle, A. Collins, J. Mantell, T. H. Sharp, M. Antognozzi, P. J. Booth, N. Linden, M. J. Miles, R. B. Sessions, P. Verkade, and D. N. Woolfson, "Self-Assembling Cages from Coiled-Coil Peptide Modules," *Science*, vol. 340, pp. 595–599, May 2013.
- [24] T. Ban, M. Hoshino, S. Takahashi, D. Hamada, K. Hasegawa, H. Naiki, and Y. Goto, "Direct Observation of A $\beta$  Amyloid Fibril Growth and Inhibition," *Journal of Molecular Biology*, vol. 344, pp. 757–767, Nov. 2004.
- [25] J. A. Varela, M. Rodrigues, S. De, P. Flagmeier, S. Gandhi, C. M. Dobson, D. Klenerman, and S. F. Lee, "Optical Structural Analysis of Individual  $\alpha$ -Synuclein Oligomers," *Angewandte Chemie*, vol. 130, pp. 4980–4984, Apr. 2018.
- [26] L. Novotny and B. Hecht, *Principles of Nano-Optics*. Cambridge University Press, 2012.
- [27] M. N. Bongiovanni, J. Godet, M. H. Horrocks, L. Tosatto, A. R. Carr, D. C. Wirthensohn, R. T. Ranasinghe, J.-E. Lee, A. Ponjavic, J. V. Fritz, C. M. Dobson, D. Klenerman, and S. F. Lee, "Multi-dimensional super-resolution imaging enables surface hydrophobicity mapping," *Nature Communications*, vol. 7, p. 13544, Dec. 2016.

- [28] J.-E. Lee, J. C. Sang, M. Rodrigues, A. R. Carr, M. H. Horrocks, S. De, M. N. Bongiovanni, P. Flagmeier, C. M. Dobson, D. J. Wales, S. F. Lee, and D. Klenerman, "Mapping Surface Hydrophobicity of  $\alpha$ -Synuclein Oligomers at the Nanoscale," *Nano Letters*, vol. 18, pp. 7494–7501, Dec. 2018.
- [29] C. R. Bermingham, I. Murillo, A. D. J. Payot, K. C. Balram, M. B. Kloucek, S. Hanna, N. M. Redmond, H. Baxter, R. Oulton, M. B. Avison, and M. Antognozzi, "Imaging of sub-cellular fluctuations provides a rapid way to observe bacterial viability and response to antibiotics," preprint, *Physiology*, Nov. 2018.
- [30] G. Longo, L. Alonso-Sarduy, L. M. Rio, A. Bizzini, A. Trampuz, J. Notz, G. Dietler, and S. Kasas, "Rapid detection of bacterial resistance to antibiotics using AFM cantilevers as nanomechanical sensors," *Nature Nanotechnology*, vol. 8, pp. 522–526, July 2013.
- [31] J. Vicary, A. Ulcinas, J. Hörber, and M. Antognozzi, "Micro-fabricated mechanical sensors for lateral molecular-force microscopy," *Ultramicroscopy*, vol. 111, pp. 1547–1552, Nov. 2011.
- [32] F. Gittes and C. F. Schmidt, "Thermal noise limitations on micromechanical experiments," *European Biophysics Journal*, vol. 27, pp. 75–81, Jan. 1998.
- [33] G. Binnig, C. F. Quate, and C. Gerber, "Atomic Force Microscope," *Physical Review Letters*, vol. 56, pp. 930–933, Mar. 1986.
- [34] B. L. M. Hendriksen and J. W. M. Frenken, "CO Oxidation on Pt(110): Scanning Tunneling Microscopy Inside a High-Pressure Flow Reactor," *Physical Review Letters*, vol. 89, July 2002.
- [35] H. L. Stern, R. Wang, Y. Fan, R. Mizuta, J. C. Stewart, L.-M. Needham, T. D. Roberts, R. Wai, N. S. Ginsberg, D. Klenerman, S. Hofmann, and S. F. Lee, "Spectrally Resolved Photodynamics of Individual Emitters in Large-Area Monolayers of Hexagonal Boron Nitride," *ACS Nano*, vol. 13, pp. 4538–4547, Apr. 2019.
- [36] D. W. Pohl, "Dynamic piezoelectric translation devices," *Review of Scientific Instruments*, vol. 58, pp. 54–57, Jan. 1987.
- [37] W. Han, J. Mou, J. Sheng, J. Yang, and Z. Shao, "Cryo Atomic Force Microscopy: A New Approach for Biological Imaging at High Resolution," *Biochemistry*, vol. 34, pp. 8215–8220, July 1995.

- [38] Z. Shao and Y. Zhang, “Biological cryo atomic force microscopy: A brief review,” *Ultramicroscopy*, vol. 66, pp. 141–152, Dec. 1996.
- [39] L. Qin, J. Zhang, J. Sun, D. M. Czajkowsky, and Z. Shao, “Development of a low-noise cryogenic atomic force microscope for high resolution imaging of large biological complexes,” *Acta Biochimica et Biophysica Sinica*, vol. 48, pp. 859–861, Sept. 2016.
- [40] B. Drevniok, W. M. P. Paul, K. R. Hairsine, and A. B. McLean, “Methods and instrumentation for piezoelectric motors,” *Review of Scientific Instruments*, vol. 83, p. 033706, Mar. 2012.
- [41] S. H. Pan, E. W. Hudson, and J. C. Davis, “ $^3\text{He}$  refrigerator based very low temperature scanning tunneling microscope,” *Review of Scientific Instruments*, vol. 70, pp. 1459–1463, Feb. 1999.
- [42] F. Marinello, M. Balcon, P. Schiavuta, S. Carmignato, and E. Savio, “Thermal drift study on different commercial scanning probe microscopes during the initial warming-up phase,” *Measurement Science and Technology*, vol. 22, p. 094016, Sept. 2011.





## ACHIEVING SUB-FN PRECISION MEASUREMENTS USING LMFM

The static mode force measurements in LMFM are based on Hooke's Law where the force is estimated through the displacement and the stiffness of the probe. The vertical orientation of the LMFM probes allows for the use of extremely soft cantilevers (see section 1.2). Moreover, the dimensions of the probe (length of  $120\mu\text{m}$ , further described in section 3.3) and the comparatively small displacement (rarely exceeding  $200\text{nm}$ ) mean that the small angle approximation holds and the Hooke's Law can be applied with confidence. Commercially available probes which can be purchased from NuNano [1] have thickness of either  $100\text{nm}$  or  $50\text{nm}$  corresponding to nominal force constants of the order of  $\sim 10^{-5}\text{N/m}$  and  $10^{-6}\text{N/m}$  respectively. Given these force constants, the position of the probe needs to be measured with sub-nanometer ( $< 10^{-9}\text{m}$ ) resolution to be able to achieve sub-femtonewton precision ( $< 10^{-15}\text{N}$ ). Part of the content of this chapter is included in the manuscript to be submitted to the journal Sensors - Special Issue: Cantilever-Based Sensors [2].

The force measurement procedure (and its associated error) described in this chapter is subsequently used throughout the rest of the thesis.

## 4.1 Experimental Procedure

All experiments were performed in ambient conditions using VWR borosilicate glass cover slips (thickness 1). Each cover slip was cleaned before measurements using one of the following two methods. First method was used for cover slips with small amount of contamination and was based on ethanol rinsing and subsequent drying with compressed nitrogen. The second method was used to clean cover glass with higher levels of contamination. The second method used a warm 5-minutes long ultrasonic bath in a 3% detergent solution (decon 90), followed by 6 warm 5-minutes long ultrasonic rinsing baths in Milli-Q water. Finally the cover glass was placed in an oven at 120°C till dry.

### 4.1.1 Displacement Measurements

Here we describe how to measure small displacements of the cantilever between two equilibrium positions when an intermittent force is applied. The force is provided by the interaction between the cantilever and the evanescent field generated by the TTL-modulated driving laser (laser #1 in figure 3.3). The probe's position is constantly measured with laser #2 at constant illumination, using the scattered evanescent wave detection system. It is clear from figure 4.1 that the positions of the tip cluster around two values depending on the laser being switched on or off.

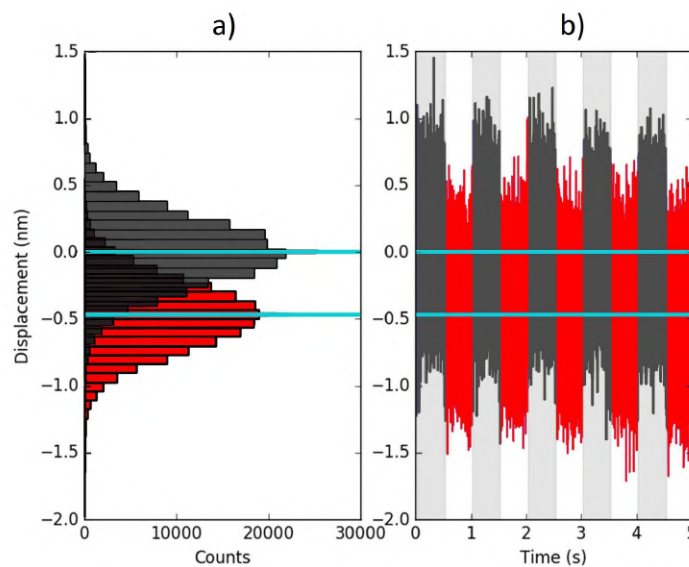


FIGURE 4.1. Visualisation of the principles behind displacement measurements

The precision with which one can measure the mean position of the scatterer and the associated standard error, depends on the amount of light scattered towards the detector. For example, if a  $2\mu\text{m}$  silica sphere is placed on the surface and moved side to side (whilst being illuminated with 40mW of laser power) it is possible to evaluate its displacement with sub-angstrom precision after just 15s (see figure 4.2). However a freely oscillating, soft cantilever in ambient conditions will be subjected

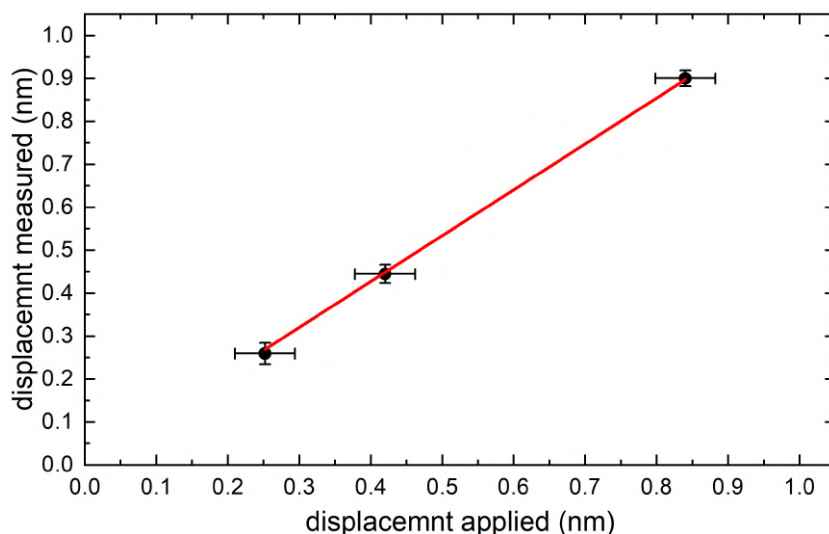


FIGURE 4.2.  $2\mu\text{m}$  silica spheres displacement measurement using a detection laser power of 40mW and a square waveform with a frequency of 15s.

to much larger thermal fluctuations [3], causing a significantly larger spread of the two equilibrium positions assumed by the probe. Nevertheless, because it is a thermal noise, that originates from Brownian motion, the position of the probe can be described using Gaussian distribution around an equilibrium position. When a force is applied to the probe, it shifts its equilibrium point, meaning that one can evaluate the displacement by comparing the two mean positions for 'off' and 'on' states.

The analysis of the data is made simpler by the fact the exact time when the force is switched on and off is known and this information can be used to separate the positions of the probe into two groups. To evaluate the effect of the intermittent force on the cantilever, the difference in the mean position is measured. For each of the 'on-off' cycles, the average position of 'off' is evaluated and subtracted from both the 'off' and corresponding 'on' averages. By doing so, the impact of drift, low frequency noise and random air currents is minimised. This method is not applicable when force steps are triggered by active samples such as a bio-molecular motor. In these cases a more complex

mathematical algorithm has to be used [4].

### 4.1.2 Auto-correlation study of data acquisition rate

When trying to establish the precision of the position measurements described in the previous section, one has to consider that the higher the data acquisition rate is, the more data points get collected in the same amount of time. As the error on measurement scales with  $1/\sqrt{n}$  it is tempting to use the highest acquisition rate possible to reduce the time needed to achieve suitable precision. However in practice, because of the dissipative mechanical response of the system, below a certain time scale, the position of the probe is no longer independent and data points start to become correlated. Calculating the autocorrelation for the probe movement [5] according to equation 1.1, can be used to establish the maximum sampling rate. Specifically the autocorrelation function is given by

$$\begin{aligned} A_{corr}(t) &= \int_{-\infty}^{\infty} y^*(t') \times y(t+t') dt' \\ &\propto e^{-t/t_c} \end{aligned} \quad (4.1)$$

where  $t_c$  is the characteristic relaxation time (or correlation time) of the system. In fact the relaxation time is related to the spring constant of the probe  $k$  and the hydrodynamic drag coefficient  $\gamma$  as follows [6, 7]

$$t_c = \frac{k}{\gamma}. \quad (4.2)$$

Therefore, data points recorded at a rate higher than the inverse of the correlation time cannot be considered statistically independent [8]. This means that, to establish the actual precision on the position measurements if acquired at a higher rate, the data needs to be decimated accordingly (see figure 4.3).

### 4.1.3 Calibration methods of the cantilevers' spring constant

One of the most common methods used for determining the stiffness of a mechanical sensors, makes use of the previously mentioned equipartition theorem [9]. For a simple harmonic oscillator, its Hamiltonian  $H$  can be written as

$$H = \frac{p^2}{2m} + \frac{1}{2}ky^2 \quad (4.3)$$

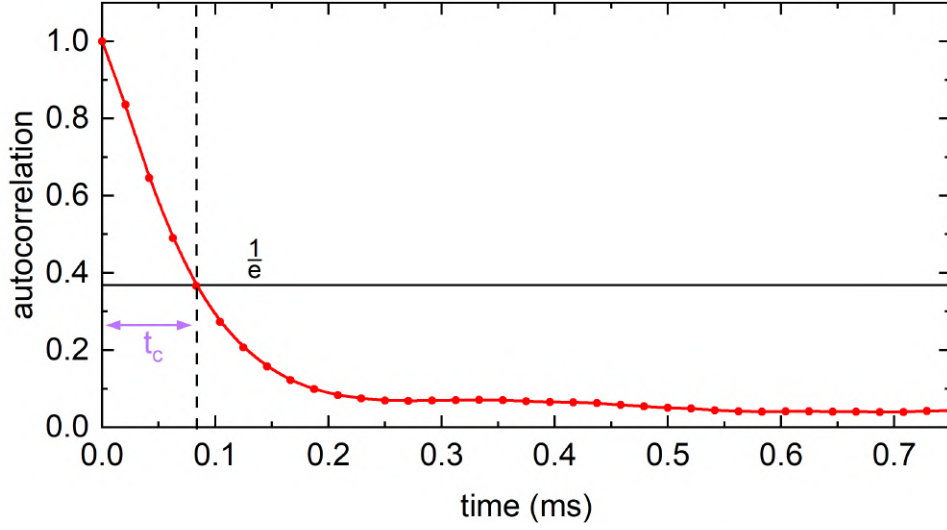


FIGURE 4.3. An example of autocorrelation of data evaluated for the purpose of decimation statistically dependent points.

where  $p$  is the momentum,  $m$  the mass and  $k$  the stiffness in the relative direction  $y$ . The equipartition theorem states that each degree of freedom will contribute on average  $\frac{1}{2}k_B T$  of energy. The cantilevers used in LMFM, because of their extreme difference in stiffness in the three dimensions ( $120\mu\text{m} \times 1.5\mu\text{m} \times 0.1\mu\text{m}$ ), can be considered as having only one degree of freedom (along the direction of lowest compliance), giving rise to the energy equipartition equation:

$$k = \frac{k_B T}{\langle y^2 \rangle}. \quad (4.4)$$

This method however only considers the first mode of oscillation, whilst neglecting higher modes, effectively underestimating the spring constant of the probe [1]. A further underestimation of the stiffness is caused by a broadening of the Gaussian distribution of positions due to drift in the signal. As the mean squared position ( $y^2$ ) is obtained by fitting the Gaussian distribution, any drift in the position signal causes the distribution to appear broader reducing the calculated stiffness of the cantilever.

An alternative method (and the method used throughout the project), commonly used for estimating the stiffness of an optical trap, is the Lorentzian method based on the Langevin equation [10]. Instead of looking at the position in the time domain, the Lorentzian method fits the power

spectrum density (PSD)  $S_y(f)$  in the frequency domain

$$S_y(f) = |y(f)|^2 \quad (4.5)$$

which is given by the absolute squared of the Fourier transformed position  $y(f)$ . In the time-domain, the Langevin differential equation of an over-damped harmonic oscillator driven by thermal energy is represented by

$$\gamma \frac{dy}{dt} + ky = F_B(t) \quad (4.6)$$

where  $F_B(t)$  is the random Brownian motion force with a time-averaged value of 0, and  $\gamma$  is the hydrodynamic drag coefficient. The PSD of the Brownian motion force is constant and can be calculated using the fluctuation dissipation theorem [11]

$$S_{FB}(f) = 4\gamma k_B T = \text{const.} \quad (4.7)$$

Taking a Fourier transform of the Langevin equation (4.6) transforms the equation in the frequency domain and gives

$$-i2\pi\gamma f y(f) + ky(f) = F_B(f) \quad (4.8)$$

which can be simplified by inserting the expression for a corner frequency  $f_c = k/2\pi\gamma$ , giving

$$2\pi\gamma(f_c - if)y(f) = F_B(f). \quad (4.9)$$

Combining equations (4.9) and (4.7) and inserting them into (4.5) gives a Lorentzian function of an over-damped oscillator

$$S_y(f) = \frac{k_B T}{\gamma\pi^2(f_c^2 + f^2)} \quad (4.10)$$

which correctly describes the power spectrum density of an ultra-soft micro-cantilever, as the ones used in this work. When  $f \gg f_c$ , the PSD decreases as  $S_y(f) \propto 1/f^2$ . Whereas, when  $f \ll f_c$ , the PSD becomes constant. The characteristic shape of the PSD is easiest to identify on a log-log scale as shown in figure 4.4 where the experimental PSD of a cantilever with spring constant of around  $5.4 \times 10^{-6} \text{N/m}$  is measured in ambient conditions and fitted using equation (4.10). With a very low quality factor  $Q$  of the cantilever, its first resonance peak which is expected around 8kHz cannot be observed, whilst higher modes are outside of the detector acquisition rate [1].

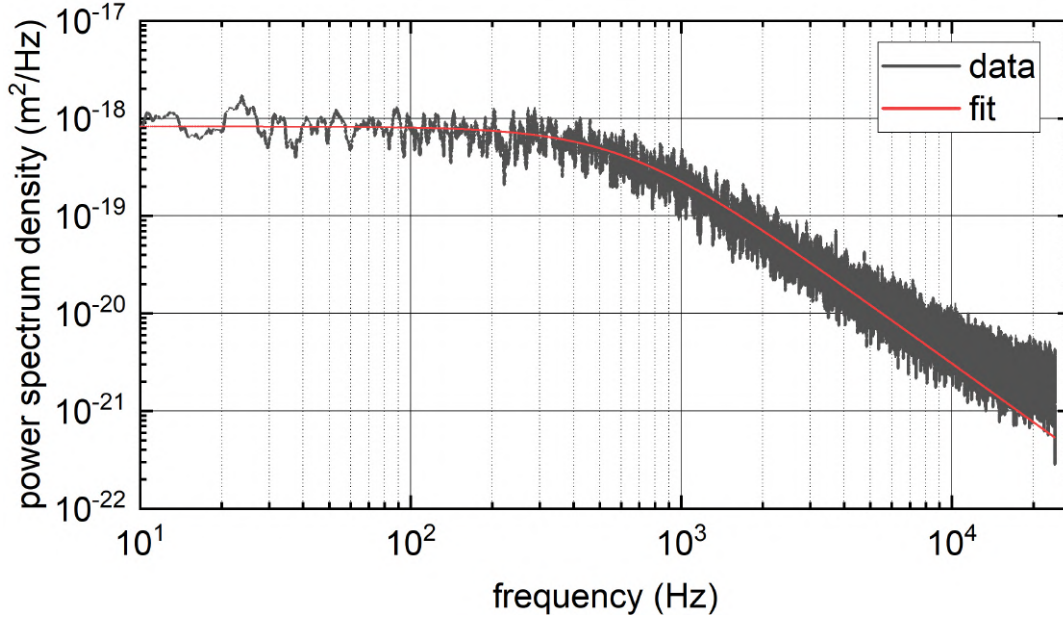


FIGURE 4.4. Power Spectrum Density data with a Lorentzian function fitted (red) for the purpose of spring constant evaluation. Value of  $5.395 \times 10^{-6} \text{ N/m}$  was found for this single fitting, with multiple fittings presented in figure 4.6

One other method to characterise the spring constant of an AFM cantilever is the Sader method [12–14], which makes use of both the Young’s modulus of the probe and the viscosity of the surroundings. However for the method to work properly, the dimensions of the probe, the viscosity of the medium and the Young’s modulus of the probe material need to be known with high accuracy making this method less attractive for the present application.

Experimentally, to improve the resolution of the PSD fitting routine, we use the collected time trace of the probe position recorded during the displacement measurements. We then divide these time traces into short (0.6s-1.1s) data sets. Each section is Fourier transformed and fitted using the Lorentzian function in equation (4.10). Each fit produces a stiffness value and the distribution of these values is used to calculate the mean stiffness of the cantilever with associated standard error.

## 4.2 sub-fN resolution

When combining cantilevers with extremely low stiffness with a position detection algorithm with nanometer resolution (as described in section 4.1.1), it becomes possible to measure force with



femtonewton or even sub-femtonewton resolution. Figure 4.5 shows the shift in the distribution of positions of a thermally fluctuation cantilever when a force of  $2.7\text{fN} \pm 0.2\text{fN}$  is applied. The force was produced by illuminating the cantilever tip with an intermittent evanescent field with a pulse duration of 0.5 s. The integration time necessary to obtain the required force resolution was 16 min. In practice, the force experienced by the probe was found calculating the separation between the means of the distributions with laser on and off while the error is derived from the standard deviation of the mean.

It is important to stress that, to achieve high accuracy when measuring forces using a micro-cantilever, it is essential to correctly evaluate its stiffness. For this reason we have dedicate a substantial effort to establish a robust calibration procedure as outlined in section 4.1.3. The stiffness calibration data used for the results in figure 1.5 are presented in figure 4.6.

Importantly, for shorter time accumulations, it is interesting to notice that it is still possible to achieve a precision of  $\pm 1\text{fN}$  by recording a time trace that is only 1min long. On the opposite side of the spectrum, stability of the system has allowed to perform a 3-hour-long measurement which was capable of detecting an optically induced force of only  $0.3\text{fN} \pm 0.1\text{fN}$  in magnitude.

The slight broadening of the 'on' distribution presented in figure 4.5 could be a result of either a small increase in the temperature of the system due to illumination, or the extra oscillations due to the laser output noise.

This level of force resolution in the femtonewton and sub-femtonewton range has been mainly accessible so far through the use of optical tweezers [15] and SPM is usually considered not suitable for this force regime. There have been however a few custom-made SPMs created which have demonstrated femtonewton and sub-femtonewton resolution. Most of these techniques perform measurements in either vacuum or close to absolute zero ( $< 5\text{K}$ ) [16–20] to reduce the impact of thermal noise on their measurements. Unfortunately, these experimental conditions are not suitable for biological applications where the high force sensitivity would be mostly required. A noteworthy setup has been presented by de Lépinay et al. [21] which is capable of measuring sub-femtonewton forces at room temperature in ambient conditions, where they observe the motion of a nanowire in two-dimensions.

The system described in the present work, has some clear advantages with respect to other force

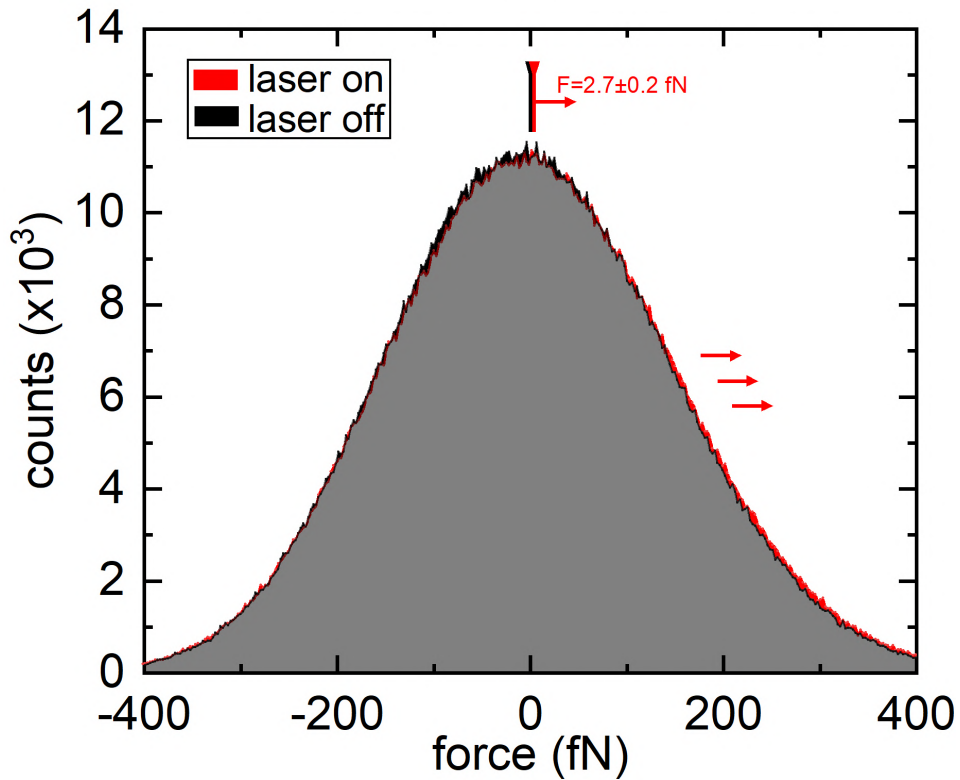


FIGURE 4.5. Force measurement with sub-fN precision. A shift in the positive direction of the force distribution upon laser illumination (red) is visible to the right of the grey area which corresponds to the 2 distributions overlapping. Reproduced from [2].

microscopy techniques. The high force resolution combined with the versatility of the system and the fact of using commercially available cantilevers, makes the LMFM a technique capable of consistently delivering high precision force measurements in a variety of environments.

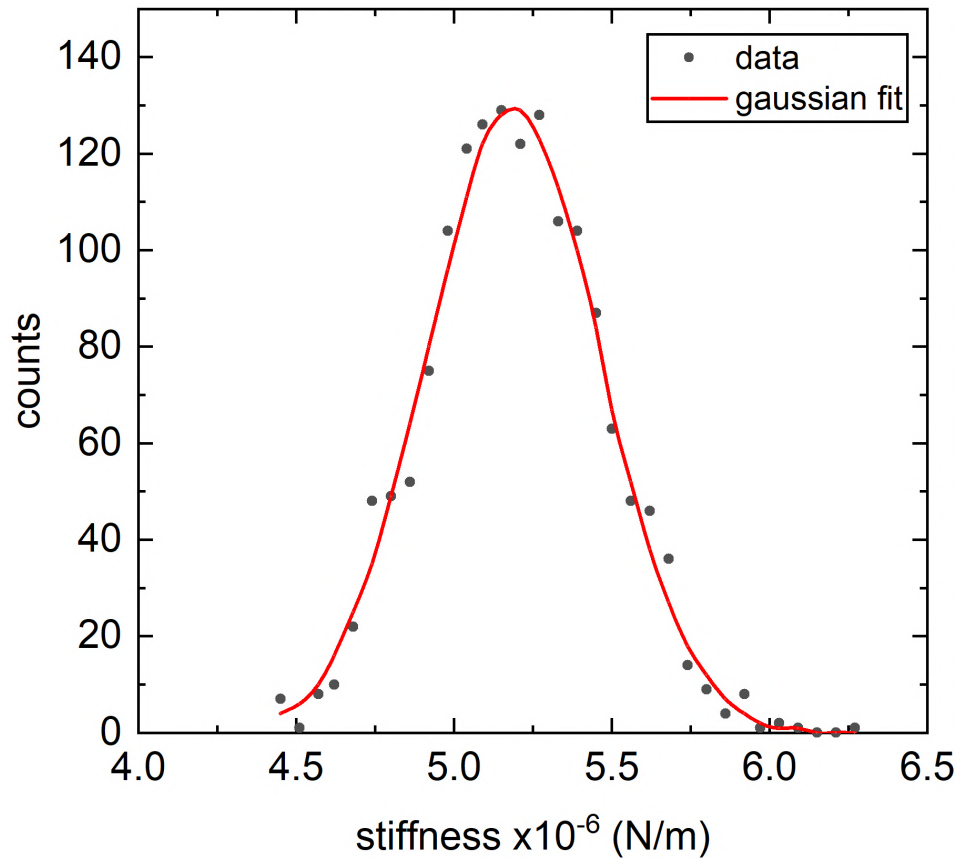


FIGURE 4.6. Probe stiffness histogram

### 4.3 Bibliography

- [1] J. Vicary, A. Ulcinas, J. Hörber, and M. Antognozzi, “Micro-fabricated mechanical sensors for lateral molecular-force microscopy,” *Ultramicroscopy*, vol. 111, pp. 1547–1552, Nov. 2011.
- [2] W. K. Szeremeta, R. L. Harniman, C. R. Bermingham, and M. Antognozzi, “Towards a Fully Automated Scanning Probe Microscope for Biomedical Applications,” *Submitted to Sensors, Special Issue: Cantilever-Based Sensors*, 2020.
- [3] B. Lukić, S. Jeney, C. Tischer, A. J. Kulik, L. Forró, and E.-L. Florin, “Direct Observation of Nondiffusive Motion of a Brownian Particle,” *Physical Review Letters*, vol. 95, p. 160601, Oct. 2005.
- [4] N. J. Carter and R. A. Cross, “Mechanics of the kinesin step,” *Nature*, vol. 435, pp. 308–312, May 2005.

- [5] A. Pralle, E.-L. Florin, E. Stelzer, and J. Hörber, “Local viscosity probed by photonic force microscopy,” *Applied Physics A: Materials Science & Processing*, vol. 66, pp. S71–S73, Mar. 1998.
- [6] C. Tischer, A. Pralle, and E.-L. Florin, “Determination and Correction of Position Detection Nonlinearity in Single Particle Tracking and Three-Dimensional Scanning Probe Microscopy,” *Microscopy and Microanalysis*, vol. 10, pp. 425–434, Aug. 2004.
- [7] M. Tassieri, F. D. Giudice, E. J. Robertson, N. Jain, B. Fries, R. Wilson, A. Glidle, F. Greco, P. A. Netti, P. L. Maffettone, T. Bicanic, and J. M. Cooper, “Microrheology with Optical Tweezers: Measuring the relative viscosity of solutions ‘at a glance’,” *Scientific Reports*, vol. 5, p. 8831, Aug. 2015.
- [8] M. P. Nicholas, L. Rao, and A. Gennerich, “An Improved Optical Tweezers Assay for Measuring the Force Generation of Single Kinesin Molecules,” in *Mitosis* (D. J. Sharp, ed.), vol. 1136, pp. 171–246, New York, NY: Springer New York, 2014.
- [9] J. L. Hutter and J. Bechhoefer, “Calibration of atomic-force microscope tips,” *Review of Scientific Instruments*, vol. 64, pp. 1868–1873, July 1993.
- [10] F. Gittes and C. F. Schmidt, “Thermal noise limitations on micromechanical experiments,” *European Biophysics Journal*, vol. 27, pp. 75–81, Jan. 1998.
- [11] R. Kubo, “The fluctuation-dissipation theorem,” *Reports on Progress in Physics*, vol. 29, pp. 255–284, Jan. 1966.
- [12] J. E. Sader, I. Larson, P. Mulvaney, and L. R. White, “Method for the calibration of atomic force microscope cantilevers,” *Review of Scientific Instruments*, vol. 66, pp. 3789–3798, July 1995.
- [13] J. E. Sader, J. W. M. Chon, and P. Mulvaney, “Calibration of rectangular atomic force microscope cantilevers,” *Review of Scientific Instruments*, vol. 70, pp. 3967–3969, Oct. 1999.
- [14] J. E. Sader, R. Borgani, C. T. Gibson, D. B. Haviland, M. J. Higgins, J. I. Kilpatrick, J. Lu, P. Mulvaney, C. J. Shearer, A. D. Slattery, P.-A. Thorén, J. Tran, H. Zhang, H. Zhang, and T. Zheng, “A virtual instrument to standardise the calibration of atomic force microscope cantilevers,” *Review of Scientific Instruments*, vol. 87, p. 093711, Sept. 2016.

- [15] G. Ranjit, D. P. Atherton, J. H. Stutz, M. Cunningham, and A. A. Geraci, “Attonewton force detection using microspheres in a dual-beam optical trap in high vacuum,” *Physical Review A*, vol. 91, May 2015.
- [16] F. Mueller, S. Heugel, and L. J. Wang, “Femto-Newton light force measurement at the thermal noise limit,” *Optics Letters*, vol. 33, p. 539, Mar. 2008.
- [17] J. G. Longenecker, E. W. Moore, and J. A. Marohn, “Rapid serial prototyping of magnet-tipped attonewton-sensitivity cantilevers by focused ion beam manipulation,” *Journal of Vacuum Science & Technology B, Nanotechnology and Microelectronics: Materials, Processing, Measurement, and Phenomena*, vol. 29, p. 032001, May 2011.
- [18] Y. W. Kim, H. H. Choi, J.-H. Choi, and S.-G. Lee, “Fabrication and characterization of an attonewton-sensitivity Si cantilever with an Nb micro-ring,” *Journal of the Korean Physical Society*, vol. 60, pp. 973–977, Apr. 2012.
- [19] S. A. Hickman, E. W. Moore, S. Lee, J. G. Longenecker, S. J. Wright, L. E. Harrell, and J. A. Marohn, “Batch-Fabrication of Cantilevered Magnets on Attonewton-Sensitivity Mechanical Oscillators for Scanned-Probe Nanoscale Magnetic Resonance Imaging,” *ACS Nano*, vol. 4, pp. 7141–7150, Dec. 2010.
- [20] H. J. Mamin and D. Rugar, “Sub-attonewton force detection at millikelvin temperatures,” *Applied Physics Letters*, vol. 79, pp. 3358–3360, Nov. 2001.
- [21] L. M. de Lépinay, B. Pigeau, B. Besga, P. Vincent, P. Poncharal, and O. Arcizet, “A universal and ultrasensitive vectorial nanomechanical sensor for imaging 2D force fields,” *Nature Nanotechnology*, vol. 12, pp. 156–162, Oct. 2016.

## OPTICALLY INDUCED UNIDIRECTIONAL BENDING IN Si<sub>3</sub>N<sub>4</sub> CANTILEVERS

When performing force measurements at the nanoscale, it is important to remember that a micro-cantilever is a mechanical element and can respond to external force fields in non-trivial ways. In particular, a probe is not only sensitive to the forces investigated, but it is also susceptible to other forces present at that scale (such as Van der Waals or electrostatic interaction) and furthermore, the environment can also affect the measurement (e.g. pH of the surroundings, temperature and the affect it has on the structure of the probe etc).

This chapter focuses on the investigation into a secondary effect that manifested during the investigations into optical forces in evanescent field. The extra force observed is referred to with the general term 'bias bending' as the exact origin is not completely understood. In simple terms, we observed that when a vertically oriented micro-cantilever enters an evanescent field, it invariably experiences a bending towards one of its sides.

To better understand the problem, the following convention (see figure 5.1) for describing the orientation of the cantilever with respect to rotation around x-axis has been introduced. Consistently with previous notation, laser #1 propagates along the z-axis, whilst laser #2 propagates in the (-y) direction. By using both lasers for this investigation, it is not necessary to rotate the cantilever in all the orientations described in figure 5.1, but it is sufficient to study positions 'A' and 'C' with laser 1 and 2 propagating at 90° with respect to each other. Additionally, readers may find figure 3.2 useful.

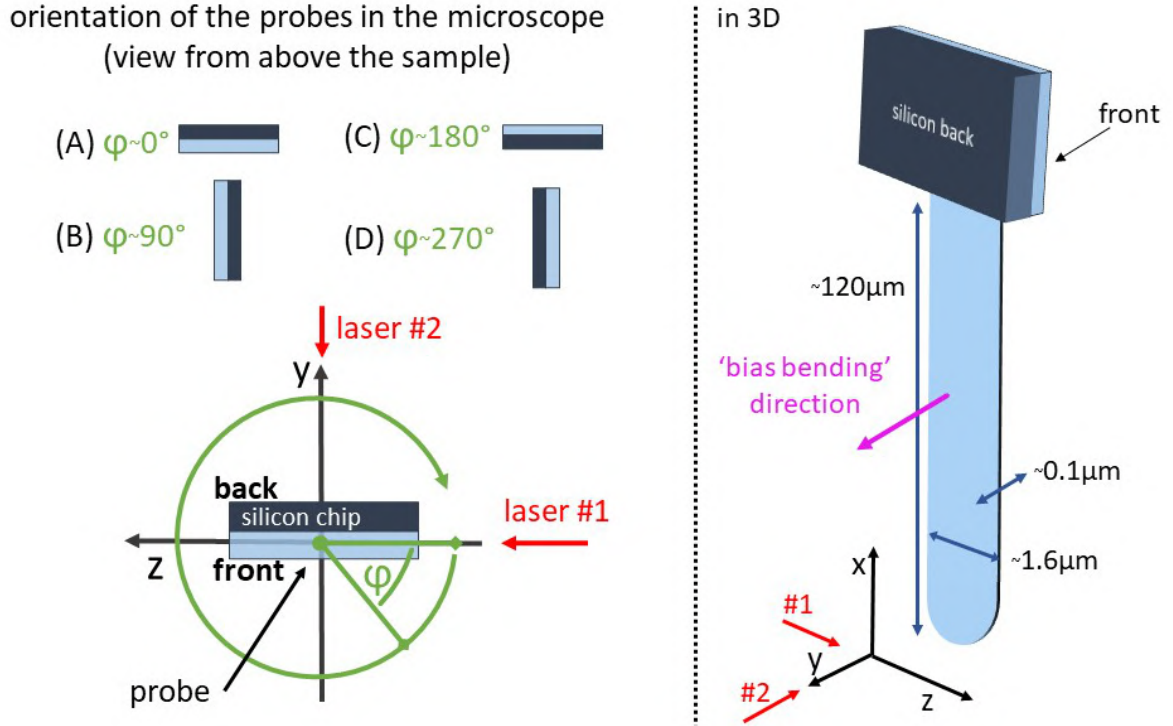


FIGURE 5.1. Diagram illustrating the cantilever orientation convention as well as the direction of the propagation of the evanescent field. It is crucial for understanding the experiments presented in the following chapters. Cantilever in 3D is in orientation 'A'.

The design and optimisation of the cantilever modifications (section 5.3), the EDX of the cantilevers and the photostriction consideration (section 5.5) was done in collaboration with final year undergraduate students Jake Sheridan and Sophia Wisniewska. The etching of the cantilevers using FIB was performed with Dr. Christopher Jones and Dr. Tomas Martin from Interface Analysis Centre at the School of Physics at the University of Bristol. The ellipsometry was carried out with Dr. Andrew Murray in clean room facilities in School of Physics at University of Bristol.

## 5.1 Initial Observations

When performing measurements using LMFM with NuNano  $\text{Si}_3\text{N}_4$  probes [1], an optically induced force is observed in addition to the optical forces expected from the theoretical considerations described in chapter 2. Initially, this 'bias force' was observed and attributed to the force associated

with orbital momentum [2] described in equations (2.32) and (2.76). However, subsequently this was shown not to be correct. The initial overview of the problem is best summarised by the results collected in figure 5.2.

The diagram shows the direction of the force measured by the probe, depending on its orientation (either 'A' or 'C' (as described in figure 5.1)), the laser beam direction and the laser polarisation indicated by the large black letters (S,L,R are the s-polarisation, left-handed elliptical and right-handed elliptical respectively). It can be seen that the measurements performed with the probe in orientation 'A' show the cantilever always deflecting in (+y) direction, whereas the probe in orientation 'C' always deflects in (-y) direction. From these results it is clear that the cantilever in an evanescent field always bends towards the side contacting the silicon chip (denoted as 'back' in figure 5.1).

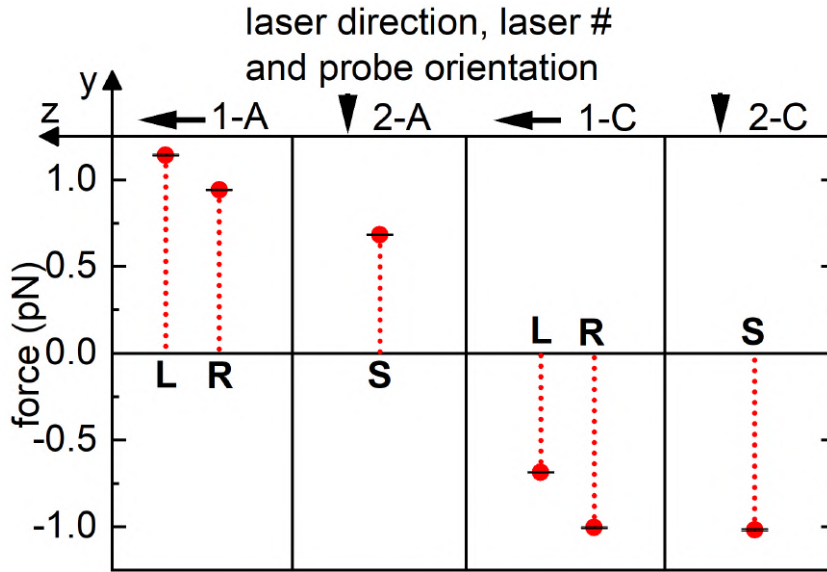


FIGURE 5.2. Summary of the initial bias bending observations. Presented are results of force measured by the probe, depending on its orientation (either A or C (see figure 5.1)), laser direction and laser polarisation indicated with large black letters (S,L,R are the s-polarisation, left-handed elliptical and right-handed elliptical respectively). All measurements performed with the probe in orientation 'A', show the cantilever always deflecting in +y direction, whereas the probe in orientation 'C' always deflects in -y direction.

To try to identify the cause of this bias bending, all the possible explanations were divided into 3 categories depending on where or what could be the triggering factor: (1) the interaction of light with



the tip of the probe, like an asymmetric scattering by the tip of the cantilever, (2) as the consequence of how the evanescent field is created in LMFM, and (3) due to the evanescent wave coupling inside the cantilever.

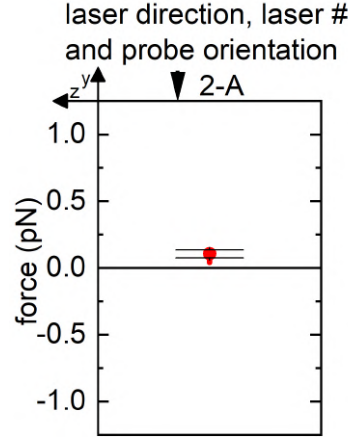


FIGURE 5.3. Evidence of the bias bending as measured using a cantilever in orientation A with a  $2\mu\text{m}$  silica sphere attached to the tip (thus ensuring that only a sphere is directly interacting with the evanescent field).

The first hypothesis was extensively investigated in previous work [3, 4] using an older version of the microscope, where the geometry of the tip was modified in various manner. The effect of the modifications of the probe's tip, on the force measured, was limited. It was concluded that the tip does affect the bias bending, but only with respect to the magnitude and not its overall direction. Figure 5.3 contains results for the force measured by a cantilever with a  $2\mu\text{m}$  silica sphere attached to the tip (the method for attaching spheres is described in detail in chapter 6), with only the sphere interacting with the evanescent field. If asymmetric scattering was the origin of the bias bending, a tip with spherical geometry was expected to no longer be affected by the 'bias force' and be able to measure the longitudinal orbital momentum described in equations (2.32) and (2.76) in the direction of the propagation of the wave ( $-y$ ). The fact that the cantilever deflected in the opposite direction, which is in stark contrast to studies showing the effect of evanescent fields on dielectric spheres [5, 6]. This result is a good indication that the 'bias bending' is still present, even with a symmetrical tip. In all cases of modifying the symmetry of the probe, the effect of the modifications was limited to a reduction of the magnitude of the bias effect.

### 5.1.1 Evanescent wave dependence (2-prism setup)

Before considering the most plausible hypothesis that the bias bending is caused by light coupling into the cantilevers, it was necessary to exclude that the particular way of producing the evanescent field was not responsible for the effect.

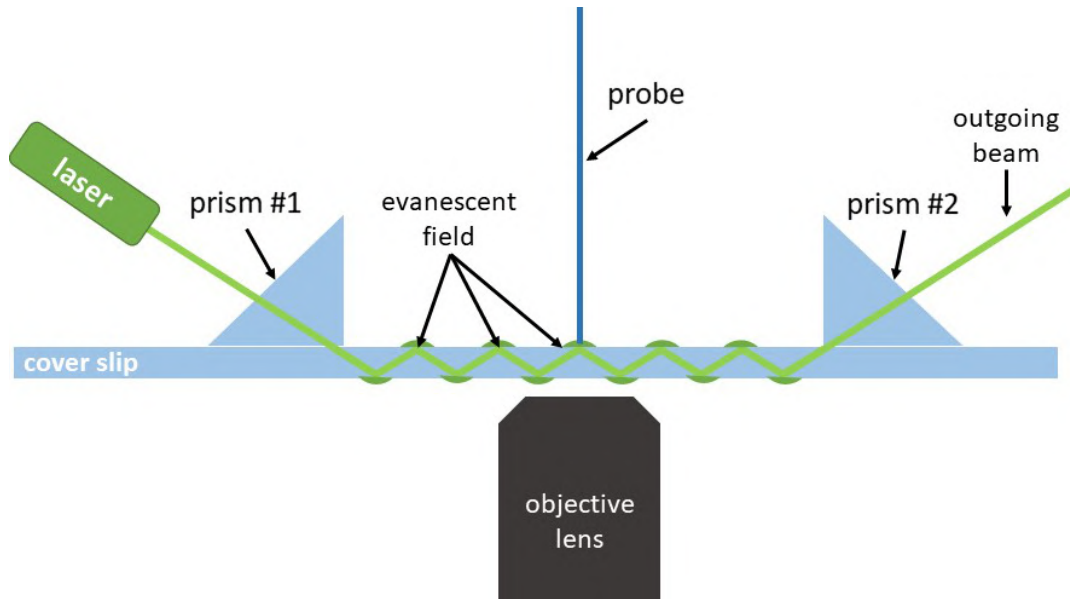


FIGURE 5.4. Diagram illustrating the 2 prism setup

It is well documented that the method of generating total internal reflection using a high numerical aperture objective is not perfect due to the presence of 'stray light scattering' which can originate within the objective lens itself [7–11]. If such a stray beam were to illuminate the base of the cantilever, it would open up the potential for a bimetallic strip effect in that region [12]. Taking into account that the length of the cantilevers is the same in all experiments and the probes are aligned in the same manner for each experiment; it is possible that such a stray ray could hit the same part of the cantilever each time.

In order to investigate this possible source of bias bending a different setup for creating the evanescent field was implemented (see figure 5.4). Two prisms were placed on the top surface of a cover-slip and optically coupled using a thin layer of index-matching immersion oil in between [7]. The s-polarised ( $\lambda = 532\text{nm}$ ) laser was aligned at an angle to create a set of total internal reflections within the cover slip. The second prism was crucial to extract the light from the cover slip in order to

ensure no back reflection of the coupled beam, which could create a counter propagating evanescent wave in the region of interest.

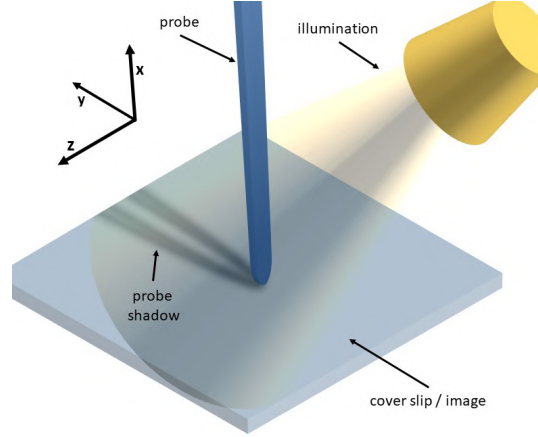


FIGURE 5.5. Diagram illustrating how the cantilever can be observed using the CMOS camera by utilising an external light source and casting a shadow

Crucially for this setup, there cannot be any immersion oil present in between the cover slip and the objective lens, as the light coupled inside the glass would propagate into the oil layer and destroying total internal reflection within the coverslip. The consequence of lack of immersion oil significantly reduces the collecting angle of the objective lens is severely limited, to the point that the SEW detection system no-longer works as the signal reaching the detector is too weak to register the movement within the noise. However a sufficiently high laser power, can produce a deflection directly observable using the CMOS Camera once the cantilever is illuminated as shown in figure 5.5.

Images presented in figure 5.6 were recorded for probes in 2 orientations. The top row (a,b) contains results from cantilever in orientation 'A', whilst the bottom row contains images taken for the cantilever in orientation 'C'. The blue vertical line indicates an approximate position of the tip of the probe in (y) direction when the laser is off. The green line indicates the position of the tip when illuminated by the laser. These images show that regardless of the method used for generating the evanescent field, the probe always moves towards the back of the silicon chip, confirming that the bias bending is triggered by the interaction with the evanescent field, and it is an intrinsic property of the cantilever.

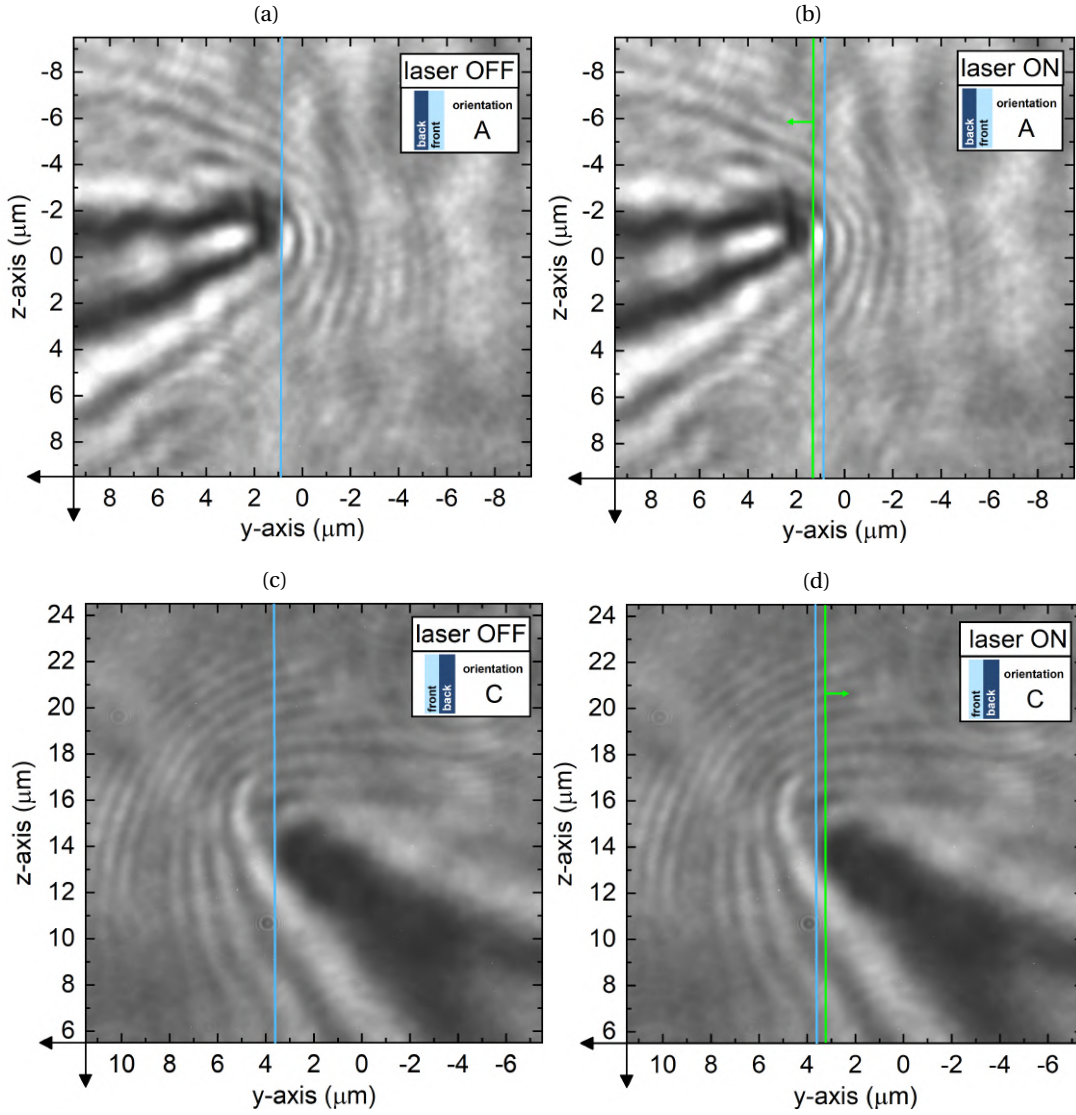


FIGURE 5.6. Images of the probe position, recorded using CMOS camera for the purpose of investigating bias bending in 2-prism setup. Cantilevers were in orientations A (a,b) and C (c,d) explained in figure 5.1. The blue line indicates an approximate position of the tip of the probe in y-direction when the laser is off (for respective orientations). The green line indicates the position of the tip when illuminated by the laser.

## 5.2 Light coupling within the cantilever and its polarisation dependence

The most plausible hypothesis explaining the origin of the bias bending is related to a photo-induced effect which could be triggered by the evanescent field coupling within and propagating inside the cantilever. With the refractive index of silicon nitride ( $n_{\text{Si}_3\text{N}_4} = 2.268$ ) being higher than both the air ( $n_{\text{air}} = 1$ ) and the glass ( $n_{\text{glass}} = 1.518$ ), it is reasonable to expect that the light could couple within the cantilever through frustrated total internal reflection and then supporting its propagation inside, acting as a waveguide.

To investigate such possibility, 2 types of numerical simulations were used. Numerical methods are often employed to help investigate the propagation of electromagnetic waves in geometrically intricate setups, where analytical solutions are not feasible. Real-life systems tend to have irregular geometries, making computer modelling the only method for solving Maxwell's equations. With the extreme length-scale difference between the three dimensions of the cantilevers used, which also includes curved surfaces, numerical techniques are the only tool to investigate the coupling of the evanescent field.

### 5.2.1 Simulation methods, FDTD and DGTD

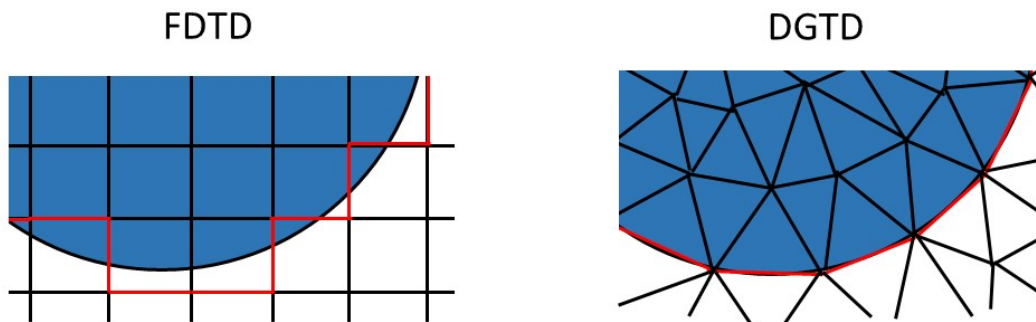


FIGURE 5.7. Diagram illustrating the difference between a rectangular grid and an adaptive mesh

The 4 Maxwell's equations that need to be solved by the simulation are

$$\left\{ \begin{array}{l} \nabla \times \mathbf{E}(\mathbf{r}, t) = -\frac{\partial \mathbf{B}(\mathbf{r}, t)}{\partial t} \\ \nabla \times \mathbf{B}(\mathbf{r}, t) = \frac{1}{c^2} \frac{\partial \mathbf{E}(\mathbf{r}, t)}{\partial t} + \mu_0 \mathbf{J}(\mathbf{r}, t) \\ \nabla \cdot \mathbf{E}(\mathbf{r}, t) = \frac{1}{\epsilon_0} \rho(\mathbf{r}, t) \\ \nabla \cdot \mathbf{B}(\mathbf{r}, t) = 0 \end{array} \right. \quad (5.1)$$

where  $\mathbf{B} = \mu \mathbf{H}$ ,  $\mathbf{D} = \epsilon \mathbf{E}$  and where  $\rho$  is the charge density and  $\mathbf{J}$  is the current density. It can be shown that if the initial conditions satisfy the 3<sup>rd</sup> and 4<sup>th</sup> equation, they will be satisfied at all times [13]. Hence numerical methods such as FDTD and DGTD only consider the first 2 of the Maxwell's equations (5.1).

The Finite Difference Time Domain (FDTD) is a widely used computational method which discretizes the 2D (or 3D) space, using Cartesian coordinates, into uniform rectangular grid (or cuboidal grid in 3D) [14]. This allows to calculate the electromagnetic field using the differential form of Maxwell's equations, which can be written as

$$\left\{ \begin{array}{l} -\frac{\partial B_i}{\partial t} = \frac{\partial E_k}{\partial j} - \frac{\partial E_j}{\partial k} \\ \frac{\partial D_i}{\partial t} = \frac{\partial H_k}{\partial j} - \frac{\partial H_j}{\partial k} - J_i \end{array} \right. \quad (5.2)$$

where the indices  $i, j, k$  can be rotated for each dimension as follows  $(i, j, k) = (x, y, z) \rightarrow (y, z, x) \rightarrow (z, x, y)$  [14, 15]. The FDTD method provides a very intuitive computational scheme especially when applied to the Yee grid (staggered grid) [14]. The fact that the method is a time domain simulation, it allows an easy description of the evolution of the electromagnetic field within the system, giving easy access to the evolution of the field inside the system in time. However, the intuitive cuboidal grid turns out to be one of its major weaknesses as the grid struggles with curved or non parallel surfaces, leading to a staircase effect (see figure 5.7). Furthermore, depending on the geometry of the system, FDTD can be computationally expensive, which is the case for the geometries involved in this experiment, as the mesh spacing in FDTD simulations is determined by the beam wavelength and smallest geometrical features [14]. For the experimental setup investigated here, it leads to a large volume of points that need to be computed, even if in the majority of cases they will only represent an empty space.

Discontinuous Galerkin Time Domain (DGTD) is an alternative method, which combines the advantages of adaptive meshing (predominantly used in Finite Element Method) with the time-domain aspect of FDTD [13, 16–18]. The use of an adaptive mesh (see figure 5.7) allows to approximate curved surfaces much better than with a cuboidal grid. Furthermore, it also allows for a significantly more sparse mesh in uniform regions (saving computational resources). The adaptive mesh in DGTD is made out of variable size triangles in 2D and tetrahedrons in 3D. The differential form of equations (5.2) will no longer be suitable, and for this reason DGTD method evaluates the integral version of Maxwell's equation over the volume of each element. Another major difference when using DGTD simulation is that initially the calculations are performed for each element separately, only the following step involves setting the boundary conditions according to the field found in their neighbouring volumes and exchanging the flux through adjacent surfaces. As a consequence, evaluating electromagnetic flux going through a desired surface can be done easily and with high precision.

Both the FDTD and DGTD methods were used to investigate the evanescent wave coupling hypothesis for the bias bending. Each method was preferred depending on what information was needed and the available computational resources. The well established simulation software package (Lumerical: High-Performance Photonic Simulation Software) was used to perform the simulations.

### 5.2.2 Finding refractive index of cantilevers using ellipsometry

Ellipsometry is a commonly used technique designed to determine the refractive indices and thickness of thin film materials [19], through measuring the changes in the polarisation ellipse which are governed by Fresnel coefficients of reflection. J.A. Woollam RC2 Spectroscopic Ellipsometer was used to find the refractive index of silicon nitride cantilevers used throughout this project (see figure 5.8). This optical parameter is of fundamental importance to ensure realistic numerical simulations.

### 5.2.3 Effect of the polarisation on bias bending

As the refractive index of silicon nitride is significantly higher than the refractive index of glass, total internal reflection at the glass surface is frustrated in the  $\text{Si}_3\text{N}_4$  medium. Due to the specific geometry of the cantilever as well as the low refractive index of the surrounding medium ( $n_{air} = 1$ ) light can

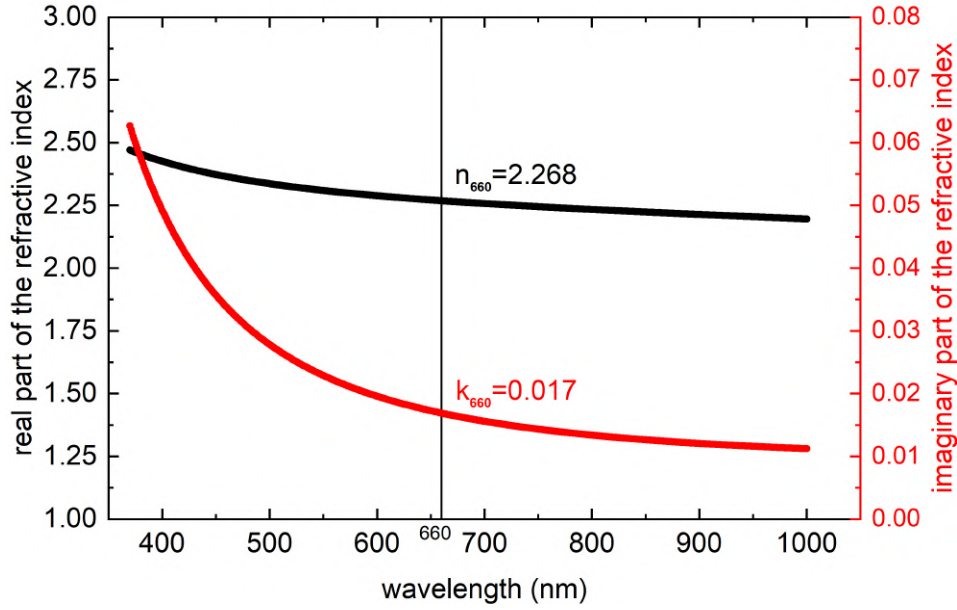


FIGURE 5.8. Refractive index of silicon nitride cantilevers measured via ellipsometry

propagate within it like in a waveguide. The cutoff wavelength  $\lambda_c$  in a waveguide with rectangular cross-section is given by the following expression

$$\lambda_c = \frac{2}{\sqrt{(\frac{a}{w})^2 + (\frac{b}{t})^2}} \quad (5.3)$$

where  $w$  and  $t$  are width and thickness of the cantilever respectively, whilst  $a$  and  $b$  are the integer mode numbers for TE or TM propagation. Equation (5.3) suggests a possibility of modes being supported for  $\lambda_0 = 660\text{nm}$ . Most commonly, light is coupled into a waveguide using a high numerical aperture lens. However, in the case of a vertical cantilever in an evanescent field, light couples upon frustrating a totally internally reflected beam, with a well defined incidence angle and a direction of propagation with respect to cantilever's orientation (see figure 5.1). This will produce an asymmetric light propagation, similar to ones observed in multi-mode interferometers [20–22]. Furthermore, the curvature of the tip will lead to a divergence of the light coupled inside the cantilever, resulting in mode dispersion.

As the propagation of light inside a waveguide is dependent on the polarisation. The dependency of the bias bending on the polarisation and the power of the incidence beam was measured. The LCVR was used to generate either s-polarised or p-polarised light and the power output of laser #1



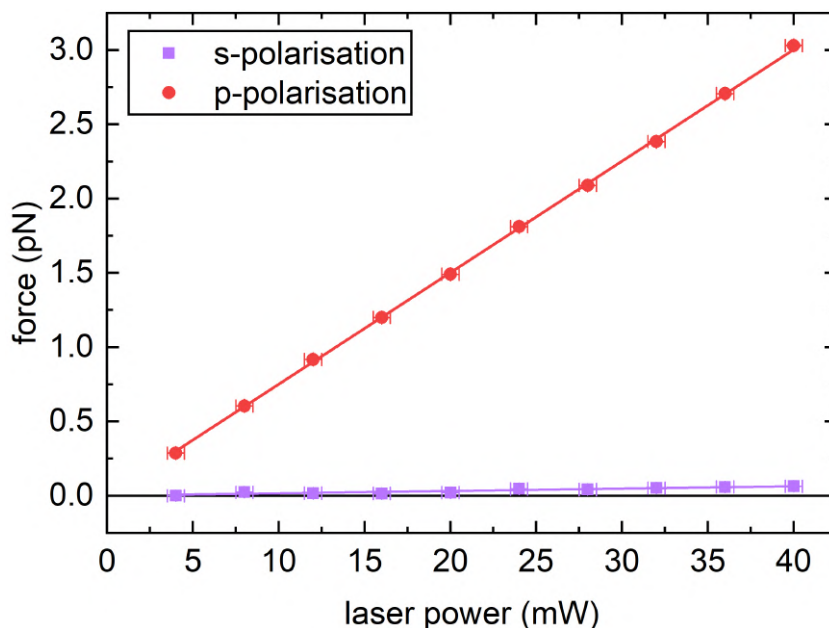


FIGURE 5.9. Bias bending converted into the magnitude of the force experienced by the cantilever in orientation 'A' according to the polarisation of the incident beam (for laser #1).

was varied between 4mW and 40mW with 4mW increments ( $\pm 0.5$ mW). The cantilever was positioned in orientation 'A' (as described in figure 5.1). Results of these measurements can be seen in figure 5.9. Two main conclusions can be drawn from the presented data. Firstly, the bias bending is linearly dependent on the power of laser at constant polarisation. Secondly, the response to p-polarised light is significantly stronger than to s-polarised light. In fact s-polarised light deflection is equivalent to just  $2.0\% \pm 0.1\%$  of p-polarised counterpart. This magnitude discrepancy cannot be explained by the difference in Fresnel coefficients (see equations (2.49) and (2.48)) between p-polarised and s-polarised beams. On the other hand, we know that the LCVR does not produce a pure linearly polarised beam. Due to the large effect of p-polarised light on the cantilever, it is sufficient that a small fraction of light exiting the device was still p-polarised to produce a non-zero response of the cantilever when illuminated with s-polarised light.

#### 5.2.4 3D simulations of cantilevers under s-polarised and p-polarised illumination

Using FDTD simulations, the hypothesis suggested in section 5.2.3 was numerically investigated. A 3-dimensional simulation was set up, which included the glass ( $n = 1.518$ ) to air interface at  $x=0$ . The

evanescent field was created by simulating a Gaussian beam propagating in  $xz$ -plane with an incident angle  $\alpha = 55^\circ$ , a waist diameter of  $6\mu\text{m}$  and a wavelength of  $\lambda = 660.0\text{nm} \pm 0.1\text{nm}$ . The simulation assumed a cantilever of thickness  $t = 100\text{nm}$  along  $y$ -axis, width of  $w = 1650\text{nm}$  along  $z$ -axis and length spanning beyond the simulation region in the  $(+x)$  direction (which corresponds to both 'A' and 'C' orientations). The cantilever tip was positioned  $30\text{nm}$  above the glass-air interface. The idealised model of the probe included the semicircular tip. Two simulations were performed with s-polarisation and p-polarisation beam.

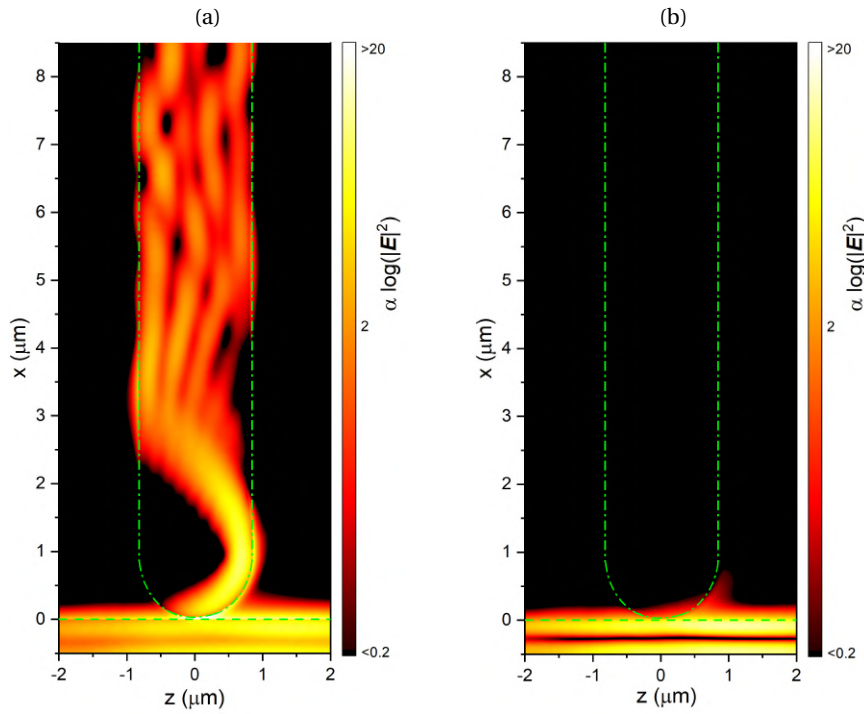


FIGURE 5.10. Cross section of 3D simulation results of light coupling inside the probes for (a) p-polarised and (b) s-polarised light. The green dashed line indicates the outline of the cantilever, whilst the glass to air boundary is at  $x=0$ . The evanescent field is generated by total internal reflection of a Gaussian beam incident onto a glass-air interface at an angle of  $\alpha = 55^\circ$ , propagating in  $xz$ -plane with a positive  $k_z$  component (left to right).

Figure 5.13 shows the simulation of the intensity of the electric field through the cross section of the simulation region in the  $xz$ -plane at  $y = 0$  for both polarisation states. The simulation results strongly suggests that an evanescent wave can couple inside the  $\text{Si}_3\text{N}_4$  cantilever having dimensions similar to the ones used in our experiments. Moreover, for the 'A' and 'C' orientations only the

p-polarised component of light can couple in. These results are in strong agreement with the experimental results presented in figure 5.9 and support the hypothesis that the bias bending is triggered by the light coupling inside the cantilever.

### 5.3 Removing Bias Bending

Thus far, the evidence presented supports the hypothesis that the bias bending being caused by the light coupled into the silicon nitride probe. The argument would be almost conclusive if one could stop the light from coupling in and measure the effect on bias bending. A possible way to produce this effect would be to taper the probe. However doing so, would result in a significantly lower scattering signal, preventing the SEW detection system from achieving the desired sensitivity. The high refractive index of the cantilever and its geometry makes the coupling of light through the frustration of total internal reflection difficult to stop.

A potential answer to this problem was identified, where instead of stopping the light from coupling in, the probe would be modified in such a manner, that the light which does couples in, is refracted out of the cantilever almost immediately. Such solution would therefore stop the light from propagating along the length of the probe. Two different schemes were developed as potential solutions, simulated and experimentally tested and the results are presented in the following sections.

#### 5.3.1 Triangular Cutout Scheme

The triangular cutout scheme is based on a simple ray diagram consideration. Initially, when the light couples inside the cantilever, its trajectory is determined by the angle of incidence through Snell's Law. The beam propagating within the cantilever remains narrow before reaching the edge of the cantilever (see figure 5.2.4a). By cutting out a triangular shape in the region of the first intended internal reflection and adjusting its angle accordingly, it is possible to refract the coupled beam out of the cantilever.

To optimize the geometry of the triangular cutout scheme (presented in figure 5.11), a simple python code was created. The program would account for slightly varying widths of the cantilevers (originating from the manufacturing process) as well as to find a robust design with a margin of error

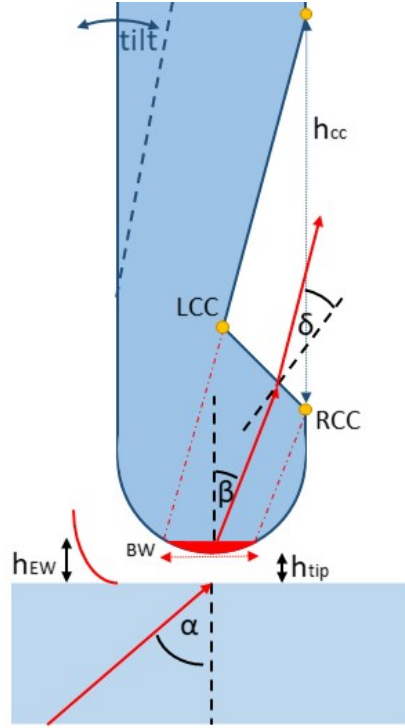


FIGURE 5.11. Diagram illustrating the idea behind triangular cutout scheme

built in, to account for different tilt angles of the cantilever around y-axis and range of incidence angles ( $\alpha$ ). The python code assumed that the rays entering the cantilever maintain a parallel beam configuration. The height of the evanescent wave  $h_{EW}$  was found using equation (2.71) and was set to the decay length of the field (calculated for the smallest incidence angle in the likely range), in order to ensure most of the light was accounted for in the design. The width of the beam  $BW$  propagating inside the probe, was found as a chord of a circle (with tip with radius  $r$ ) at a distance of  $h_{EW}$  minus the height of the tip above the surface  $h_{tip}$  from its edge. The angle of the refracted beam inside the cantilever ( $\beta$ ) was found using Snell's Law. Geometrical manipulations were used to find the right corner cutout  $RCC$  as the beam was propagated forward (at an angle ( $\beta$ ) for the largest ( $\alpha$ )) and the right utmost ray of the beam intersected with the side of the cantilever which was tilted by the largest (negative) possible tilt. Subsequently the angle of the cutout was found to ensure that the outgoing beam would not be refracted towards the probe. The cutout was then propagated towards the middle of the probe, whilst the height of the cutout  $h_c$  was adjusted accordingly.

From the simulation study of the effect of a triangular cut-out on the propagating coupled beam

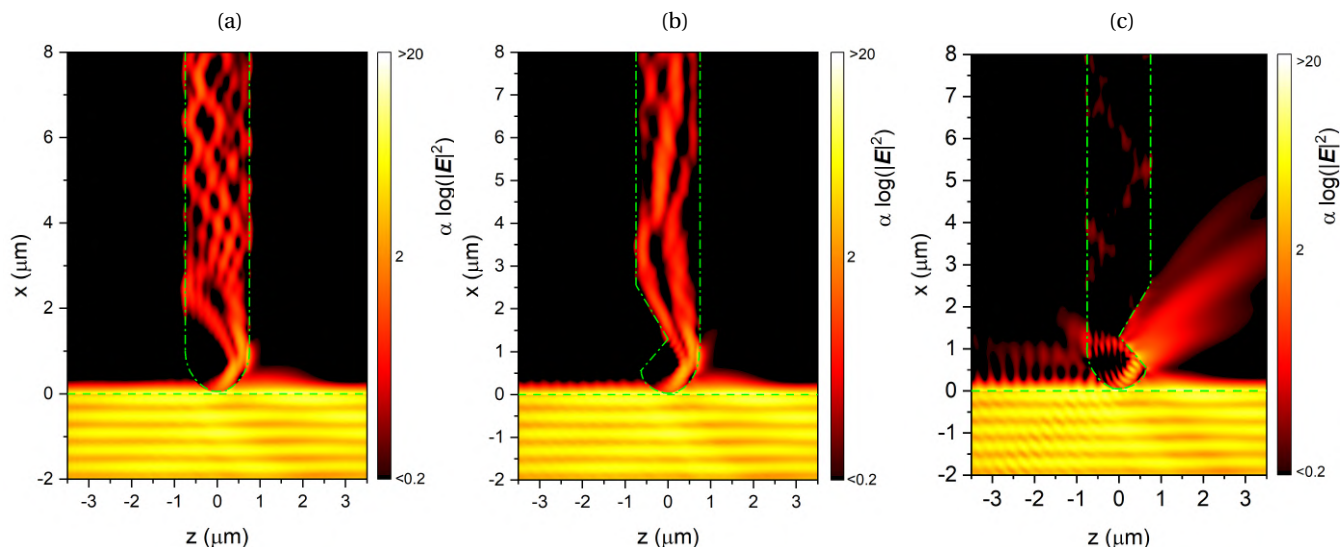


FIGURE 5.12. Simulation results for the Triangular Cutout Scheme. **(a)** Cantilever with no triangular cutout. **(b)** Cantilever with a triangular cutout located on the left (cutout missed by the coupled beam). **(c)** Cantilever with a triangular cutout located on the right (cutout located in the prime position for the method to work). The evanescent field is generated by total internal reflection of a p-polarised Gaussian beam incident onto a glass-air interface at an angle of  $\alpha = 55^\circ$ , propagating in  $xz$ -plane with a positive  $k_z$  component (left to right).

(figure 1.12), it seems clear that a one-sided triangular cutout configuration allows to test the coupling hypothesis. Such cantilever should behave like a non-modified cantilever at orientation 'C' (see figure 5.12b), but when positioned in orientation 'A' (see figure 5.12c) it should significantly reduce bending if the bias bending is caused by the light that is travelling inside the probe.

### 5.3.2 2 Holes scheme

The 2-Holes scheme has been loosely inspired by the photonic crystal filters, which work by confining the geometry of the waveguide to select the desired frequencies [23–25]. The cantilevers used in LMFM are not conventional waveguides, they do however have light travelling through them, and so the possibility of refracting and scattering the light out was investigated. The diameter of the holes relative to the width of the cantilevers is a key variables to stop the propagating light. Unfortunately, the diameter of the hole is limited by considerations of structural integrity of the silicon nitride cantilever.

The 2 holes scheme was optimised using 2D DGTD simulations as the system does not depend

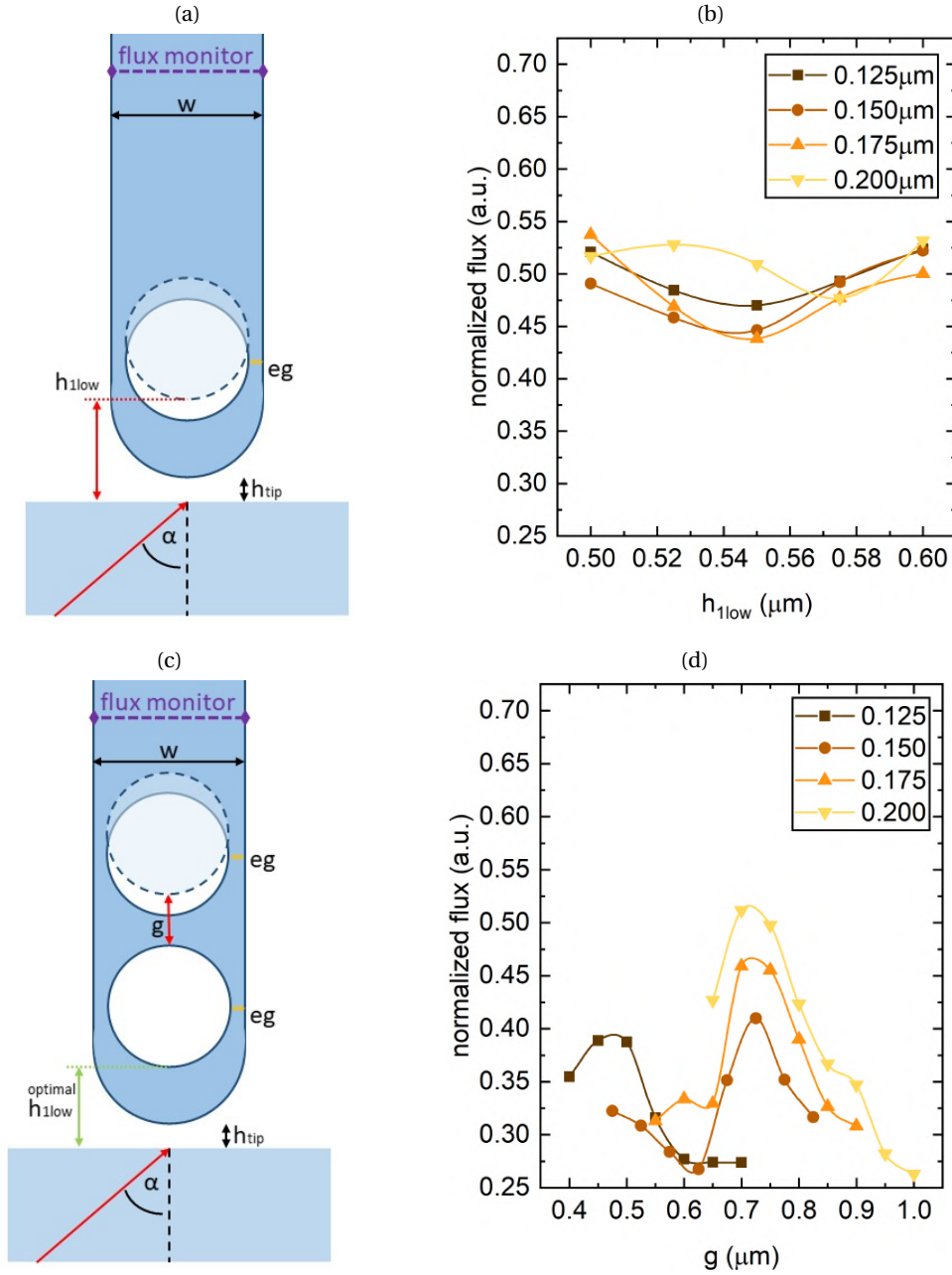


FIGURE 5.13. 2 holes scheme optimisation. (a),(c) Diagram illustrating the procedure of the optimisation. (b),(d) FDTD results for the scheme optimisation. Presented are the result of flux reduction for a 1.55  $\mu\text{m}$  wide cantilever. The flux is normalised against an unmodified probe.

on features in y-dimension, apart from the thickness of the cantilever. The simulation investigated different positions and sizes of the holes for a variety of cantilever widths a provided by scanning electron images. A set of corresponding simulations were performed in 2D and 3D to ensure that

that it was correct to disregard the y-dimension. Indeed, the simulations differed only by a linear factor and the same trend was clear in both data sets.

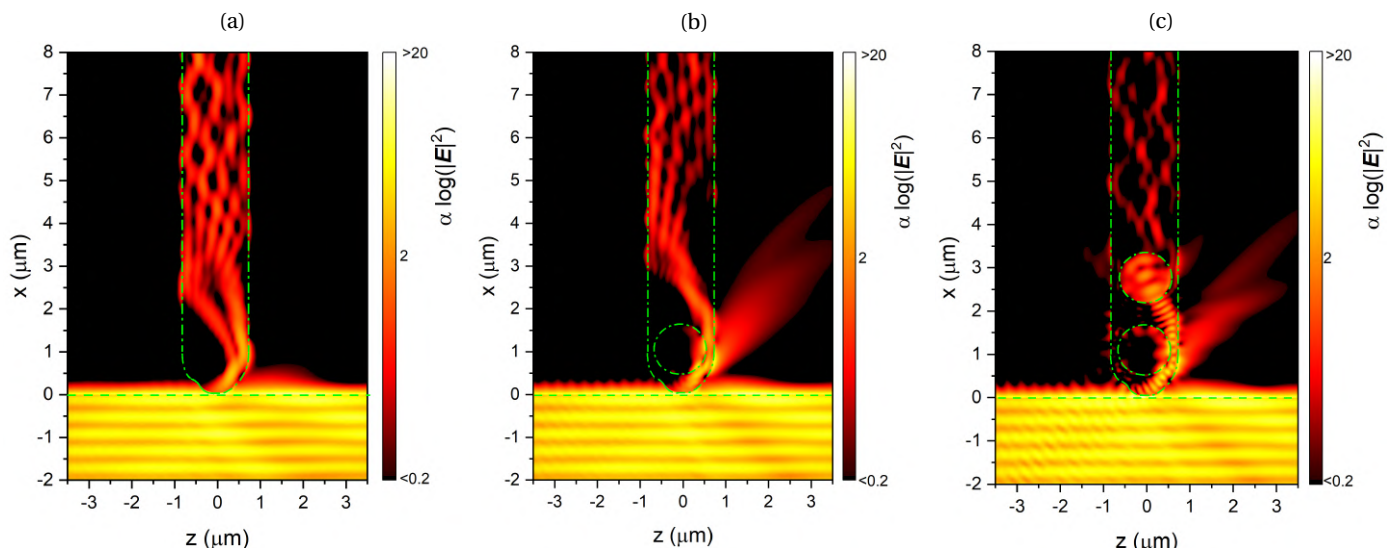


FIGURE 5.14. Simulation results for the 2-Holes Scheme. **(a)** Cantilever (shape of which is based on SEM image in figure 5.15d) with no holes, **(b)** with a first hole (scattering some of the light) and **(c)** with two holes, scattering most of the light inside this cantilever. The evanescent field is generated by total internal reflection of a p-polarised Gaussian beam incident onto a glass-air interface at an angle of  $\alpha = 55^\circ$ , propagating in xz-plane with a positive  $k_z$  component (left to right).

In a simulation, a power flux monitor was positioned  $4\mu\text{m}$  away from the surface and it recorded the total flux which passed through the cantilever.  $R$  = The flux was calculated as a fraction of the total flux input in the simulation. The simulations were 120fs long, to ensure that the whole light pulse ( $<5\text{fs}$ ) had enough time to travel through the flux monitor. Figure 5.13 shows the 2-Holes scheme optimisation process. The optimisation was done for different cantilever widths, which were determined prior by taking SEM images of cantilever arrays. In this way we could use these simulations to etch these pattern on real cantilevers. For each given width, the position of the first hole  $h_{low}$  (figure 5.13a) was first determined for 4 different radii (defined with respect to how big was the edge gap  $eg$  that remained ( $eg = (w - 2r)/2$ ); see figure 5.13a). Once the optimum height for the first hole (for a given width and hole radius) was found, a second hole of the same radius was added above and the gap  $g$  between the holes was varied (see figure 5.13c). The results for each of the 2 stages of optimization are presented in figures 5.13b and 5.13d where the flux through the monitor,



for each iteration, was normalised against the flux through the monitor of a cantilever without any modifications.

Figure 5.14 contains results of 3D FDTD simulations visualising the effect of adding 2-holes according to the design described in figure 5.13.

### 5.3.3 Manufacturing cantilever with modified end using focused ion beam

The Helios NanoLab 600 DualBeam FIB from Thermo Fisher Scientific was used to implement the designs suggested in the previous section on real Si<sub>3</sub>N<sub>4</sub> cantilevers. The Focused Ion Beam (FIB) used in this work utilises a beam of highly focused gallium ions to sputter atoms from the sample surface, enabling milling and etching nanostructures.

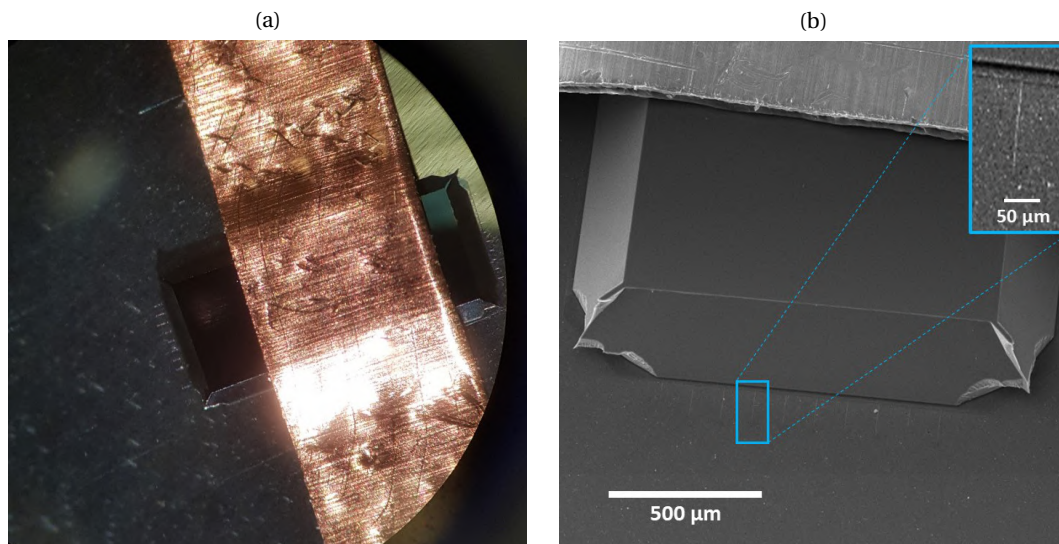


FIGURE 5.15. **(a)** Image from an optical microscope of a cantilever chip mounted flat on a polished aluminium stub, prepared for FIB. **(b)** SEM image of the same chip, confirming, the cantilevers are mounted flat on the surface.

Mounting of the cantilever chips for modifications in FIB was not trivial. Usually samples are mounted on the SEM specimen stubs using highly conductive carbon adhesive tabs. Due to their very low stiffness, the cantilevers had to be placed flat on the surface. However if an adhesive surface was used, it would make it impossible to take the cantilevers of the stub after the modifications were completed. Hence they had to be mounted directly onto the aluminium stub. For the success of the etching process it was essential for the cantilevers to make a good contact with the aluminium



surface. Firstly, it prevented the cantilever from freely oscillating, ensuring the precision of etching. Secondly, lack of contact would lead to a high amount of charge buildup, causing the cantilevers to fold. To ensure sufficient contact the microcantilevers, the stubs had to be polished. The chip was then placed down at an angle onto the stub with its longer edge first and then gently lowered. Any movement along the direction of the long edge of the chip could potentially result in damaging the cantilevers. The chip was finally secured in place with carbon and copper adhesive tape (see figure 5.15a). To ensure the chips were mounted correctly, SEM images of the whole chip as well as of each individual cantilever were taken using Tescan Vega3 (see figure 5.15b) before etching.

The etching was performed at relatively low current ion beam. In this way it was possible to prevent etching into the aluminium substrate that could have caused redeposition of the aluminium on the face of the cantilevers. After a few attempts, both the 2-holes scheme and the triangular cutout design were successfully implemented and can be seen in figures 5.16a and 5.17a respectively.

#### **5.3.4 Bias bending on cantilevers with circular and triangular cut-outs**

Following the methodology described in section 5.3.3, the two designs described above were implemented and tested.

Figure 5.16 shows the results for the 2-holes scheme. The modified cantilever was positioned 30nm above the surface and was subject to p-polarised light (incident at  $55^\circ$ ). For comparison purposes, a response of a cantilever with no modifications on the same chip was also measured.

The force acting on the cantilever was measured in both 'A' and 'C' orientation. The cantilever with the 2 holes etched has a weaker response to bias bending (on average 42% of the force acting on the unmodified cantilever). As the modified and unmodified cantilevers are on a single chip, their tilt and rotations around y-axis and x-axis are assumed to be the same. The average reduction in the bias bending for the modified cantilevers is in agreement with the simulations which suggested 20% – 40% flux reduction. Variations between the two orientations (A and C) of the cantilever with holes can be explained by looking at the image in figure 5.16a which shows that the tips have an irregular semicircular shape, which would explain the difference in both of the cantilevers' response when rotated  $180^\circ$ .

Figure 5.17 shows the results for the triangular cutout design. The setup for the measurement is

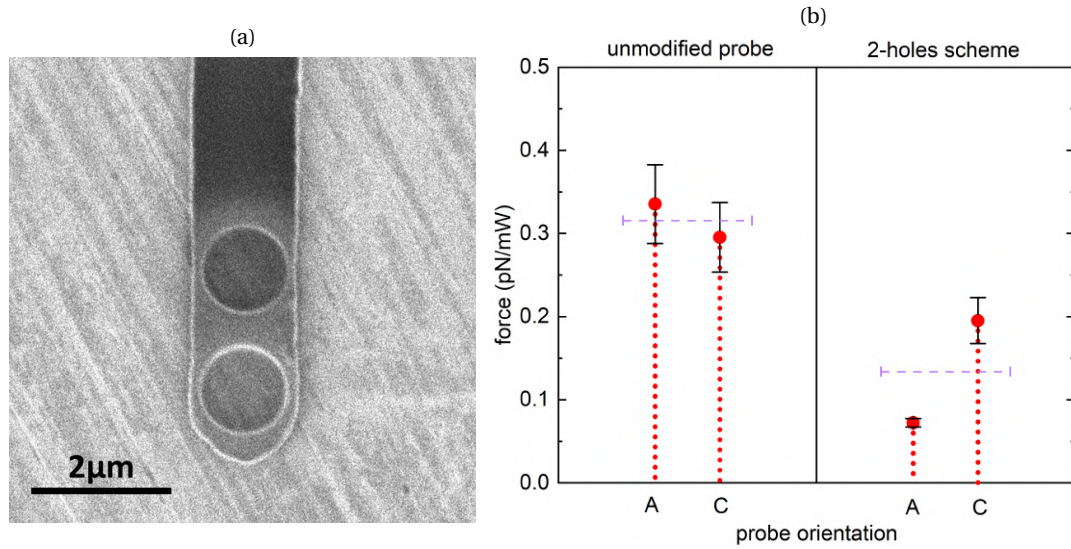


FIGURE 5.16. **(a)** SEM image of a modified cantilever according to the optimized 2 holes design **(b)** A comparison of bias bending for the unmodified probe and modified probe. An average reduction of the bias bending of 42% was observed. The difference of the bias force in the 'A' and 'C' orientations could be explained by the irregular semicircular shape of the tip

the same as above. As already mentioned, by cutting a single triangle on one side, gives the possibility to test the coupling light hypothesis in an elegant way. A simple rotation of the cantilever by 180° degrees should significantly reduce the bias bending as predicted by the simulation shown in figure 5.12 b and 5.12c respectively. Orientation 'C' corresponds to the case presented in figure 5.12b, whilst orientation 'A' to figure 5.12c. Figure 5.17b clearly confirms the simulation results with a significant reduction in bias bending should be observed for orientation 'A'. Specifically, the force measured for orientation 'A' was less than 0.2% of the force experienced by the cantilever when it was in orientation 'C'. This result combined with the prediction from the simulation not only confirms the origin of the bias bending but also suggests an elegant way to minimise its effect while maintaining the regular shape of the cantilever tip. The disadvantage of this method is the fragility of the final cantilevers and some further design optimisation is required to produce “bias-free” probes.

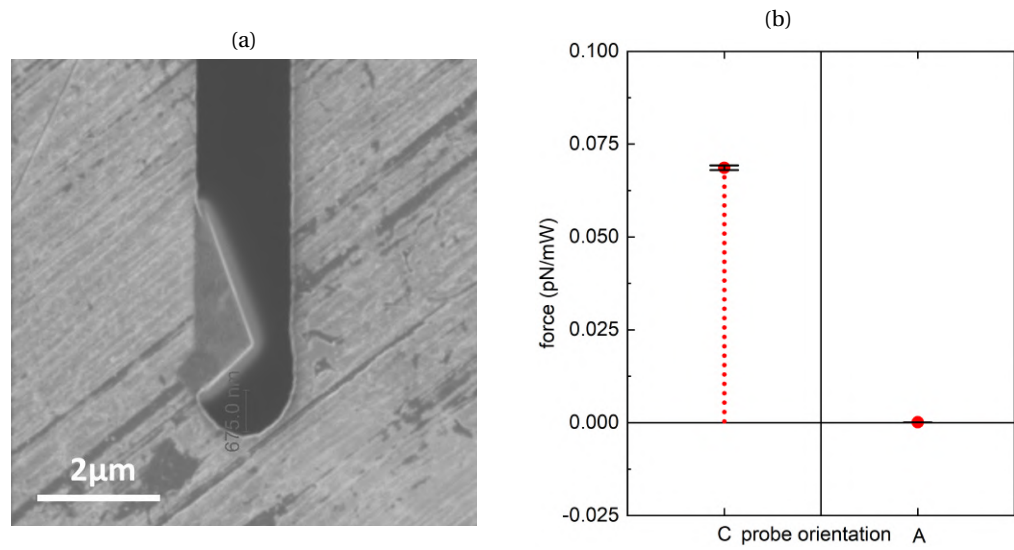


FIGURE 5.17. **(a)** SEM image of a modified cantilever according to the triangle cutout design **(b)** A comparison of bias bending experienced by the cantilever in orientations 'C' and 'A' corresponding to the simulations in 5.12b and 5.12c respectively. A clear reduction of the bias bending can be seen for cantilever in orientation 'A' which is in agreement with the coupling hypothesis and the simulation prediction.

## 5.4 Locating the bias bending along the probe

Once it is clear that the bias bending is created by light coupling within the cantilever the next step is to determine what can cause this effect. In order to narrow down the possible explanation for the bias bending, it is important to understand in which part of the cantilever, the bending is originating. Two solutions are investigated. In one case the bending is created along the length of the cantilever, in the second case the bending is limited to the base of the cantilever (due to bimetallic strip effect).

An extended FDTD simulation of the light coupling into the cantilever was performed spanning  $100\mu\text{m}$  (almost the whole length of an actual cantilevers) to investigate how far the light travels in the cantilever before it's attenuated through absorption. The results presented in figure 5.18 show that the light can travel most of the way up, though it will be significantly attenuated (nearly 2 orders of magnitude) by the time it reaches the base of the cantilever. The curvature of the tip causes a divergence of the coupled light leading to mode dispersion and subsequent attenuation of light inside the cantilever.

However to discriminate where the bending is taking place, an experiment which could stop the light travelling halfway up the cantilever was needed. For that purpose, the 2 hole design was employed, with the only difference that the holes were not etched as previously at the tip but rather in the middle of the cantilever. Whilst cutting the holes, the structural integrity of the cantilever was weakened, creating a hinge. This unexpected development was not necessarily a bad outcome. Contrary to most of the experiments, the knowledge of the displacement of

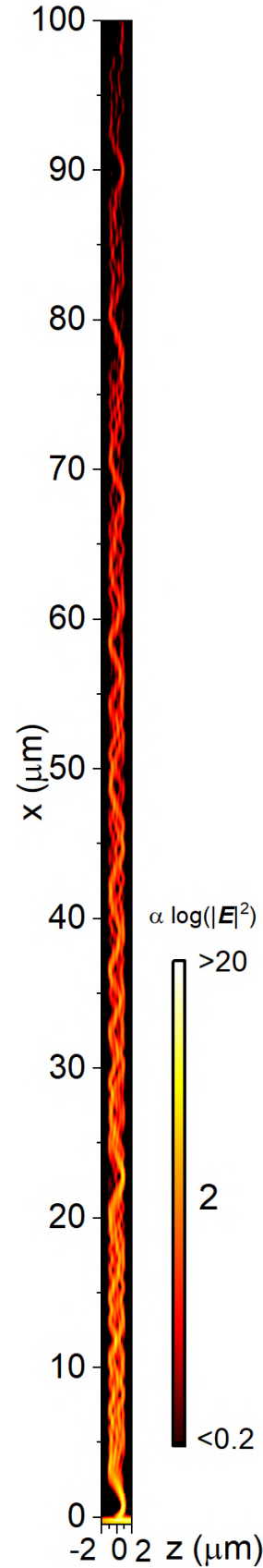


FIGURE 5.18. Simulation of light propagating inside the cantilever along the whole length

the tip was not necessarily sufficient, the movement of the whole probe needed to be monitored. That was accomplished using the CMOS camera similarly to section 5.1.1. One of the three possible outcomes was expected. First possibility was that no displacement would be recorded using the QPD, indicating that in fact the bias bending originates at the base of the cantilever. Second and third possible outcomes both would register deflection of the probe using QPD. However in one case the whole cantilever would move and in the other, only the part below the 2 holes. The latter would indicate that the bending originates along the cantilever, with the former being inconclusive suggesting that the 2 holes which were randomly positioned, did not stop sufficient amount of the light from travelling further and so both explanations would still be valid.

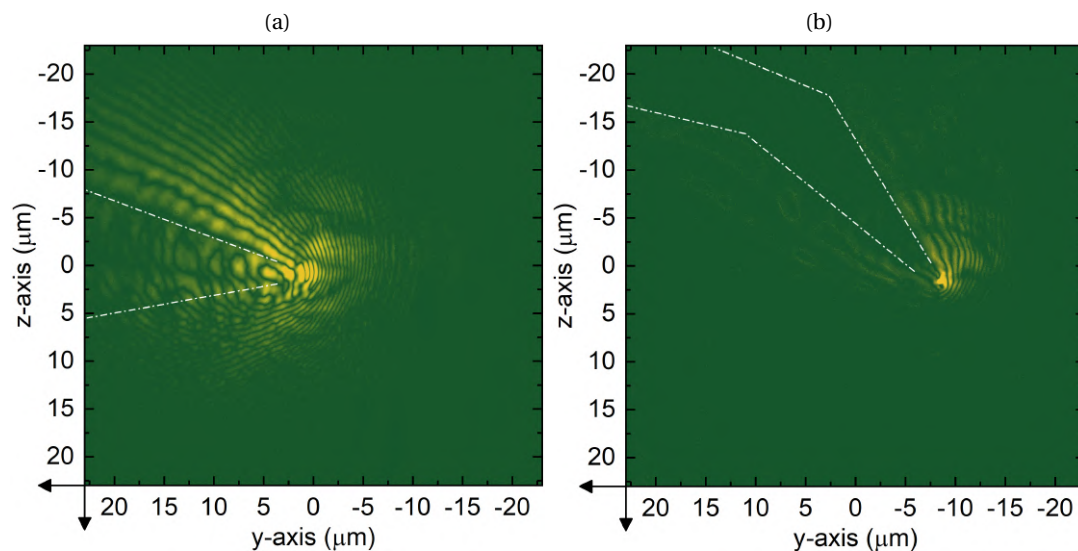


FIGURE 5.19. Entire cantilever movement observations using CMOS camera. Two bright-field images of **(a)** an unmodified probe, and **(b)** probe with 2 holes etched halfway up were taken with the driving laser 'on' and 'off'; and subsequently subtracted. The obtained difference for each pixel, highlights which part of the probe moved, showing that for the modified cantilever only the section below the modifications experienced the bias bending.

Figure 5.19a was created by subtracting 2 bright field images from CMOS camera. The position was recorded twice, with the driving laser 'on' and 'off'. Bright-field images were taken for an unmodified probe (in figure 5.19a), and a probe with 2 holes etched halfway up (in figure 5.19b), and subsequently subtracted to highlight the difference in position. By looking at these, we can determine which part of the probe moved, showing that for the modified cantilever only the section

below the modifications experienced the bias bending.

## 5.5 Discussion of the results

The unmodified cantilever chip was examined using the Tescan Vega3 SEM with an EDX module to check for any potential impurities or contamination from the micro-fabrication process [26]. It is not uncommon for the KOH wet etching used in the cantilevers manufacturing process [1] to introduce contamination by heavy metals such as nickel or copper which might diffuse into the material. As copper has a high thermal expansion coefficient, a copper contamination on one face of the cantilevers could explain the bias bending observed. It is also possible that a very thin layer of silicon remains unetched, on the back side of the cantilever.

Presented in figure 5.20 is the EDX spectrum of the silicon nitride probes. As expected, strong peaks corresponding to Silicon and Nitrogen were identified. In addition, a small signal corresponding to Oxygen was also observed and it is likely coming from very thin oxide layers formed on  $Si_3N_4$  after prolonged exposure to air. No heavier metals were detected so the bias bending cannot be caused by the contamination. Unfortunately, EDX does not provide precise enough readings to make any quantitative statements about the ratio of silicon to nitrogen.

### 5.5.1 Transfer of momentum - surface roughness or curvature of cantilever leading to recoil force

Transfer of momentum of the light coupled inside of the cantilever was considered as a possible origin of the bias bending. If the cantilever was slightly bent, light coupled within the cantilever will experience a change in direction resulting in a net momentum transfer. A qualitative assessment of cantilever curvature was performed using an optical microscope. When illuminated at an appropriate angle the entire silicon nitride layer acts as a mirror making it possible to compare the orientation of the cantilevers with respect to the orientation of the supporting silicon chip. In other words, if the cantilevers were straight, they would reflect the light at the same angle as the chip (see figure 5.21). However, if the cantilevers were curved, only the section closest to the base of the cantilever would reflect the light at the same angle of the chip. By changing the angle of the chip around the

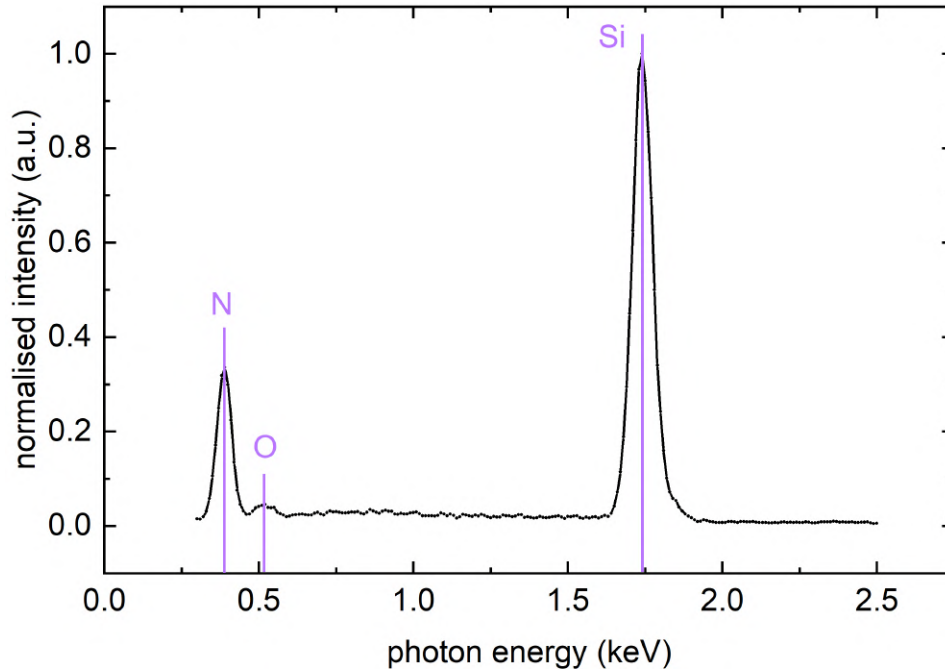


FIGURE 5.20. EDX spectrum of silicon nitride cantilevers. Peaks corresponding to nitrogen, oxygen and silicon were identified. No other elements were detected

pivot, it is possible to evaluate whether the curvature was negative or positive. Using this procedure, 2 chips with opposite curvatures were identified and their response to evanescent field evaluated. No difference in the direction of the bias bending was observed, meaning that the momentum of light travelling within the cantilever is not responsible for the bending.

It is well known, that the surface roughness of a waveguide will result in loss of light due to scattering [27]. It has also been reported that the surface roughness of amorphous  $\text{Si}_3\text{N}_4$  increases with the deposition thickness [28]. For this reason the surface roughness of both sides of the silicon nitride layer was measured. A higher roughness of the 'front' side could lead to the net scattering from that side and causing the cantilever to always bend towards the silicon chip. However, as seen in figure 5.22, the 'back' side of the silicon nitride layer has a slightly higher surface roughness. These results, which were obtained using AFM Dimension3100, need to be treated with caution as the surface area measured is significantly smaller than that of the cantilever area and generalizations made based on such a small sample size might be misleading. Nevertheless a big difference in surface roughness would need to be present for this explanation to be valid.

Ultimately, the effect of cantilever curvature and roughness can be ruled out if we consider the

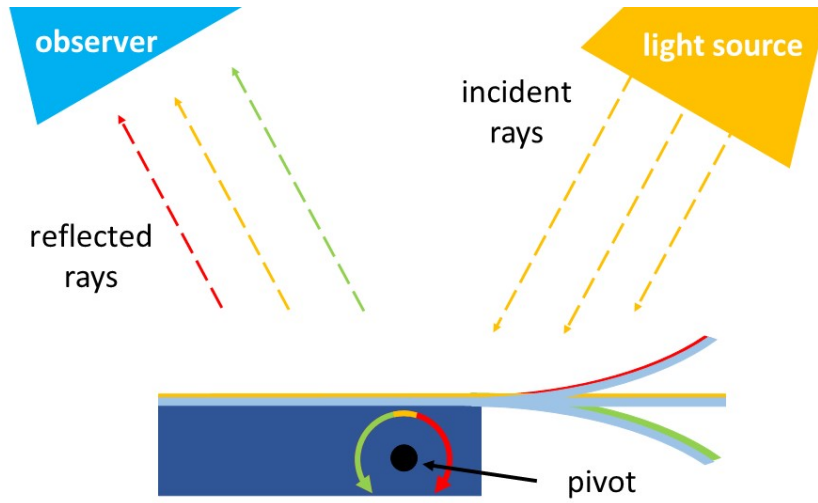


FIGURE 5.21. Diagram illustrating a method for qualitative estimate of curvature of the cantilevers with respect to the chip

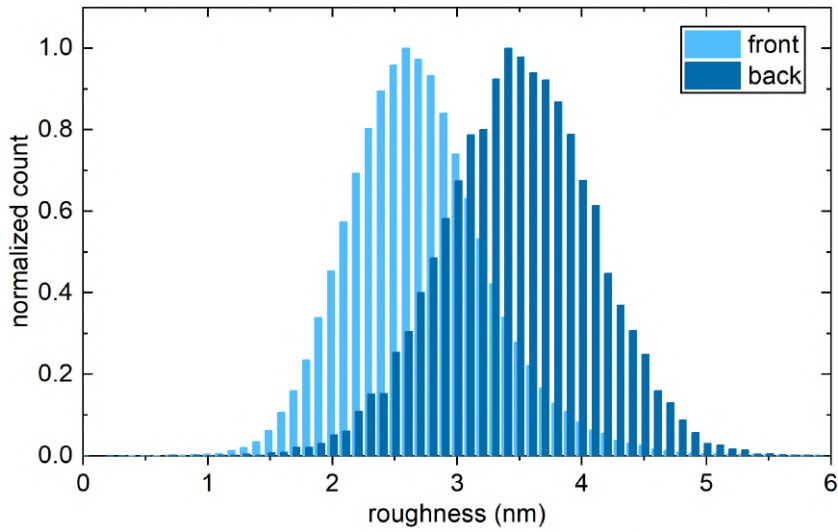


FIGURE 5.22. Comparison of surface roughness of 2 sides of the cantilever, measurement performed with AFM

amount of photons which couple inside the cantilever. According to the simulations presented in section 5.3.4, only 0.9% of total power couples inside the cantilever (which it is, in itself, an overestimate, as the actual beam diameter is around twice the diameter of the beam simulated). During experiments, the estimated power of the input laser incident on the cover slip was around 7.5mW. Energy of a single photon of  $\lambda = 660\text{nm}$  is about  $3 \times 10^{-19}\text{J}$ . The above equates to about  $5 \times 10^{13}$  photons per second inside the cantilever. Even in the ideal circumstances, the force associated



with the transfer of momentum from the coupled laser within the cantilever would be around 0.05pN which is 2 orders of magnitude lower than the effect observed.

### 5.5.2 Thermal gradient

A thin layer of silicon left during the micro-fabrication process could produce a thermal gradient effect. The  $\text{Si}_3\text{N}_4$  is transparent at 660nm, whilst the Si has an absorption coefficient of  $2.58 \times 10^5 \text{m}^{-1}$  [29]. If the silicon layer were to absorb light and subsequently experience an increased temperature, that could result in a thermal gradient across the thickness of the cantilever. The thermal diffusion length  $l_{diff}$  for silicon nitride (assuming 1Hz on-off illumination) is given by [30]

$$l_{diff} = \sqrt{\frac{4\kappa_{th}\tau_{diff}}{\rho c_{sh}}} \quad (5.4)$$

where  $c_{sh} \approx 700 \text{J/kgK}$  is specific heat,  $\kappa_{th} \approx 15 \text{W/mK}$  is the thermal conductivity,  $\tau_{diff}$  is the time and  $\rho \approx 3000 \text{kg/m}^3$  is the density (values for  $\text{Si}_3\text{N}_4$  from [30]). Resulting thermal diffusion length is  $l_{diff} \approx 10^{-3} \text{m}$  which is 4 orders of magnitude larger than the thickness of the cantilever suggesting that the temperature gradient along the thickness of the cantilever is unlikely to be responsible for the observed bias bending.

### 5.5.3 photostriction and thermal expansion - volumetric change effect

The most promising theory to explain the bias bending is the mechanical effect due to a volumetric change experienced by the silicon nitride probe with a very thin layer of residual silicon on the back face (<5nm). The change in volume of the 2 layers ( $\text{Si}_3\text{N}_4$  and Si) would lead to a sideways deflection given by [12]

$$d_b = \frac{Y_r t_r (1 + t_r)^2}{Y_r^2 t_r^4 + 4Y_r t_r^3 + 6Y_r t_r^2 + 4Y_r t_r + 1} \frac{l^2}{t_s} \left( \left( \frac{\Delta V}{V} \right)_1 - \left( \frac{\Delta V}{V} \right)_2 \right) \quad (5.5)$$

where Y denotes Young's modulus where  $Y_r = Y_2 / Y_1$ , t is thickness,  $t_r = t_2 / t_1$  and  $t_s = t_1 + t_2$ , l is the length and  $\Delta V / V$  is fractional volume change (where subscripts 1,2 refer to silicon nitride and silicon layers respectively). The literature value of Young's modulus for silicon nitride is  $Y_1 \approx 290 \text{GPa}$  and for silicon is  $Y_2 \approx 179 \text{GPa}$  [30].

Two effects can contribute to the volumetric change. First one being the thermal expansion given by

$$\left(\frac{\Delta V}{V}\right)_t = 3\alpha_{tec}\Delta T \quad (5.6)$$

where  $\alpha_{tec}$  is the thermal expansion coefficient ( $\alpha_{tec1} \simeq 2.75 \times 10^{-6} \text{K}^{-1}$  for  $\text{Si}_3\text{N}_4$  [31] and  $\alpha_{tec2} \simeq 2.6 \times 10^{-6} \text{K}^{-1}$  for Si [32]). Assuming an increase in temperature of  $\Delta = 2\text{K}$  and the silicon layer thickness of  $t \simeq 2\text{nm}$ ; the deflection due to thermal expansion would be approximately  $\sim 1.5\text{nm}$  which would correspond to roughly  $\approx 0.05\text{pN}$  for the cantilevers used. This effect, on its own, is approximately 2 orders of magnitude lower than the observed bias bending.

The second effect contributing to the volumetric change is the photostriction [33] which causes expansion or contraction of material under illumination (it has been documented for silicon, but there is no data yet for silicon nitride). Photostriction is an effect similar to electrostriction and magnetostriction, which causes the change in the crystal lattice by exciting electron-hole pairs to create free charge carriers and is given by

$$\left(\frac{\Delta V}{V}\right)_p = \frac{dE}{dP}\Delta n \quad (5.7)$$

where  $dE/dP$  is the pressure dependence on band gap energy ( $dE/dP \simeq -2.9 \times 10^{-30} \text{m}^3$  [34]) and  $n$  is the number density of excess charge carriers given by

$$\Delta n = \eta_q \frac{\lambda}{hc} \frac{\tau_L}{lwt} W_{abs} \quad (5.8)$$

where  $\eta_q$  is the quantum efficiency ( $\eta_q \simeq 1$  [33]),  $\lambda$  the incident light wavelength,  $\tau_L$  is the lifetime of free charge carriers ( $\tau_L \simeq 2\mu\text{s}$ ),  $w$  is the width and  $W_{abs}$  is the absorbed power. It is important to stress that because of the negative sign of the pressure dependence of the silicon, the volumetric change will cause a deflection in the direction consistent with the bias bending (back of the chip). Depending on the assumptions with regard to absorption efficiency and quantum efficiency, the resulting deflection is around  $\simeq 200\text{nm}$  which corresponds to  $\simeq 4\text{pN}$ . That is in fact on the order of magnitude of the bias bending observed, making this effect the most promising hypothesis to explain the origin of the bias bending.

## 5.6 Bibliography

- [1] J. Vicary, A. Ulcinas, J. Hörber, and M. Antognozzi, “Micro-fabricated mechanical sensors for lateral molecular-force microscopy,” *Ultramicroscopy*, vol. 111, pp. 1547–1552, Nov. 2011.
- [2] M. Antognozzi, C. R. Bermingham, R. L. Harniman, S. Simpson, J. Senior, R. Hayward, H. Hoerber, M. R. Dennis, A. Y. Bekshaev, K. Y. Bliokh, and F. Nori, “Direct measurements of the extraordinary optical momentum and transverse spin-dependent force using a nano-cantilever,” *Nature Physics*, vol. 12, pp. 731–735, Aug. 2016.
- [3] C. R. Bermingham, “PhD Thesis - Measurement of pico/femto-Newton scale forces using the Lateral Molecular Force Microscope,” *University of Bristol*, 2016.
- [4] W. K. Szeremeta, “MSci Thesis - Investigating Optical Forces in an Evanescent Field, Including the Extraordinary Spin Momentum,” *University of Bristol*, 2016.
- [5] S. Kawata and T. Sugiura, “Movement of micrometer-sized particles in the evanescent field of a laser beam,” *Optics Letters*, vol. 17, p. 772, June 1992.
- [6] S. Kawata and T. Tani, “Optically driven Mie particles in an evanescent field along a channeled waveguide,” *Optics Letters*, vol. 21, p. 1768, Nov. 1996.
- [7] P. B. Conibear and C. R. Bagshaw, “A comparison of optical geometries for combined flash photolysis and total internal reflection fluorescence microscopy,” *Journal of Microscopy*, vol. 200, pp. 218–229, Dec. 2000.
- [8] M. Brunstein, M. Teremetz, K. Hérault, C. Tourain, and M. Oheim, “Eliminating Unwanted Far-Field Excitation in Objective-Type TIRF. Part I. Identifying Sources of Nonevanescent Excitation Light,” *Biophysical Journal*, vol. 106, pp. 1020–1032, Mar. 2014.
- [9] M. Brunstein, K. Hérault, and M. Oheim, “Eliminating Unwanted Far-Field Excitation in Objective-Type TIRF. Part II. Combined Evanescent-Wave Excitation and Supercritical-Angle Fluorescence Detection Improves Optical Sectioning,” *Biophysical Journal*, vol. 106, pp. 1044–1056, Mar. 2014.

- [10] A. L. Mattheyses and D. Axelrod, "Direct measurement of the evanescent field profile produced by objective-based total internal reflection fluorescence," *Journal of Biomedical Optics*, vol. 11, no. 1, p. 014006, 2006.
- [11] W. P. Ambrose, P. M. Goodwin, and J. P. Nolan, "Single-molecule detection with total internal reflection excitation: Comparing signal-to-background and total signals in different geometries," *Cytometry*, vol. 36, pp. 224–231, 1999.
- [12] C. Jeppesen, K. Molhave, and A. Kristensen, "Competition between the thermal gradient and the bimorph effect in locally heated MEMS actuators," *Journal of Micromechanics and Microengineering*, vol. 19, p. 015008, Jan. 2009.
- [13] J. Hesthaven and T. Warburton, "Nodal High-Order Methods on Unstructured Grids," *Journal of Computational Physics*, vol. 181, pp. 186–221, Sept. 2002.
- [14] Kane Yee, "Numerical solution of initial boundary value problems involving maxwell's equations in isotropic media," *IEEE Transactions on Antennas and Propagation*, vol. 14, pp. 302–307, May 1966.
- [15] P. Leuchtman, C. Fumeaux, and D. Baumann, "Comparison of errors and stability in FDTD and FVTD," *Advances in Radio Science*, vol. 1, pp. 87–92, May 2003.
- [16] K. Busch, M. König, and J. Niegemann, "Discontinuous Galerkin methods in nanophotonics," *Laser & Photonics Reviews*, vol. 5, pp. 773–809, Nov. 2011.
- [17] J. Niegemann, W. Pernice, and K. Busch, "Simulation of optical resonators using DGTD and FDTD," *Journal of Optics A: Pure and Applied Optics*, vol. 11, p. 114015, Nov. 2009.
- [18] S. Descombes, C. Durochat, S. Lanteri, L. Moya, C. Scheid, and J. Viquerat, "Recent advances on a DGTD method for time-domain electromagnetics," *Photonics and Nanostructures - Fundamentals and Applications*, vol. 11, pp. 291–302, Nov. 2013.
- [19] F. L. McCrackin, E. Passaglia, R. R. Stromberg, and H. L. Steinberg, "Measurement of the thickness and refractive index of very thin films and the optical properties of surfaces by ellipsometry,"

- Journal of Research of the National Bureau of Standards Section A: Physics and Chemistry*, vol. 67A, p. 363, July 1963.
- [20] H. Li, X. Dong, E. Li, Z. Liu, and Y. Bai, “Highly compact 2×2 multimode interference coupler in silicon photonic nanowires for array waveguide grating demodulation integration microsystem,” *Optics & Laser Technology*, vol. 47, pp. 366–371, Apr. 2013.
- [21] K. Cooney and F. H. Peters, “Analysis of multimode interferometers,” *Optics Express*, vol. 24, p. 22481, Oct. 2016.
- [22] J. Wang, N. Ning, Z. Wang, G. Li, J. Xu, and Y. Lu, “Compact general interference hybrid-plasmonic multimode interferometers used for optical hybrid,” *Applied Optics*, vol. 58, p. 5320, July 2019.
- [23] S. Feng, Z. Qu, M. Lv, X. Chen, Y. Wang, and W. Wang, “Controlling the filtering characteristics of the two-dimensional silicon-based photonic crystal with elliptic air holes,” *Optik*, vol. 124, pp. 1865–1868, July 2013.
- [24] H. Fahs and S. Lanteri, “A high-order non-conforming discontinuous Galerkin method for time-domain electromagnetics,” *Journal of Computational and Applied Mathematics*, vol. 234, pp. 1088–1096, June 2010.
- [25] T. Zhang, J. Sun, Y. Yang, and Z. Li, “Photonic crystal filter based on defect mode and waveguide mode symmetry matching,” *Optics Communications*, vol. 428, pp. 53–56, Dec. 2018.
- [26] D. Sinha, “Nickel Contamination from Caustic Etching of Silicon Wafers,” *ECS Journal of Solid State Science and Technology*, vol. 7, no. 5, pp. N55–N58, 2018.
- [27] K. K. Lee, D. R. Lim, H.-C. Luan, A. Agarwal, J. Foresi, and L. C. Kimerling, “Effect of size and roughness on light transmission in a SiO/SiO<sub>2</sub> waveguide: Experiments and model,” *Applied Physics Letters*, vol. 77, no. 11, pp. 1617–1619, 2000.
- [28] D. M. Tanenbaum, A. L. Laracuente, and A. Gallagher, “Surface roughening during plasma-enhanced chemical-vapor deposition of hydrogenated amorphous silicon on crystal silicon substrates,” *Physical Review B*, vol. 56, pp. 4243–4250, Aug. 1997.

- [29] M. A. Green, "Self-consistent optical parameters of intrinsic silicon at 300K including temperature coefficients," *Solar Energy Materials and Solar Cells*, vol. 92, pp. 1305–1310, Nov. 2008.
- [30] B. Ilic, S. Krylov, K. Aubin, R. Reichenbach, and H. G. Craighead, "Optical excitation of nanoelectromechanical oscillators," *Applied Physics Letters*, vol. 86, p. 193114, May 2005.
- [31] M. Fukuhara, K. Fukazawa, and A. Fukawa, "Physical properties and cutting performance of silicon nitride ceramic," *Wear*, vol. 102, pp. 195–210, Apr. 1985.
- [32] V. Chenniappan, G. A. Umana-Membreno, K. K. M. B. D. Silva, M. Martyniuk, A. Keating, J. M. Dell, and L. Faraone, "Photostriction actuation of silicon-germanium bilayer cantilevers," *Journal of Applied Physics*, vol. 125, p. 125106, Mar. 2019.
- [33] P. G. Datskos, S. Rajic, and I. Datskou, "Photoinduced and thermal stress in silicon microcantilevers," *Applied Physics Letters*, vol. 73, pp. 2319–2321, Oct. 1998.
- [34] N. Inui, "Charge Density Dependence of Photoinduced Stress in Semiconductors," *Japanese Journal of Applied Physics*, vol. 45, pp. 1675–1679, Mar. 2006.



## DIRECT MEASUREMENTS OF OPTICAL FORCES IN THE EVANESCENT FIELDS

The magnitude of optical forces acting on nanoparticles in evanescent fields is in the piconewton range, most of the reported experiments measuring these forces were performed using microspheres in diffusing liquid or optical tweezers thus far, with the exception of the work done by Kohlgraf et al. [1, 2] who mapped the gradient force of the evanescent field using SPM. More recently the first direct measurement of the transverse, helicity-dependent Belinfante spin momentum was reported by Antognozzi et al. [3].

In this chapter, presented are innovative experimental methods designed to measure the longitudinal orbital momentum of an evanescent field using SPM, as well as the Belinfante spin momentum using micro-fabricated cantilevers (making use of a new, improved, experimental procedure). The theory underpinning these experiments was presented in chapter 2.

Figure 6.1 illustrates the orientation convention followed in this chapter. All the experiments were performed with cantilevers in orientation 'A', illuminated by either laser #1 or laser #2. Additionally, readers may find figure 3.2 and figure 5.1 useful.



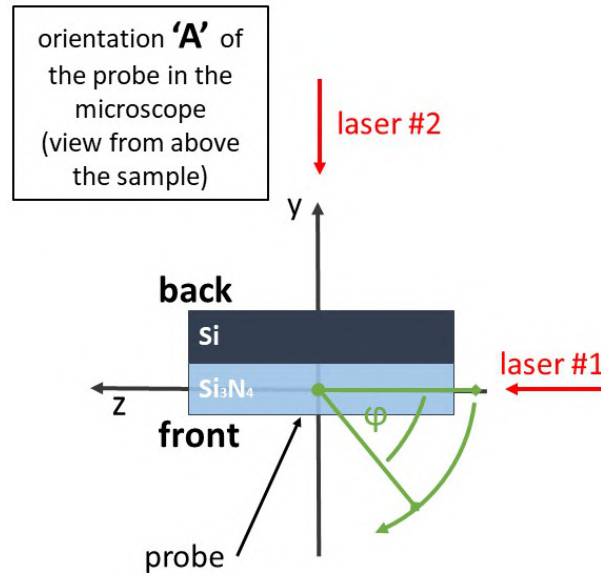


FIGURE 6.1. Diagram illustrating the cantilever orientation 'A' used throughout this chapter, as well as the direction of the propagation of the wave generated by the respective lasers. This convention is crucial for understanding the experiments presented in this chapter

## 6.1 Measuring longitudinal force associated with orbital momentum of the evanescent field

A set of 3 experiments to study longitudinal forces on dielectric particles in an evanescent field are presented in this section. First, a reproduction of one of the first experiments on longitudinal optical force imparted on a dielectric sphere by an evanescent field is reported. Followed by a set of experiments using the extra-compliant silicon nitride cantilever with a dielectric sphere attached on the tip. Finally, a glass micro-needle with a dielectric sphere is used to perform measurements on longitudinal momentum; using a probe with no inherent bias bending resulting from the interaction of the probe with evanescent field.

### 6.1.1 Optically driven Mie particles in an evanescent field

One of the first experiments on optical forces in the evanescent field was performed back in 1992 by Satoshi Kawata and Tadao Sugiura where they showed the transfer of momentum between a

Mie-sized microspheres and the evanescent field [4]. Silica and polystyrene spheres were dispersed in an aqueous solution and their motion was recorded upon evanescent field illumination. From their velocity, the authors were able to evaluate the force acting on the spheres [5].

To establish a baseline of the force communicated to a dielectric sphere in an evanescent field, we followed the experimental method presented in Kawata and Sugiura's paper.  $2\mu\text{m}$  silica beads (Bangs Lab, USA) diluted in water were injected into a microfluidic channel and observed diffusing according to standard Brownian motion diffusion. As soon as the evanescent illumination was switched on, we could observe the spheres acquire a non-zero drift velocity in the direction of the evanescent field (see results in figure 6.2).

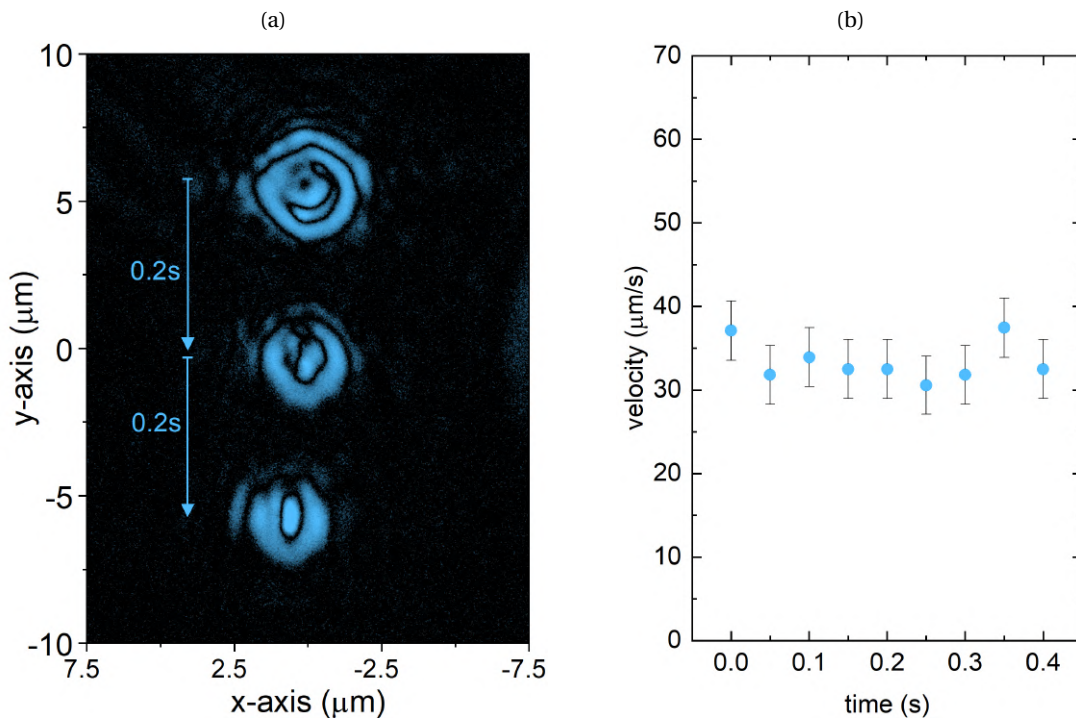


FIGURE 6.2. Measuring the force on Mie-sized spheres in an evanescent field. **(a)** Overlaid stills, from a CMOS camera, of a sphere being pushed in the direction of propagation of the evanescent field (-y direction) **(b)** Extracted sphere velocity from a time sequence recorder by the CMOS camera, which can be used to evaluate the force experienced by the sphere through the Stoke's Law.

Using brightfield illumination the position of the spheres was observed with the CMOS camera. The trajectories of movement of the spheres upon evanescent field illumination were recorded at

20fps. The Stoke's Law for the friction force is given by

$$F_r = 6\pi r \nu \eta_{H_2O} \quad (6.1)$$

and it relates the velocity  $\nu$  with which the sphere of radius  $r$  is moving within a fluid of viscosity  $\eta_{H_2O} \approx 10^{-3} \text{Pa}\cdot\text{s}$  [6] at room temperature with the frictional force it is experiencing. At equilibrium, the scattering force is matching the viscous force and it is possible to calculate the effect of the evanescent field. The spheres were observed moving in the direction of the propagation of the evanescent field with a constant velocity of  $\nu \approx 33 \pm 2 \mu\text{m/s}$ , which is equivalent to an optical force of  $0.65 \pm 0.04 \text{pN}$ . The limited precision ( $\pm 6 \text{px} \approx \pm 159 \text{nm}$ ) with which the position of the sphere could be evaluated, based on CMOS camera images, contributed to a large error in determining the velocity of the sphere through water.

As the evanescent wave decays exponentially away from the surface and the sphere is  $2 \mu\text{m}$  in diameter, most of the optical momentum will be transferred through the lower part of the sphere closest to the glass substrate. This can result in the momentum of light being transferred into the angular momentum of the sphere as well as the linear momentum of the sphere. Furthermore, one of the biggest issues of this experiment is the lack of control of the height above the sample. However, regardless of these disadvantages, the experiment provides incontrovertible evidence that the evanescent field communicates linear momentum to the fluctuating dielectric particles.

To solve the issues previously mentioned we decided to repeat these measurements using a  $2 \mu\text{m}$  bead attached at the end of a vertically oriented cantilever. In this way the sphere would not be able to rotate even if a torque was acting upon it and by adjusting the vertical position of the cantilever we could fix the sphere-surface distance within a fraction of 1 nanometre.

### 6.1.2 Attaching spheres to the SPM probes

Thanks to the advanced positioning capabilities of the new LMFM we were able to routinely attach a microsphere to the tip of a cantilever directly in the LMFM. A selection of  $2 \mu\text{m}$  (SS04002) and  $3 \mu\text{m}$  (SS05001) silica spheres from 'Bangs Laboratories, Inc' were used throughout the project. A solution of spheres in ethanol was prepared with concentrations ranging between 1:1000 and 1:10000 to ensure an appropriate dispersion of particles on the cover slip. The solutions were thoroughly

vortexed (for 45s) to avoid particle aggregation and subsequently an aliquot of  $2\mu\text{l}$  was deposited on a clean cover slip already mounted in LMFM (see section 4.1). The ethanol is used as it quickly evaporates, leaving the spheres dry on the surface. A thin layer of the Norland Optical Adhesive NOA 81 was used due to its optical properties ( $n = 1.68$ ). The viscosity of the adhesive used, is also important. As the cantilevers possess an extreme aspect-ratio, a high (low) viscosity can lead to excess (lack) of the adhesive at the actual tip of the cantilever. The UV-curing glue, enables enough time for positioning and handling, followed by curing on demand. UV-adhesive is spread thinly on the same cover slip, so that it is less likely for the cantilever to become trapped by the surface tension of the glue, and ensuring a small amount of the adhesive on the tip. The mobility of the spheres on the surface is checked using the cantilever before dipping it in the glue. If the spheres cannot be pushed by the cantilever at this stage, we found that it will be impossible to detach them from the surface once the glue has cured. We use the tip and sample motorised stages to position the tip of the cantilever either directly above the sphere or touching its sides. The Mightex BioLED 400nm is then used for curing the adhesive after an irradiation time of 30mins. Figure 6.3 contains two optical images of a cantilever taken in contact with the a  $2\mu\text{m}$  sphere before and after the UV-is cured and the bead is lifted from the surface.

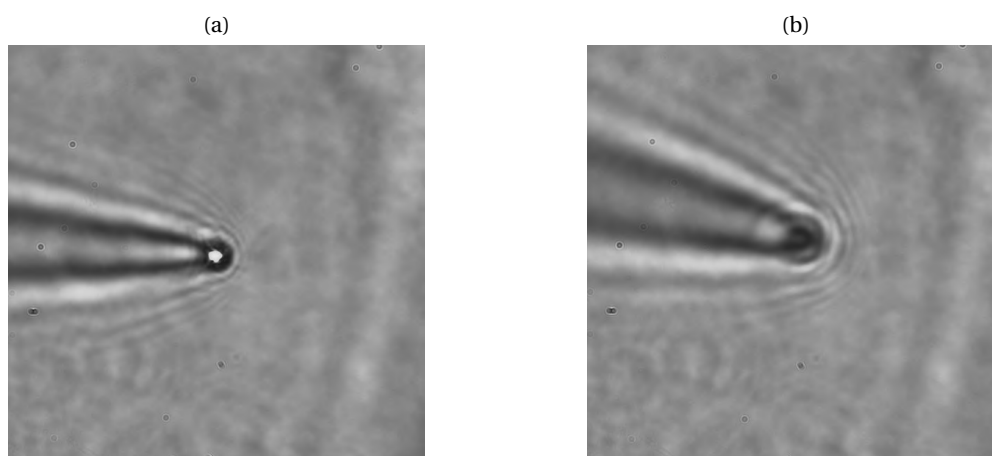


FIGURE 6.3. Images taken using the CMOS camera during the process of attaching the sphere to the silicon nitride cantilevers, **(a)** cantilever with glue on top of a silica sphere **(b)** cantilever with the sphere attached to the tip after UV glue was cured and the bead is lifted from the surface

### 6.1.3 Measuring the orbital momentum on a Mie-sized sphere using LMFM with silicon nitride probes

As mentioned in section 5.1, the presence of the bias bending, made it initially impossible to measure the longitudinal momentum of the evanescent field transferred to a sphere attached to the tip of the probe. Since then, it has been now established that the bias bending is most likely caused by the light which couples inside the cantilever. To avoid this effect it is possible to attach a sphere to the tip of the cantilever in a way that would make it almost impossible for the evanescent field to couple within the cantilever.

Simple ray optics shows that a  $2\mu\text{m}$  dielectric sphere attached on the other side of the cantilever tip with respect to the direction of propagation of the evanescent field, should stop light from coupling. Using Lumerical, three different arrangements of a  $2\mu\text{m}$  silica sphere at the end of a cantilever tip were simulated and studied how much light coupling each geometry provides. The results in figure 6.4a and 6.4b clearly show that, if the sphere is in front of the cantilever or exactly underneath, there is still substantial coupling even if the cantilever tip is much higher than the decay length of the evanescent field. Fortunately, figure 6.4c shows that when the sphere is behind the cantilever the coupling is reduced by 3 orders of magnitude.

The simulated cantilever is in the orientation equivalent to 'A' or 'C', with the laser #2 creating the evanescent field. The beam has a wavelength of  $\lambda = 561\text{nm}$  corresponding to the illumination from laser #2. The sphere is positioned  $30\text{nm}$  above the sample and an ellipsoidal drop of glue is added to mimic the likely shape of the system. With the direction of the propagation of the wave being along the  $(-y)$ -axis, it can be clearly seen, that when the sphere is attached on the positive  $y$  (left) side of the probe, the geometry of the system favours coupling (see figure 6.4a). The light also appears to couple when the tip is glued on top of the sphere with the excess of glue helping to facilitate the coupling (see figure 6.4b). Finally, when the sphere is attached on the negative  $y$  (right) side of the probe, no light coupling is produced (see figure 6.4c).

The FDTD results are confirmed by the experimentally measured forces for a set of cantilevers, with beads attached, with each of the cantilevers having a  $2\mu\text{m}$  silica sphere attached to a different side of the tip (corresponding to the configurations presented in figure 6.4).

Results presented in figure 6.5 are consistent with predictions from the simulations of different

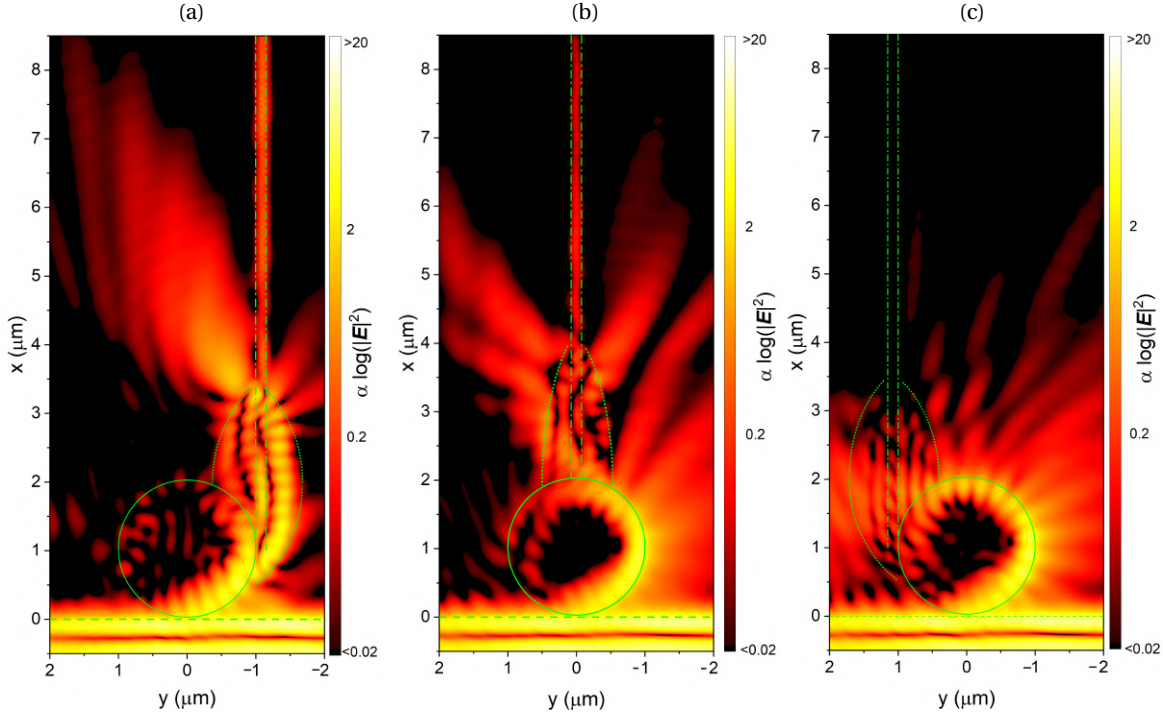
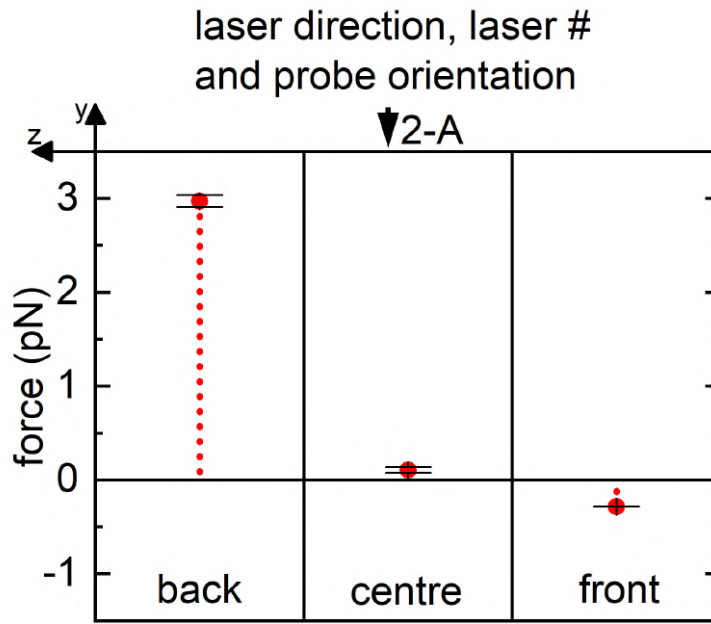


FIGURE 6.4. Simulations of the 3 different configurations of the sphere (solid line) attached to the probe (dash-dot line). The evanescent field is generated by total internal reflection of a p-polarised Gaussian beam incident onto a glass-air interface at an angle of  $\alpha = 55^\circ$ , propagating in xy-plane with a negative  $k_y$  component (left to right). Excess glue with refractive index  $n = 1.68$  is simulated (dotted line) as it was found to better reproduce the experimental setup. **(a)** the sphere is positioned on the 'incoming' side of the probe, facilitating the coupling into the probe, **(b)** the probe positioned on top of the sphere, with coupling reduced compared to **(a)**, however still present, and dependent on the size of the drop of glue. **(c)** the sphere positioned 'behind' the probe, showing that even though the light couples inside the sphere as expected, it should not couple further into the probe.

geometries in figure 6.4. When the spheres are attached either to the 'back' side or 'centre' of the tip, the results shown in figure 6.5 (left and centre column) confirm that the bias bending is still opposing the orbital momentum acting on a sphere, making it impossible to decouple the two. The result in figure 6.5 (right column), for the sphere located on the 'front' side of the cantilever (as depicted in figure 6.4C), show the probe movement in the direction of the propagation of the wave. The magnitude of the force detected is approximately a factor of 2 lower than that measured using the method based on Kawata's et al. [4, 5] papers. One possible explanation for the discrepancy is based on the fact that in the case of diffusing beads, we made the assumption, that the recorded



(b)

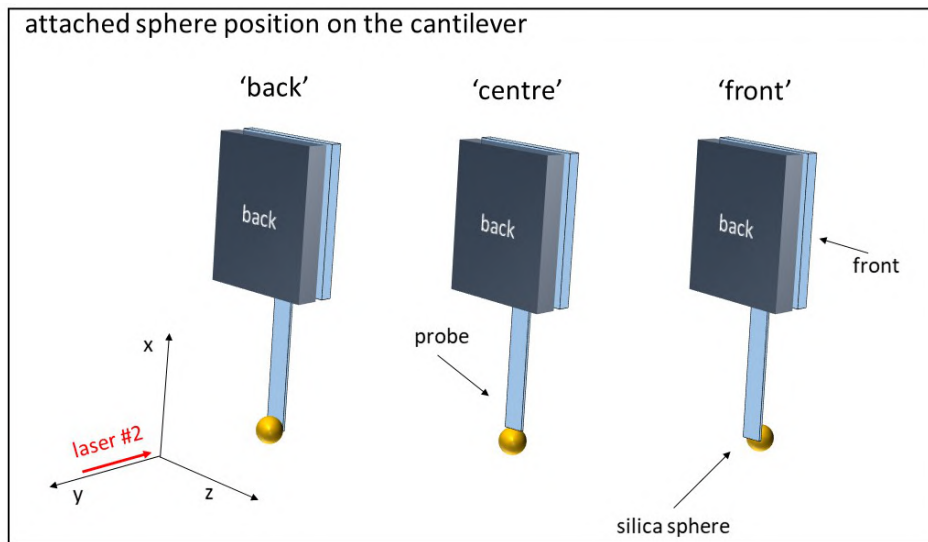


FIGURE 6.5. **(a)** Results of longitudinal momentum measurement using spheres attached to silicon nitride cantilevers. The results for **(back)**, **(centre)** and **(front)** correspond to geometries presented **(b)**

bead velocity (in figure 6.2) was also the relative velocity between the sphere and liquid. In other words, it was assumed that the liquid was stationary. However it is not unreasonable to suspect that the water itself was moving, having gained some momentum from light [7–10]. If the liquid was also moving, the estimated velocity, would be an overestimation of relative velocity, meaning that in fact, the force experienced by the sphere in water was lower than that evaluated by the Stoke's Law.

The lack of a viscous medium of a higher refractive index, suggests a more precise measurement. A further argument could be made of the fact that a small fraction of the evanescent field could still be coupling into the cantilever reducing the value of the measured

#### 6.1.4 Measuring the orbital momentum on the Mie-sized sphere using LMFM with custom made glass probes

As the silicon nitride probes used in LMFM experience the bias bending due to the light which couples inside, a probe from a different material was created, that would not manifest any photostrictive effect. In this way it was ensured that the force measured was not affected by the bias bending. The new probe had to have sufficiently low stiffness to observe sub-piconewton forces. For that reason, the standard AFM cantilevers were discarded as an option. Instead it was decided that a cylindrical probe made from pulled borosilicate glass could be a suitable candidate. For the probe to have sufficiently low transverse stiffness ( $k < 10^{-5} \text{N/m}$ ), the ratio between the length  $l$  and the radius  $r$  had to be chosen according to the following relation

$$k = \frac{3\pi r^4 Y}{4L^3} \quad (6.2)$$

where the Young's modulus for glass is  $Y = 74 \text{GPa}$ . To create a thin glass probe, 2 raw borosilicate glass rods were used. The end of one of the two rods was brought to its melting point, then attached to the end of the second rod, only to be rapidly separated, creating a thin strand of glass with radius  $r < 20 \mu\text{m}$ . The final probe used, had a radius of  $11 \mu\text{m} \pm 1 \mu\text{m}$  and a length of  $5.2 \text{cm} \pm 0.1 \text{cm}$ .

In order to fit the significantly longer probes in the LMFM, the bridge of the microscope had to be modified (i.e. where the cantilever is mounted). This modification produced a significant imbalance in the microscope head and, as a consequence, the possibility to adjust the probe tilt was limited to a few degrees, hence a malleable copper holder was introduced to compensate for lack of angular range (see figures 6.6a and 6.6b). With a significantly larger surface area of the probe, the effect of air currents is significantly amplified and so a transparent cylindrical enclosure had to be introduced to screen the probe from air movements. A  $3 \mu\text{m}$  silica sphere was attached to the end of the probe, to ensure a well defined tip (as opposed to an uneven glass interface, created by snapping the glass strand). As can be seen in figure 6.6b, the glass probe created was slightly curved. As a consequence,



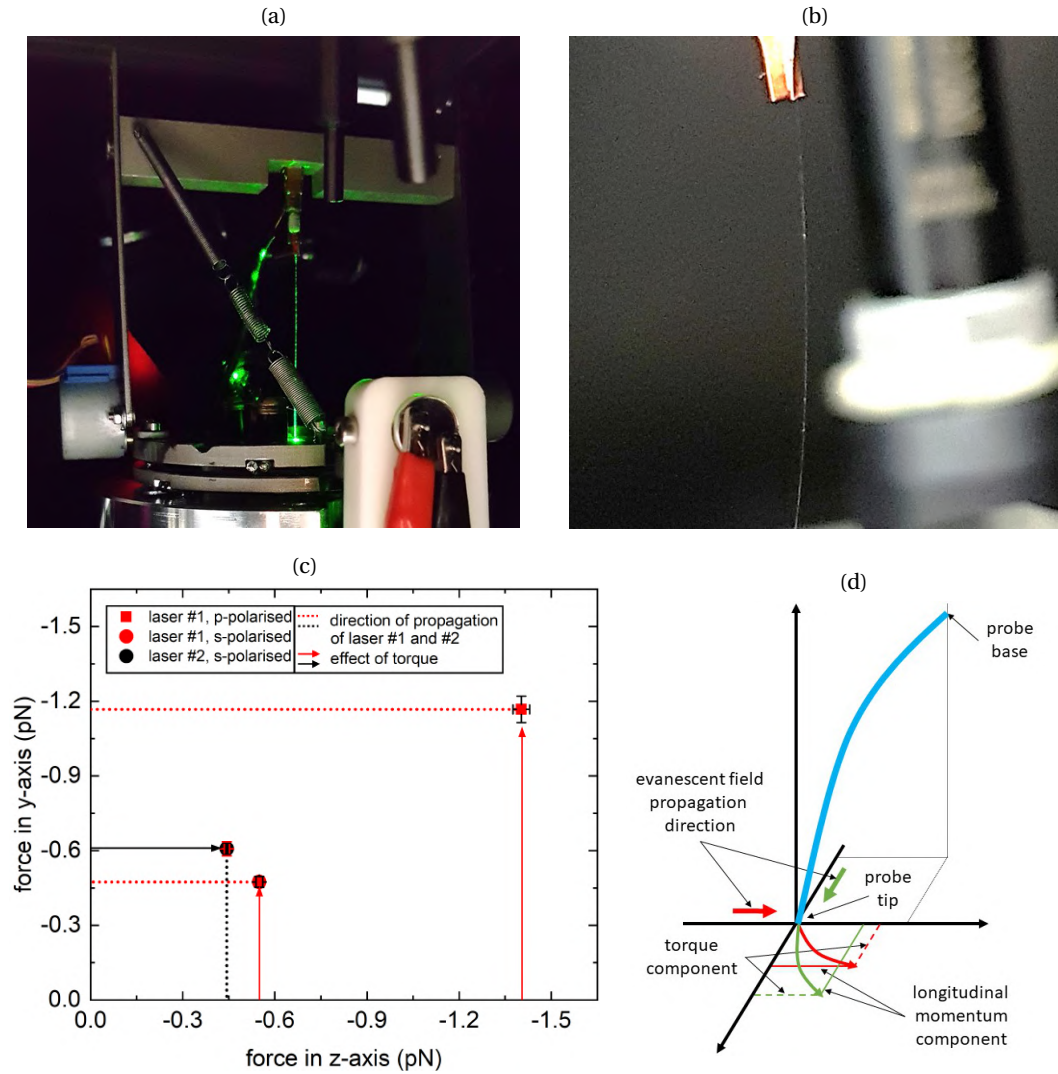


FIGURE 6.6. **(a)** Photograph of a modified 'bridge' setup with a glass micro-needle mounted and positioned in the evanescent field. Coupling of light inside the micro-needle clearly visible. **(b)** Photograph of a slightly curved handmade glass micro-needle mounted on a malleable copper holder. **(c)** Force measurement results for the glass probe exposed to evanescent field generated by laser #1 (red data points) and laser #2 (black data point) (see figure 6.1 for more details). Due to the misalignment of the base of the probe and the tip, a torque acting on the probe is present and can be explained with help of **(d)** schematic

the tip of the probe is not aligned directly underneath the base of the probe. Meaning that the effect of a force along z-axis or y-axis will result in a translation combined with a torque as described in figure 6.6d.

Figure 6.6c shows the measurements of the force experienced by the sphere in the evanescent

field, created by laser #1 ( $\lambda = 660\text{nm}$ , 69mW) and #2 ( $\lambda = 642\text{nm}$ , 66mW) at  $\alpha = 43.5^\circ \pm 0.5^\circ$  incident angle, which propagate at  $90^\circ$  to each other (see figure 6.1). The deflection recorded is consistent with the transfer of longitudinal momentum from the evanescent field (dotted line) and when considering the off axis movement as the result of a torque caused by the misalignment of the probe (solid arrow). The ratio between the forces generated by the s-polarised and p-polarised light (0.41), can be partially explained by the difference in intensity of the fields due to the difference in the corresponding Fresnel coefficients for s-polarised and p-polarised light (discussed in section 2.2.3).

The magnitude of the force measured was again of the same order of magnitude as in the previous 2 experiments. However the addition of torque when using the curved glass micro-needles and a slight difference in bead diameter, made the comparison less accurate

The use of a glass cylindrical micro-needles although not suitable for robust statistical studies of optical force fields, does have some unique advantages. Due to the macroscopic length of the needle it is possible to observe it with a simple optical USB microscope and figure 6.6a clearly shows the light coupling inside the probe through frustrated total reflection, giving much support the hypothesis presented in chapter 5 relating to the origin of the bias bending in Si<sub>3</sub>N<sub>4</sub> cantilevers.

## 6.2 Belinfante spin momentum

An overview of the different investigations into the helicity-dependent, transverse Belinfante spin momentum is presented in this section, along with an improved experimental procedure for measuring the spin momentum, based on its first direct observations in 2016 [3]. The underpinning theory of the manifestation of the Belinfante spin momentum was presented in chapter 2.

### 6.2.1 Belinfante spin momentum - overview

In 2016, Antognozzi et al. [3] reported on the first ever direct observation of the Belinfante spin momentum on a dielectric probe. In fact, this measurement was the first reported optomechanical effect of light which was not associated with either the gradient force, the orbital component of momentum, the scattering of light or a the recoil effect due to the geometry of the object. The effect measured was purely caused by the transverse spin-dependent Belinfante spin momentum, independent on the geometry of the object. After decades of considering it as a 'virtual' component of light, Bliokh et al. [11] argued that it could in fact be observed in a structured field. In a homogeneous field, the time averaged spin momentum component averages to zero. However in a structured field, it was argued that the inhomogeneity of the field would cause the average effect to be non-zero. The concept is best understood as an analogy to spin-hall effect (see figure 6.7). Here the system can be thought of as being made out of small polarisation dependent spin flow circulating loops. In a homogeneous medium they all cancel out, however in a non-homogeneous one, like the evanescent field, have a non-zero net magnitude giving rise to a net spin flow.

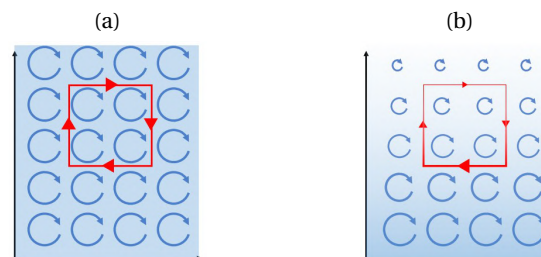


FIGURE 6.7. Analogous to spin-hall effect, the Belinfante spin momentum originates from the spin flow loops. Where **(a)** in a homogeneous field they cancel out, whilst **(b)** in an inhomogeneous field they do not, giving rise to a non-zero net spin flow.

The measurements reported by Antognozzi et al. were performed using the previous generation of LMFM. They varied the polarisation state of the evanescent field by rotating a quarter waveplate. The measured total force imparted on the cantilever can be seen in figure 6.8a. It is clear that the magnitude of the force for the right-handed and the left-handed polarisations is significantly different. The data then was fitted and computationally split into an even and odd component, with the latter revealing the predicted Belinfante spin momentum contribution as well as the imaginary Poynting vector contribution (see figure 6.8c). The even part was attributed to a possible small rotation of the cantilever resulting in manifestation of the canonical momentum.

Subsequently, the Belinfante spin momentum has been observed by other groups. Liu et al. [12] performed the measurements using optical tweezers and measured in 3 dimensions, the response of a dielectric sphere to a changing polarisation of the evanescent wave. Svak et al. [13] also utilised optical tweezers, but instead of using an evanescent field, they used a cross-section of a Gaussian beam as their sampled inhomogeneous field giving rise to the helices dependent, transverse force.

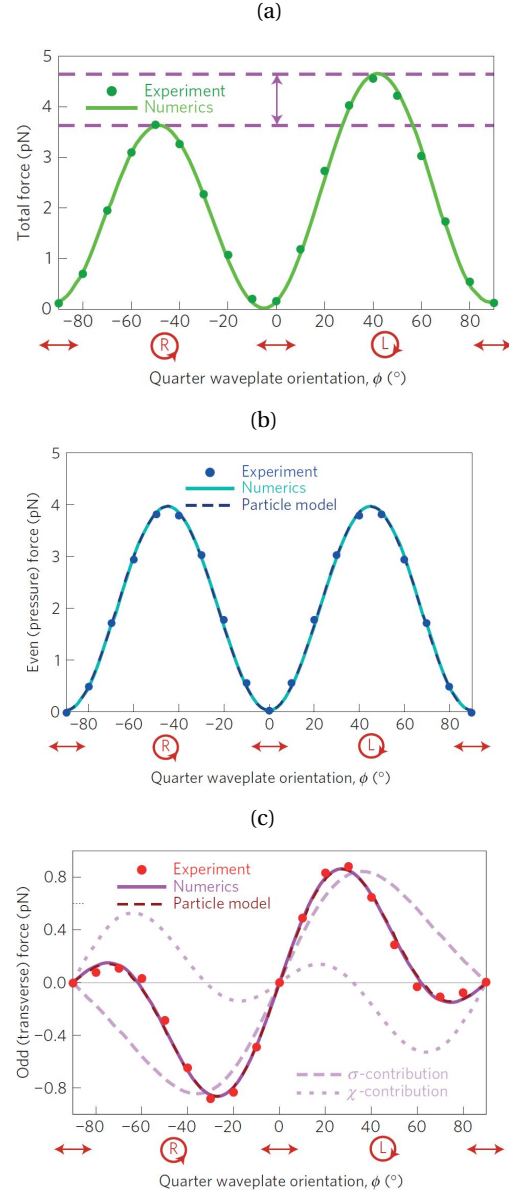


FIGURE 6.8. Previous Belinfante measurements reported in [3]. (a) the total force measured by a cantilever from which (b) an even and (c) odd parts were computationally separated. The odd part is a manifestation of the Belinfante spin momentum.

### 6.2.2 Direct measurement of the Belinfante's spin momentum by removing the bias bending

The previous detailed analysis of the bias bending effect, combined with the innovative design of the new generation of LMFM, converge at this point of the work and result in an improved experimental procedure to directly measure the Belinfante spin momentum. This new method does not use any ad-hoc computational techniques to extract the helicity-dependent component of the force from the total force detected.

The theory on the Belinfante spin momentum has been described in chapter 2 and the below consideration follows from that.

The general optical path setup in the new LMFM is equivalent to that of the previous instrument [3], and so it is expected that the measurement of the total force experienced by the cantilever would be reproduced. On the other hand, the better understanding of the origin of the bias bending, as caused by light which coupled into the cantilever, combined with the discovery that only p polarised light is capable of propagating inside the probes used (and positioned in orientation 'A'), opens

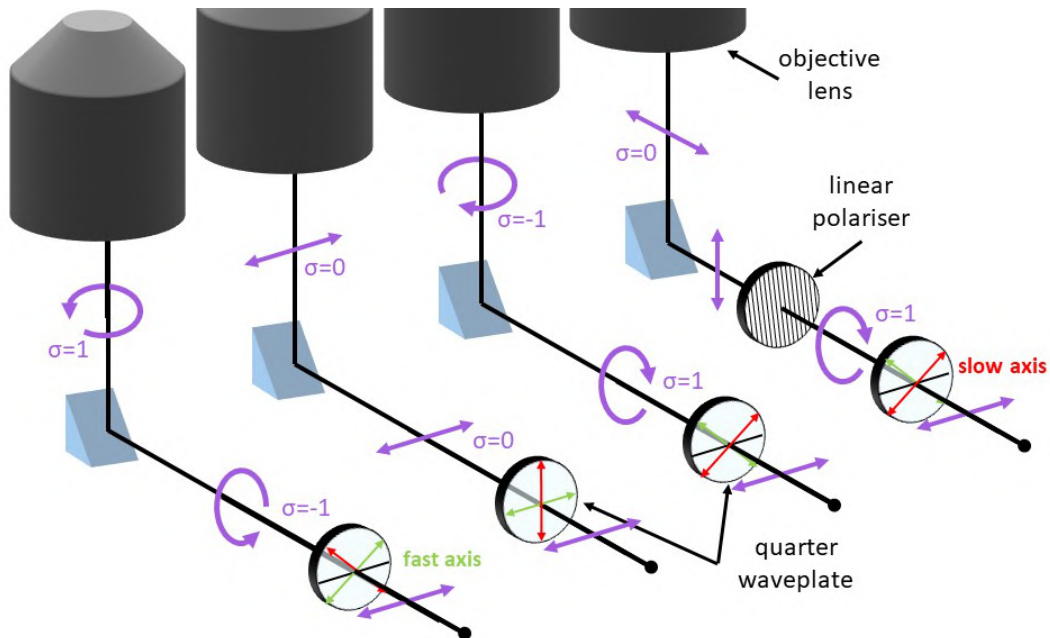


FIGURE 6.9. The optical setup for the Belinfante spin momentum measurements. Shown are the optical components and their effect on the polarisation state of the beam

up the possibility to measure both the total force on the cantilever as well as the corresponding bias bending affecting the total measurement. Once these two components are measured, one can extract the Belinfante's effect by simply subtracting the bias bending effect for the total force. The new experimental procedure is detailed below.

A cantilever (in orientation 'A') was positioned 30nm above the cover slip. The polarisation of laser #1 was controlled by rotating the quarter waveplate, between  $\phi = -100^\circ$  and  $\phi = 100^\circ$  at  $10^\circ \pm 2^\circ$  steps, with respect to the s-polarised incoming beam. A further removable linear polariser is used to set the polarisation of the laser 1 to "p" after the QWP (see figure 6.9). The QWP was set to be at an angle  $\phi = 0$  when the light intensity after the p-polariser is at the minimum. The beam is then reflected by a right-angled mirror underneath the objective lens. The incidence angle was set to  $\alpha = 55^\circ$  (see section 3.4.1).

By rotating the quarter waveplate (with no linear polariser present) and measuring the corresponding total force  $F_{total}$ , a completely analogous result in [3] (see also figure 6.8) was obtained and can be seen in figure 6.10a. A second data set is collected with the linear polariser introduced in the laser beam path after the quarter waveplate and before the right-angled mirror (see figure 6.9). In this way, only the p-polarised component of the polarisation state of the beam after the QWP can reach the probe. As the QWP is rotated to reproduce the same positions used in the previous set of measurements, the linear polariser ensures that the deflection measured is only due to the bias bending effect  $F_{bias}$  (see figure 6.10b). The experiment was performed using a Meadowlark UPM-100-VIS linear polariser with a very high extinction ratio of 100000:1 between s-polarisation and p-polarisation to ensure minimal cross-talk between the two states. However the introduction of the polariser also attenuates the p-polarised component of light. In order to find this scaling factor, the incoming laser beam polarisation was rotated by  $90^\circ$  and set to p polarisation. The deflection of the cantilever was measured for the p-polarised light with and without the linear polariser in the path and the ratio of the two is used as the scaling factor  $c_p$ .

For fitting purposes, a small correction to the equations for the polarisation parameter  $m_i$  (equation (2.60)) as well as the stokes parameters (in equations (2.64) to (2.66)) needs to be included as the right-angled mirrors, directing the beam into the objective lens, are not perfect reflectors. To account for this effect, the intensity of the beam for the s polarised and p polarised light was

measured before ( $I_{s1}$  and  $I_{p1}$  and after ( $I_{s2}$  and  $I_{p2}$ ) the reflection from the mirror. The ratio of these intensities, gives the attenuation coefficient for each of the orthogonal polarisation states

$$\begin{aligned} a_s &= \sqrt{\frac{I_{s2}}{I_{s1}}} \\ a_p &= \sqrt{\frac{I_{p2}}{I_{p1}}}. \end{aligned} \quad (6.3)$$

The change in the intensity of the s-polarised and p-polarised components will affect the ellipticity of the polarisation of the beam. Hence the following adjustments need to be made, by adding an attenuation factor  $a_{s/p} = a_s/a_p$  as follows

$$m_i = a_{s/p} \frac{-\cos(2\phi) - i \cot(\delta/2)}{\sin(2\phi)}. \quad (6.4)$$

giving

$$\tau(\phi) = \frac{\sin^2(2\phi) - a_{s/p}^2 (\cos^2(2\phi) + \cot^2(\delta/2)) (\cosh^2(\gamma) - \cos^2(\alpha))}{\sin^2(2\phi) + a_{s/p}^2 (\cos^2(2\phi) + \cot^2(\delta/2)) (\cosh^2(\gamma) - \cos^2(\alpha))} \quad (6.5)$$

$$\chi(\phi) = 2 \frac{a_{s/p} \sin(2\phi) (\cosh(\gamma) \sin(\alpha) \cos(2\phi) - \sinh(\gamma) \cos(\alpha) \cot(\delta/2))}{\sin^2(2\phi) + a_{s/p}^2 (\cos^2(2\phi) + \cot^2(\delta/2)) (\cosh^2(\gamma) - \cos^2(\alpha))} \quad (6.6)$$

$$\sigma(\phi) = 2 \frac{a_{s/p} \sin(2\phi) (\cosh(\gamma) \sin(\alpha) \cot(\delta/2) + \sinh(\gamma) \cos(\alpha) \cos(2\phi))}{\sin^2(2\phi) + a_{s/p}^2 (\cos^2(2\phi) + \cot^2(\delta/2)) (\cosh^2(\gamma) - \cos^2(\alpha))}. \quad (6.7)$$

The experimental results were fitted using the following expressions. For the total force  $F_{total}$  recorded (presented in figure 6.10a), the fitting was performed using

$$\begin{aligned} F_{total}(\phi) &= a + F^{s+i}(\phi) + c_p F_{bias}(\phi) \\ &= a + b\chi(\phi) + c\sigma(\phi) + d\sin^2(2\phi) \end{aligned} \quad (6.8)$$

where  $F^{s+i}$  is the Belinfante spin momentum and imaginary Poynting contribution,  $a, b, c, d$  are fitting parameters, with  $a = F_{total}(0)$ .  $\chi(\phi), \sigma(\phi)$  are the Stokes parameters given by equations (6.5) to (6.7). The experimental data presented in 6.10b, corresponds to the bias bending force once accounted for the scaling factor  $c_p$ . The fitting function is given by

$$c_p F_{bias}(\phi) = d \sin^2(2\phi). \quad (6.9)$$

Finally, the difference between the two experimental data sets (seen in figure 6.10c) was fitted using the following function

$$\begin{aligned} F^{s+i}(\phi) &= F_{total}(\phi) - c_p F_{bias}(\phi) - a \\ &= b\chi(\phi) + c\sigma(\phi) \end{aligned} \tag{6.10}$$

Equation (6.10) presents the  $\sigma$ -dependent and  $\chi$ -dependent fundamental optical forces, acting on an object in an evanescent wave in a transverse direction to the propagation of the wave.

Figure 6.10c shows an excellent agreement between the experimental data and the theoretical fitting. It need to be emphasised that the removal of the bias bending is based on experimental results and not mathematical interpolation, which is a significant improvement to the previously reported measurements [3].



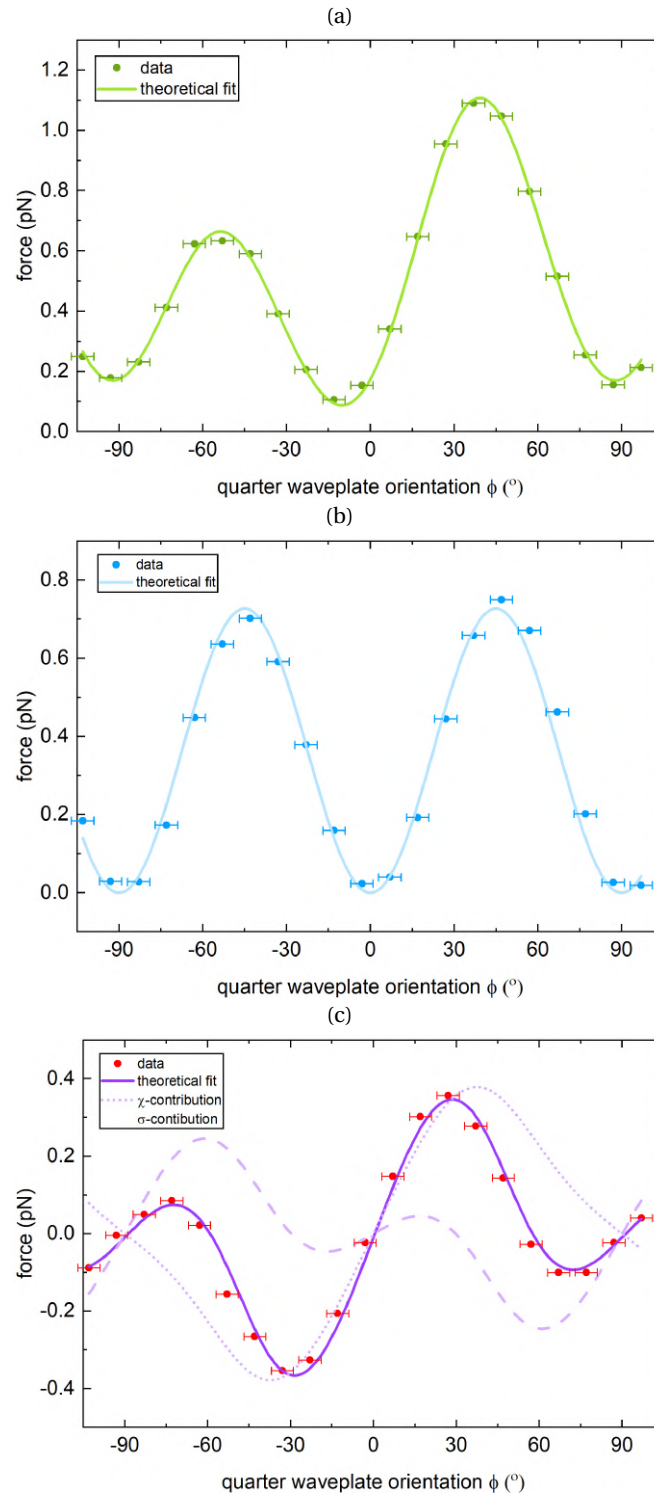


FIGURE 6.10. Experimental results for Belinfante spin momentum measurement. **(a)** shows the data and the theoretical fit to the total force measured by the probe, including the experimentally measured contribution from the bias bending shown in **(b)**. Shown in **(c)** is the transverse force experienced by the cantilever due to the contributions from the  $\sigma$ -dependent Belinfante spin momentum and the  $\chi$ -dependent imaginary Poynting vector contribution. This graph was obtained by subtracting force measurements in **(a)** and **(b)**. The fitting curve is calculated using equation (6.10).

An additional argument supporting the subtraction of the even bias bending contribution as opposed to the assumption that the even part of the total force measured is due to the transfer of longitudinal momentum to the cantilever at a small angle  $\varphi$  is, that with the introduction of the scheme presented in section 3.6.6, it is possible to measure the angle  $\varphi$ . In fact, for this experiment  $\varphi = 20.7^\circ \pm 0.9^\circ$ , which would mean that the  $\tau$ -dependent contribution would have to act in the negative y direction.

The experiment presented in this section, gives an additional insight into the fundamental mechanism of the spin momentum transfer. With the extreme aspect-ratio of the probe, it was established in chapter 5 that only the p polarised light could couple inside the cantilever. This means that the transverse, helicity dependent momentum is not transferred inside the cantilever but it is transferred through the interaction of the evanescent field with only the surface of the probe. This conclusion is consistent with the interpretation of the numerical simulations included in the 2016 paper by Antognozzi et al. [3].

## 6.3 Conclusions

The new design of the LMFM has enabled unique force measurements capabilities that are ideal when dealing with optical forces. The biggest challenge for this technique, remains the manufacturing of probes that are not affected by bias bending. However, the better understanding of the origins of the bias bending provided by this work, opens up the possibility to design original experimental protocols to detect specific optical effects with high accuracy. In this respect, section 6.1 demonstrated the measurements of the longitudinal momentum of the evanescent field using a physical probe. Whilst section 6.2.2 contains a demonstration of the helicity-dependent spin momentum without need for arbitrary mathematical decoupling of the even and odd component of the force.. Finally, the extreme aspect-ratio of the probe, together with the understanding of the bias bending, gave a new insight into the surface-nature of the Belinfante's spin momentum.

## 6.4 Bibliography

- [1] D. C. Kohlgraf-Owens, S. Sukhov, and A. Dogariu, “Near-Field Topography of Light,” *Optics and Photonics News*, vol. 23, p. 39, Dec. 2012.
- [2] D. C. Kohlgraf-Owens, S. Sukhov, L. Greusard, Y. De Wilde, and A. Dogariu, “Optically induced forces in scanning probe microscopy,” *Nanophotonics*, vol. 3, Jan. 2014.
- [3] M. Antognozzi, C. R. Bermingham, R. L. Harniman, S. Simpson, J. Senior, R. Hayward, H. Hoerber, M. R. Dennis, A. Y. Bekshaev, K. Y. Bliokh, and F. Nori, “Direct measurements of the extraordinary optical momentum and transverse spin-dependent force using a nano-cantilever,” *Nature Physics*, vol. 12, pp. 731–735, Aug. 2016.
- [4] S. Kawata and T. Sugiura, “Movement of micrometer-sized particles in the evanescent field of a laser beam,” *Optics Letters*, vol. 17, p. 772, June 1992.
- [5] S. Kawata and T. Tani, “Optically driven Mie particles in an evanescent field along a channeled waveguide,” *Optics Letters*, vol. 21, p. 1768, Nov. 1996.
- [6] M. L. Huber, R. A. Perkins, A. Laesecke, D. G. Friend, J. V. Sengers, M. J. Assael, I. N. Metaxa, E. Vogel, R. Mareš, and K. Miyagawa, “New International Formulation for the Viscosity of H<sub>2</sub>O,” *J. Phys. Chem. Ref. Data*, vol. 38, no. 2, p. 26, 2009.
- [7] S. M. Barnett and R. Loudon, “The enigma of optical momentum in a medium,” *Philosophical Transactions of the Royal Society A: Mathematical, Physical and Engineering Sciences*, vol. 368, pp. 927–939, Mar. 2010.
- [8] S. M. Barnett, “Resolution of the Abraham-Minkowski Dilemma,” *Physical Review Letters*, vol. 104, Feb. 2010.
- [9] J. P. Gordon, “Radiation Forces and Momenta in Dielectric Media,” *Physical Review A*, vol. 8, pp. 14–21, July 1973.
- [10] A. Ashkin and J. M. Dziedzic, “Radiation Pressure on a Free Liquid Surface,” *Physical Review Letters*, vol. 30, pp. 139–142, Jan. 1973.

- [11] K. Y. Bliokh, A. Y. Bekshaev, and F. Nori, “Extraordinary momentum and spin in evanescent waves,” *Nature Communications*, vol. 5, p. 3300, May 2014.
- [12] L. Liu, A. Di Donato, V. Ginis, S. Kheifets, A. Amirzhan, and F. Capasso, “Three-Dimensional Measurement of the Helicity-Dependent Forces on a Mie Particle,” *Physical Review Letters*, vol. 120, May 2018.
- [13] V. Svak, O. Brzobohatý, M. Šiler, P. Ják, J. Kaňka, P. Zemánek, and S. H. Simpson, “Transverse spin forces and non-equilibrium particle dynamics in a circularly polarized vacuum optical trap,” *Nature Communications*, vol. 9, p. 5453, Dec. 2018.



# CHAPTER 7

## USE OF EVANESCENT FIELD SCATTERING TO INVESTIGATE SUB-CELLULAR ACTIVITY IN BACTERIA

So far the evanescent field was used to detect the position of the micro-cantilever tip and subsequently that micro-cantilever was used to measure polarisation-dependent optical forces. In this chapter we present a new application of total internal reflection microscopy to study the metabolic activity of bacteria at the single cell level. Presented below is work contributing to establishing the Sub-cellular Fluctuation Imaging method [1, 2].

Creating the fluctuation description was a collaborative effort between myself, Dr. Massimo Antognozzi, Dr. Ben Maughan and PhD student Kanasanun Phonrat. The measurements of fluctuation levels in sections 7.2 and 7.3 were jointly performed with PhD student Kanasanun Phonrat. Figures 7.1, 7.2 and 7.4 are adapted or reproduced from [2], whilst the remaining figures were entirely created by me.

### 7.1 Sub-cellular Fluctuation Imaging (SCFI) - overview

In recent year, new diagnostic methods have been developed to perform rapid antimicrobial susceptibility tests (AST) [3] to address the evergrowing issue of increasing antimicrobial resistance of bacteria. It is believed that the excess use of antibiotics has allowed bacteria to mutate and become

resistant to the limited number of antibiotics that are known to us [4]. One of the contributing factors to common misuse of antibiotics is the fact that the most commonly used Antimicrobial Susceptibility Tests (AST) in medical setting (such as culture method) take between 24 and 48 hours [5]. This results in doctors taking educated guesses on regular basis when prescribing antibiotics to patients. In recent years, the search for rapid ASTs turned its attention to the nanoscale world [6, 7]. These studies, established a connection between the viability of a bacteria and their movement detected using AFM probes [7]. These nano-scale bacterial fluctuations were also studied by Syal et al. [8] using a promising method based on a plasmonic technique. In order to understand the origin of these intracellular activity, Parry et al. [9] investigated the connection between the metabolic state of the bacterium and the motion of tagged particles in the bacterial cytoplasm. The study found that these fluctuations are out of equilibrium effects and are directly linked to the metabolic activity of the bacterial cells. These conclusions were expanded to eukaryotic cells by Guo et al. [10].

Sub-Cellular Fluctuations Imaging (SCFI) is a method developed in the group led by M. Antognozzi to observe the viability of bacteria deposited on a glass surface using total internal reflection microscopy [1, 2].

The SCFI method presented here, utilises evanescent wave illumination to observe sub-cellular movements of bacterial constituents. The measurements are performed using the CMOS camera, normally used for bright field microscopy in LMFM (see section 3.4), to observe the scattering of the evanescent field within the bacterial envelope. Under standard brightfield illumination, the only way to determine if a stationary bacterium is dead or alive, is to wait until the cell divides or grows. However the near-field illumination allows to observe, in real time, fluctuations of the scattered signal intensity coming from a narrow region within the immobilised bacterium (see figure 7.1).

The bacteria used for the proof of the concept were the *Escherichia coli* (*E.coli*) bacteria deposited onto amino-functionalised[11, 12] glass-bottomed petri dishes (Cellview cellculture dish, GreninerBio-One, 627861) and bound to the surface using the anti-*E.coli* antibodies (abcam ab137967). Bacteria were prepared in 3 different states; 1) dead (paraformaldehyde-treated), 2) stationary phase (in a low nutritional buffer resulting in low metabolism) and 3) exponential phase (in a standard glucose-rich buffer supporting high metabolism). The full description of the preparation process of the bacteria can be found in [1, 2].

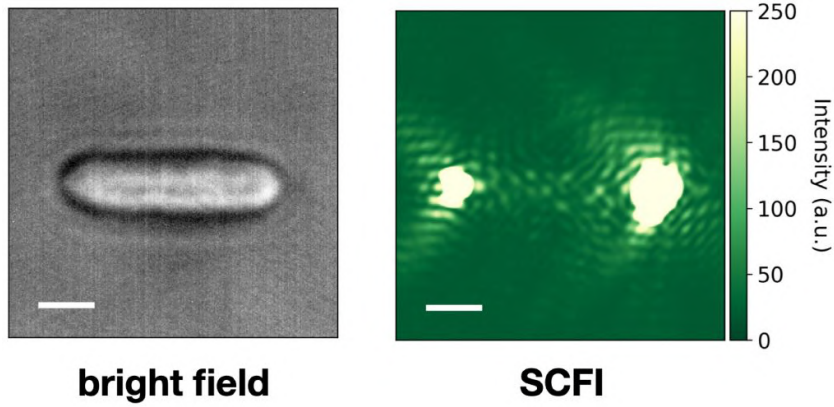


FIGURE 7.1. Comparison of images of a single *E.coli* bacterium in (left) standard optical microscopy and (right) SCFI. Under evanescent field illumination, sub-cellular features are visible between the 2 poles of the bacterium. When recording a time sequence, the movement of these features can be used by the SCFI method to determine the viability of the bacterial cell. Adapted from [2]

### 7.1.1 Fluctuation description

To quantify the sub-cellular fluctuations recorded using SCFI, a time sequence of a bacterium under evanescent field illumination is recorded for 20s at a frame rate of 20fps. Subsequently a small region of interest (ROI), 30pxs×30pxs, is selected within the outline of a bacterium as shown in figure 7.2a and 7.2d (for a bacterium in an exponential phase and dead respectively). Next, the intensity  $i_n(x, y)$  of each individual pixel in the full time sequence of  $N$  frames is calculated according to the following equation:

$$i_n(x, y) = \ln(I_n(x, y) - I_{bg}) \quad (7.1)$$

where  $I_n(x, y)$  is the recorded raw intensity of a given pixel in a given frame where  $n \in \{1, \dots, N\}$  and  $I_{bg}$  is the background intensity (see figure 7.2b and 7.2e). Finally, the fluctuation level is defined as

$$\bar{\sigma} = \langle \sigma(x, y) \rangle_{ROI} \quad (7.2)$$



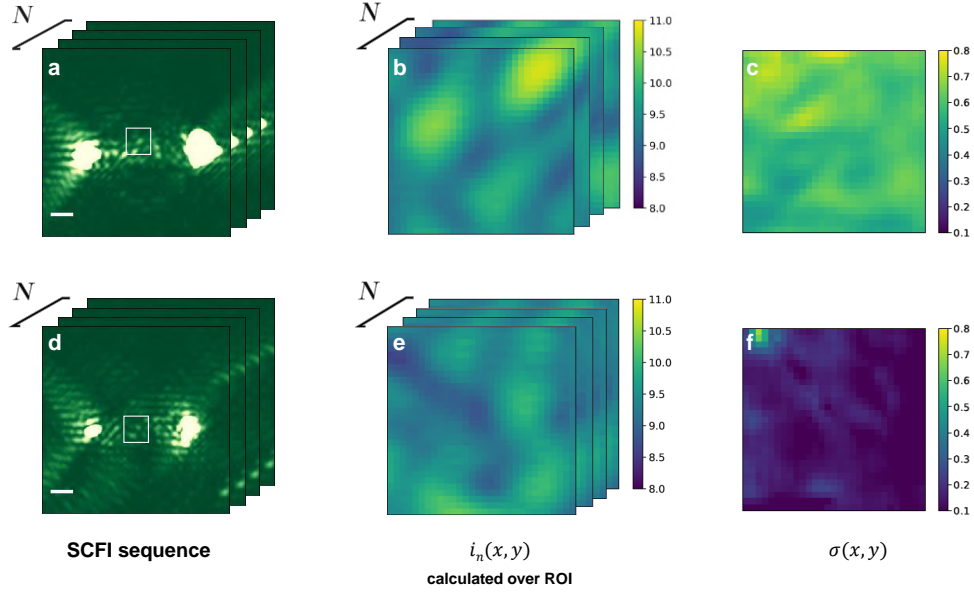


FIGURE 7.2. Visualisation of the SCFI data analysis. **(a),(d)** A sequence of images of a bacterium in exponential phase (top row) and a dead bacterium (bottom row) were observed for 20s at 20fps. A  $30 \times 30$  ROI (white square) is selected within the envelope of the bacterium, in between the 2 saturated spots. **(b),(e)**  $i_n(x, y)$  given by equation 7.1 is calculated for the selected ROI for all the pixels in all the frames. **(c),(f)** Heat map of the standard deviation  $\sigma(x, y)$  of the intensity of the pixels within selected ROI, showcasing the observed difference in the levels of fluctuations between the exponential phase and the dead bacteria. Reproduced from [2]

as an average of the standard deviation  $\sigma(x, y)$  of intensity  $i_n(x, y)$  of each pixel within the ROI (see figure 7.2c and 7.2f). The background intensity  $I_{bg}$  is found by plotting a histogram of raw pixel intensity values  $I_n(x, y)$  and finding the minimum value of intensity (see figure 7.3). Due to the evanescent field illumination, the distribution of the pixels of a living bacterium can be described using a log-normal distribution given by the following expression

$$I = e^{\left( \frac{-d \ln(I_n(x, y) - I_{bg}) - \mu}{2s^2} \right)} \quad (7.3)$$

where  $d$  is the decay length of the evanescent field,  $\mu$  is the mean intensity and  $s$  is the standard deviation.

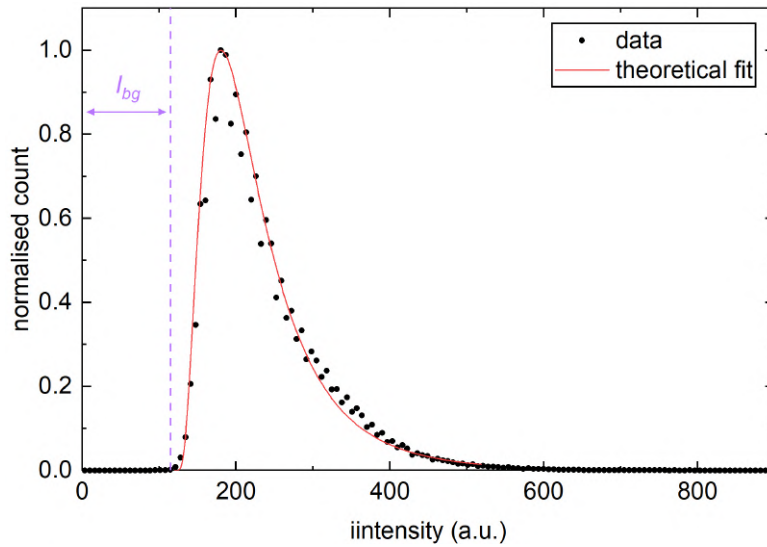


FIGURE 7.3. Log-normal distribution of SCFI data of a stationary phase *E.coli* bacterium, from which the background intensity  $I_{bg}$  is found

To establish the metabolic state of a bacterial sample, the fluctuation measurements are repeated for a statistically representative group of bacteria in each sample, as each individual bacteria can be at a different point in their metabolic cycle. In the case of *E.coli* DH1 we found that recording the signal from 50 bacteria is sufficient to distinguish between the three metabolic states previously defined.

Most importantly, the method presented here is not just a binary test, like most conventional ASTs are, but it can actually identify different degrees of metabolic state between bacterial samples. This capability opens up a possibility of a rapid viability test on bacteria treated with a bacteriostatic antibiotic as this type of antimicrobial does not kill the bacteria, but only stops them from growing. Figure 7.4 demonstrates the capability of SCFI to distinguish between different levels of fluctuations recorded for bacteria in 3 different states. All *E.coli* samples for this experiment were prepared by PhD student Kanasanun Phonrat and came from a single overnight culture. The stationary sample was taken directly from the overnight culture. The exponential sample was prepared by adding 100 $\mu$ l of the overnight culture into 10ml of Lysogeny broth (LB) and then incubated for around 120 minutes at 37°C in a shaker set to 180 rpm. The dead sample was prepared by incubating the same overnight *E. coli* culture with 2% paraformaldehyde for 40 minutes and stored in 0.06% sodium azide ( $NaN_3$ ) [2].

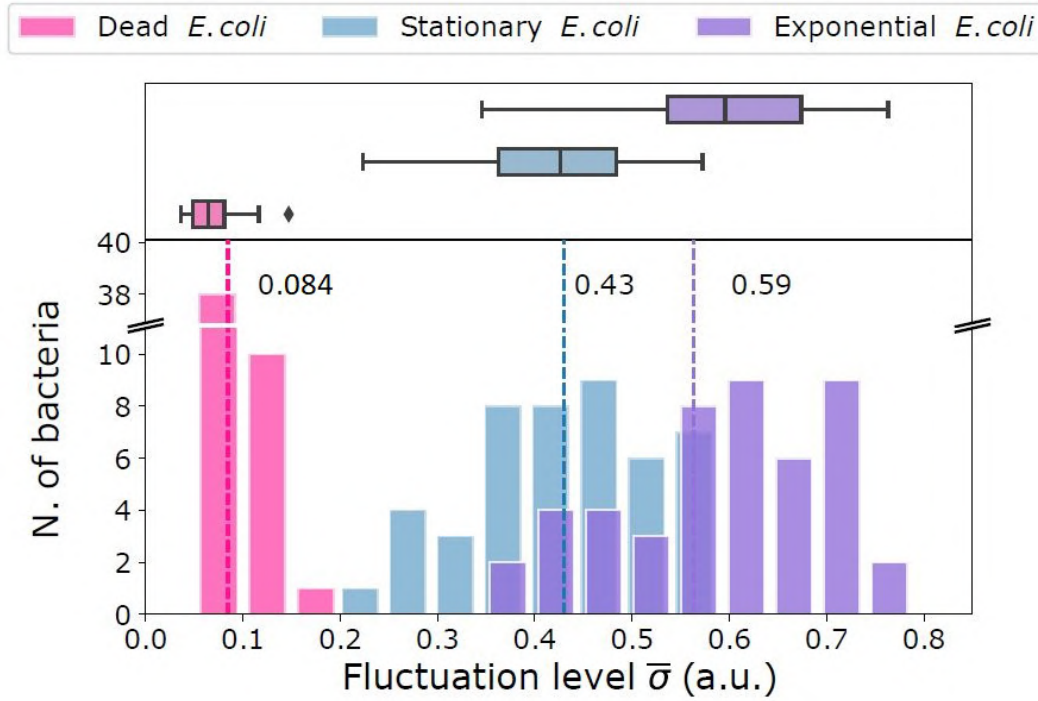


FIGURE 7.4. Fluctuation measurements of 3 populations of *E.coli* bacteria, each in a different state. Clearly distinguishable dead (pink), stationary phase (blue) and exponential phase (purple) populations, which were prepared from the same overnight culture, have mean fluctuation values of  $0.084 \pm 0.003$ ,  $0.43 \pm 0.01$  and  $0.59 \pm 0.02$  respectively. For the three distributions the  $p$ -value was found to be  $\ll 0.01$ . Reproduced from [2]

## 7.2 Explaining the scattering pattern of a bacterium in an evanescent field

When imaging bacteria using SCFI, the two large bright spots at poles of the bacterium (see figures 7.1 and 7.2) constitute constant feature when the bacterial cell is aligned in the direction of propagation of the evanescent field. For this reason, considerable attention was dedicated to understand their physical origins. If a bacterium is particularly short, the lack of unsaturated space between the two saturated spots, can prevent successful measurements of the fluctuation levels within the ROI. To understand the origins of the two spots, 2-dimensional FDTD simulations in Lumerical were created.

Figure 7.5a shows a simulation of a bacterium in an evanescent field created by a total internal

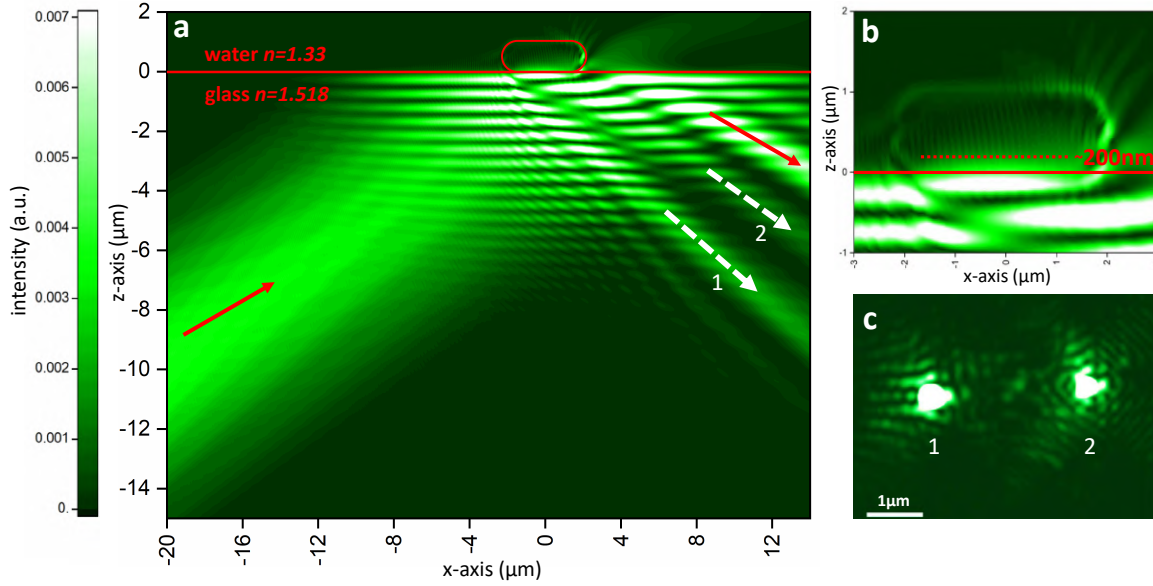


FIGURE 7.5. Finite-difference time-domain (FDTD) model of the electromagnetic field generated using SCFI at the glass-water interface with a bacterium. The refractive index of the glass, water and the bacterium are 1.518, 1.33 and 1.38, respectively. The incident angle of the laser is  $67^\circ$ , the wavelength used in this case is 561nm. The model shows how part of the evanescent wave is frustrated by the bacterium and propagates in the water. The model confirms a small penetration in the cell. At 100 from the glass surface the value of the field is less than half its value at the surface. Red arrows indicate the direction of the laser beam. Reproduced from [2]

reflection of a Gaussian-profile laser beam at  $\lambda = 561\text{nm}$  and an angle of incidence  $= 67^\circ$ . The refractive index of the glass and water were set to  $n_{\text{glass}} = 1.518$  and  $n_{\text{H2O}} = 1.33$  respectively. Assuming the wall thickness of E.coli bacteria in the range of 20nm [13], the bacterium itself was modelled to have a 20nm-thick lipid layer (with a refractive index of  $n_{\text{lip}} = 2$  [14]) surrounding the a uniform cytoplasm with a refractive index of  $n_{\text{bact}} = 1.388$  [15].

The presence of the cell wall is essential for the observation of the two large spots at the poles of the bacterium. The simulation produces two directional beams (marked with white dashed arrows 1 and 2 as seen in figure 7.5a) that give rise to the observed two bright spots on either end of the bacterium (1 and 2 as seen in figure 7.5c).

Reduction of the 2 bright spots is particularly important in the context of pixel saturation, as

saturated pixels do not contain any information on fluctuation levels as the standard deviation is equal to 0. They are also responsible for the interference effects that alter the background level  $I_{bg}$  of the recorded signal. Changes in background levels can introduce a systematic error decreasing the calculated level of fluctuations.

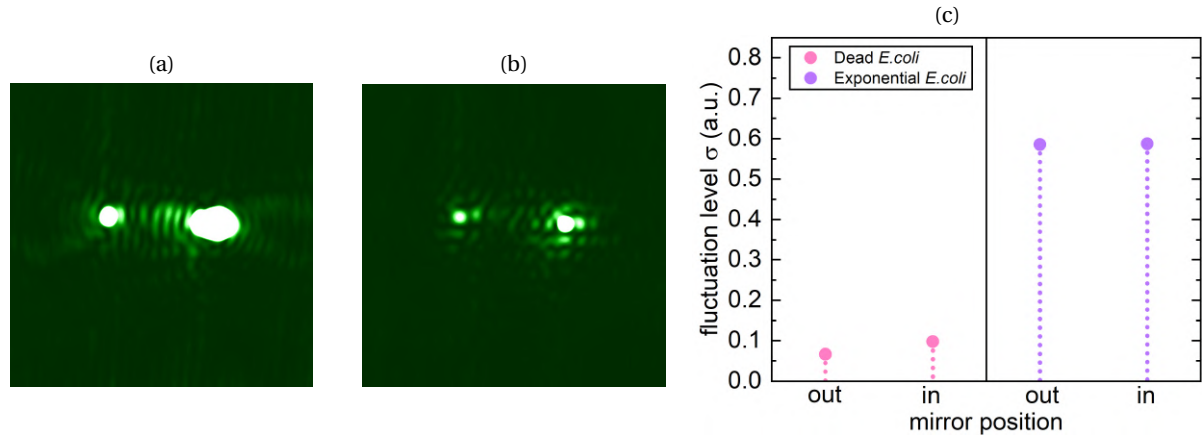


FIGURE 7.6. **(a),(b)** Images from SCFI taken with the outgoing mirror in different positions **(a)** the mirror is moved away from the centre of the lens (out) and **(b)** the mirror is moved closer to the centre of the objective lens (in) **(c)** Comparison of fluctuation levels measured for a dead bacterium and a bacterium in exponential phase, for the mirror in positions (out) and (in) showing that changing the mirror position reduces the intensities of 2 spots, without affecting the bacterial fluctuation levels recorded by SCFI.

The high directionality of the light scattered from the poles of the bacterial cell (figure 1.5a) suggests that the intensity of the two poles can be significantly reduced by stopping the corresponding  $k$ -vectors in the focal plane. To test the simulation prediction, the position of the outgoing beam mirror was changed so that it would collect light scattered at steeper angles (see figure 3.4). Indeed by varying the position of the mirror, the intensity of the 2 spots was altered without simultaneously significantly affecting the image resolution and the level of fluctuations of bacteria (see figure 7.6). The range of movement of the mirror underneath the objective lens did not allow to fully eliminate the 2 spots as the scattering from the bacterial poles contains a non-directional component. In general terms the results of the simulation can be explained when looking at the problem from a ray diagram perspective. In this case a curved, semi-spherical end of a bacterium will scatter the light,

with larger intensity closer to the surface due to an exponential decay of the evanescent field [16].

### **7.3 Manipulating bacteria with LMFM probe to study the origin of the SCFI signal**

As mentioned before, the methods used by Syal et al. [8] and Longo et al. [7] to study bacterial fluctuation, heavily rely on the correct immobilisation of the bacteria on the plasmonic surface and the cantilever, respectively. In fact, a “too strong” immobilisation when using an excess of antibodies can cause a reduction in fluctuation for the same physiological conditions potentially resulting in a false (dead) reading. The reason for this dependency, is based on the fact that these methods detect the mechanical motion of the whole bacterium. Therefore if a bacterium is bound too strongly to the surface, it will no longer move, giving appearance of being in a lower metabolic state. The SCFI method however, does not rely on the bacterium motion, but rather on the motion of sub-cellular components within the bacterial cell. To rule out the possibility that the motion of the whole bacterium is the source of the fluctuation signal, a test was performed where an individual bacterium was mechanically constrained against the glass surface using a LMFM probe. As described in chapter 3, the new microscope design enables the manipulation of the probe with nanometer precision and it is fully compatible with working in liquid environment. To ensure the ability to apply a relatively high pressure with the cantilever, a stiffer,  $33\mu\text{m}$ -long silicon nitride probe was used. The higher stiffness prevented buckling of the cantilever when vertically mounted and pressed down on the bacterium.

Figure 7.7 shows the results of fluctuation measurements for a bacterium in stationary phase tethered to the cover slip using with antibodies and subsequently pressed down by the micro-cantilever. With only a 9% change of the fluctuation, the additional whole cell immobilisation of the probe rules out the possibility that cell movements are responsible for the SCFI signal. In contrast with other methods [7, 8], where increase immobilisation of the bacteria caused a reduction in signal levels. The small increase of 9% in the fluctuations shown in 7.7 could be explained by the fact that initially the bacterium was attached using a layer of antibodies with an estimated thickness of 14nm [17]. However, when pressed, the bacterium was pushed closer towards the surface, exposing it to

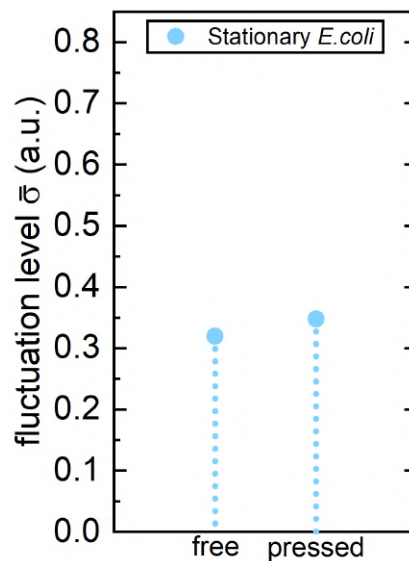


FIGURE 7.7. Comparison of fluctuation levels of the same bacterium when tethered only with antibodies 'free' and when pressed on by a cantilever 'pressed'

higher intensity field, which decays exponentially away from the surface,

## 7.4 Conclusions

The new microscope design allows complete control over the evanescent field illumination, allowing it to easily adopt between working in air and aqueous environments. The use of the evanescent field illumination opens up a possibility of detecting sub-cellular processes which leads to a label free method for quantifying the metabolic state of individual bacteria. Finally, the measurements in section 7.3 demonstrate the ability to perform mechano-optical experiments on living cells.

## 7.5 Bibliography

- [1] C. R. Bermingham, I. Murillo, A. D. J. Payot, K. C. Balram, M. B. Kloucek, S. Hanna, N. M. Redmond, H. Baxter, R. Oulton, M. B. Avison, and M. Antognozzi, “Imaging of sub-cellular fluctuations provides a rapid way to observe bacterial viability and response to antibiotics,” preprint, *Physiology*, Nov. 2018.
- [2] C. R. Bermingham, I. Murillo, K. Phonrat, W. K. Szeremeta, B. Maughan, A. D. J. Payot, M. B. Kloucek, S. Hanna, H. Baxter, J. P. Hays, M. B. Avison, and M. Antognozzi, “Direct Observation of Intracellular Fluctuations as a Rapid Test for Bacterial Viability,” *to be submitted to Scientific Reports*, 2020.
- [3] J. H. Jorgensen and M. J. Ferraro, “Antimicrobial Susceptibility Testing: A Review of General Principles and Contemporary Practices,” *Clinical Infectious Diseases*, vol. 49, pp. 1749–1755, Dec. 2009.
- [4] H. Goossens, M. Ferech, R. V. Stichele, and M. Elseviers, “Outpatient antibiotic use in Europe and association with resistance: A cross-national database study,” *Lancet*, vol. 365, p. 9, 2005.
- [5] Z. A. Khan, M. F. Siddiqui, and S. Park, “Current and Emerging Methods of Antibiotic Susceptibility Testing,” *Diagnostics*, vol. 9, p. 49, May 2019.
- [6] A. Vasala, V. P. Hytönen, and O. H. Laitinen, “Modern Tools for Rapid Diagnostics of Antimicrobial Resistance,” *Frontiers in Cellular and Infection Microbiology*, vol. 10, p. 308, July 2020.
- [7] G. Longo, L. Alonso-Sarduy, L. M. Rio, A. Bizzini, A. Trampuz, J. Notz, G. Dietler, and S. Kasas, “Rapid detection of bacterial resistance to antibiotics using AFM cantilevers as nanomechanical sensors,” *Nature Nanotechnology*, vol. 8, pp. 522–526, July 2013.
- [8] K. Syal, R. Iriya, Y. Yang, H. Yu, S. Wang, S. E. Haydel, H.-Y. Chen, and N. Tao, “Antimicrobial Susceptibility Test with Plasmonic Imaging and Tracking of Single Bacterial Motions on Nanometer Scale,” *ACS Nano*, vol. 10, pp. 845–852, Jan. 2016.
- [9] B. R. Parry, “The Bacterial Cytoplasm Has Glass-like Properties and Is Fluidized by Metabolic Activity,” *Cell*, vol. 156, pp. 183–194, 2014.



- [10] M. Guo, A. J. Ehrlicher, M. H. Jensen, M. Renz, J. R. Moore, R. D. Goldman, J. Lippincott-Schwartz, F. C. Mackintosh, and D. A. Weitz, “Probing the Stochastic, Motor-Driven Properties of the Cytoplasm Using Force Spectrum Microscopy,” *Cell*, vol. 158, pp. 822–832, Aug. 2014.
- [11] L. Wildling, B. Unterauer, R. Zhu, A. Rupprecht, T. Haselgr, C. Rankl, A. Ebner, D. Vater, P. Pollheimer, E. E. Pohl, P. Hinterdorfer, and H. J. Gruber, “Linking of Sensor Molecules with Amino Groups to Amino-Functionalized AFM Tips,” *Bioconjugate Chemistry*, p. 10, 2011.
- [12] A. Ebner, P. Hinterdorfer, and H. J. Gruber, “Comparison of different aminofunctionalization strategies for attachment of single antibodies to AFM cantilevers,” *Ultramicroscopy*, p. 6, 2007.
- [13] J. C. Gumbart, M. Beeby, G. J. Jensen, and B. Roux, “Escherichia coli Peptidoglycan Structure and Mechanics as Predicted by Atomic-Scale Simulations,” *PLoS Computational Biology*, vol. 10, p. e1003475, Feb. 2014.
- [14] S. Ohki, “Dielectric constant and refractive index of lipid bilayers,” *Journal of Theoretical Biology*, vol. 19, pp. 97–115, Apr. 1968.
- [15] P. Liu, L. Chin, W. Ser, T. Ayi, P. Yap, T. Bourouina, and Y. Leprince-Wang, “Real-time Measurement of Single Bacterium’s Refractive Index Using Optofluidic Immersion Refractometry,” *Procedia Engineering*, vol. 87, pp. 356–359, 2014.
- [16] D. Ganic, X. Gan, and M. Gu, “Three-dimensional evanescent wave scattering by dielectric particles,” *Optik*, vol. 113, no. 3, pp. 135–141, 2002.
- [17] M. J. Pollitt, G. Buckton, R. Piper, and S. Brocchini, “Measuring antibody coatings on gold nanoparticles by optical spectroscopy,” *RSC Advances*, vol. 5, no. 31, pp. 24521–24527, 2015.

## FINAL CONCLUSIONS

For this project, the new generation of Lateral Molecular Force Microscope was designed and implemented. The LMFM utilises significantly softer probes, compared to that of a conventional AFM, thanks to the vertical orientation of its mechanical sensor. The new positioning stages created for this SPM, allowed to achieve greater stability and position control (for sample and probe), while ensuring future compatibility with future automated operations, including the sample and tip exchange. The increased stability and positioning control, was achieved through the introduction of the Horizontal Translation Stages, the Vertical Positioning System (VPS) for the probe and a scheme for adjusting the tilt angle of the probe. Especially noteworthy are the elegant and compact VPS which is capable of producing nanometre sized stick-slip steps and the angle adjustment scheme which allows to position the cantilever vertically with  $1/6^\circ$  precision. Additionally, the design was made compatible with other microscopy techniques, such as the conventional SPM imaging, TIRE, sPAINT and SCFI.

The combination of the new stages with the use of vertically oriented micro-cantilever opens up a possibility for LMFM to reproducibly perform sub-femtonewton precision measurements. A force regime commonly reserved to optical tweezers.

The bias bending of silicon nitride cantilevers entering evanescent fields was investigated and it was found to be caused by light coupling inside the cantilever through frustrated total internal reflection. Photostriction effect from the light propagating inside the cantilever was identified as the

most likely mechanism behind the observed bias bending.

The model underlining the bias bending enabled to perform experiments where this effect could be directly accounted for. In particular, a new experimental procedure was implemented to directly measure the transverse Belinfante spin momentum. The experimental results gave an additional insight into the surface nature of the transfer of the helicity-dependent momentum into a mechanical probe.

Finally, the LMFM setup was used in the process of establishing the SCFI method. Time sequence of images of bacteria under evanescent field illumination manifested sub-cellular fluctuations that opened up possibility of a label-free rapid AST. The measurements of fluctuation levels in bacteria mechanically immobilised using a cantilever, showed that the fluctuations observed do not originate from wall cell movement, but rather from sub-cellular motion. This last example clearly demonstrates the versatility of the new LMFM and underscores the importance of investigating nanoscale effects for biomedical sciences.